BREAKUP AND FUSION DYNAMICS OF BERYLLIUM-7

By

Marshall J. Basson

A DISSERTATION

Submitted to
Michigan State University
in partial fulfillment of the requirements
for the degree of

Physics—Doctor of Philosophy

July 2, 2026

ABSTRACT

Light, weakly-bound nuclei, such as ^{6,7}Li, have been observed to have suppressed complete fusion cross sections by up to 30% in comparison to model calculations and those of well-bound nuclei when reacting with heavy targets at energies above the Coulomb barrier. Instead, these isotopes are prone to breakup and cluster transfer, providing alternative reaction channels by which charged fragments escape the target, resulting in enhanced incomplete fusion cross sections. Of particular note is that in neutron-rich, radioactive, and weakly-bound projectiles, additional enhancement of the incomplete fusion cross section has been measured beyond that expected from the degree of weak-binding, suggesting that the current description of physics in models to describe weak-binding in near-barrier reactions is incomplete.

Prior stable beam measurements of weakly-bound nuclei have suggested that in addition to weak-binding, the charged cluster structure of the projectile and the lifetimes of projectile-like resonances through which breakup can occur strongly impact reaction outcomes. However, detailed measurements of breakup dynamics and a well-constrained incomplete fusion cross section are limited to stability.

This thesis concerns the measurement of the breakup and incomplete fusion of ^{7}Be, a proton-rich, weakly-bound and radioactive isotope. A beam of ^{7}Be was bombarded on ^{208}Pb at a beam energy of 51.84 MeV at the National Superconducting Cyclotron Laboratory to measure no-capture breakup and incomplete fusion products. Additionally, this experiment served as the commissioning run for the Fusion Array for Breakup of Light Elements (FABLE), which was created to measure incomplete fusion yields and no-capture breakup yields with large angular separation in coincidence. The characterization of this array and development of its analysis pipeline are discussed.

By comparing the no-capture breakup and incomplete fusion of ^{7}Be to ^{7}Li, its mirror nucleus that has also been measured in prior studies, the role of structure in the resulting reactions can be better understood. Since nuclear structure tends to have strong influence on reaction dynamics at near-barrier energies, the measurement of complete fusion suppression in ^{7}Be may be expected to be similar to that of ^{7}Li, breaking the aforementioned trend of incomplete fusion enhancement

in radioactive isotopes. Additionally, by comparison to ^{6}Li, another well-studied isotope with a similar cluster breakup threshold to ^{7}Be, the importance of clustered binding and structure can be studied.

This work found while the breakup dynamics in ^{7}Be are similar to those of ^{7}Li, the incomplete fusion factor, corresponding to the degree of complete fusion suppression, was $F_{\mathrm{ICF}} = 0.50 \pm 0.04$, in agreement with the trend for enhancement of incomplete fusion in radioactive and weakly-bound nuclei and much larger than those observed for ^{6,7}Li. In addition, comparisons of the incomplete fusion and no-capture breakup yields of ^{6,7}Li served to demonstrate just how different ^{7}Be behaves in these near-barrier reactions. This measurement provides further evidence that the description of breakup and cluster transfer in near-barrier reactions remains insufficient. Finally, an alternative set of scaling parameters is proposed that provides a better trend for existing incomplete fusion factor measurements, based in the properties of charged clusters within a weakly-bound isotope.

ACKNOWLEDGMENTS

In regular circumstances, it takes a village, but I especially have a lot of people to thank. I tell the following joke a lot: "some graduate students get one research group; I got three." I fear it comes off sardonically at times, but I am tremendously grateful to so many people who have helped me along my Ph.D. journey in a variety of ways.

I would first like to thank the original members of the Near-Barrier Reaction Dynamics Group. The lifetime of the group was brief before we all went on separate trajectories, but those first two years were the reason I stuck out another four. I am grateful for the time spent working with Iulia Maria Harca. She helped teach me basics of experimental nuclear science when I was just getting started and her contributions were vital to the success of my thesis experiment.

I am deeply indebted to my advisor, Kaitlin Cook, who also taught me the basics of experimental science, because sometimes I need to hear things twice. She taught me much more than the basics, however. I would not be the scientist I am today without Kaitlin's commitment to my education and development. In spite of the fact that I have spent the majority of my Ph.D. studies in the opposite hemisphere from my advisor, I feel as though I received just as much support from her as any Ph.D. student would under regular circumstances. I do not know how else I can express my immense gratitude towards her for this.

I also wish to express my gratitude to my next advisor, Alexandra Gade. Following the disintegration of NBRD, she helped ensure that my transition was smooth so that I could focus on continuing my studies without barriers. Additionally, she has provided aid and expertise, along with the other Gamma group members, from which I have benefited. Thank you to Dirk Weisshaar, whom I bothered on several occasions with esoteric questions about electronics, and was always happy to entertain them. Thank you to Stephen Gillespie, who not only has provided wisdom and words of encouragement during my graduate studies, but also assisted greatly in the setup for my thesis experiment.

Thank you to the rest of my thesis committee members, Wade Fisher, Paul Gueye, Remco Zegers, and Heiko Hergert, for volunteering their valuable time and energy to provide critical

feedback on my work and support my professional development.

I owe a great deal of thanks to Kyle Brown, who took it upon himself to be my third advisor, for which I am extremely fortunate. Kyle has taught me a lot since we first met in 2018, back when I was an REU student and he was a postdoc in the HiRA group. Since then, Kyle's mentorship and guidance, especially in the later years of my Ph.D. studies, gave me opportunities to grow and helped me build confidence in myself as a scientist.

I also thank the rest of the HiRA group members: Caitlin McCormick, Samuel Justice Brown, Jordan Cory, Gerard Flores, and Tori Zerbach, to whom I have subjected various iterations of the contents of this thesis, in various forms (practice talks, meeting presentations, mad rants) more than anyone aside from my advisor. I have cherished greatly the time I have spent with you all, alongside your suggestions and encouragement.

I am grateful for the incredible support staff at the laboratory, without whom, this work would not be possible. In particular, I would like to especially thank Ron Fox, Giordano Cerizza, and Aaron Chester, who had great patience with me and my many questions about digitization and computing in the early years of graduate studies.

I would like to acknowledge the Nuclear Reaction Dynamics group at the Australian National University for the ^{7}Li + ^{209}Bi measurement that they performed and made available to me, which significantly enhanced the interpretation of the results in this thesis. However, I would like to thank them for more than the data – this work builds on a foundation of fusion and breakup studies to which the Nuclear Reactions Dynamics group has contributed significantly. I have benefited not only from their excellent work, but also the expertise they have lent me and kindness that they have shown me in my various interactions with members of the NRD group over the course of my graduate studies.

I would not be here today without the support of my family – thank you to my mother and father, who always encouraged me to persist, strive to improve, and always supported me. Thank you to my sister, Rebecca, for always being willing to endure a sudden surprise phone call when I needed to vent. Thank you to Drew, Melanie, and Peter, for always cheering me on.

I would like to also acknowledge the contributions of my two feline collaborators, Luna and Nisha. I should clarify that not all of these contributions were welcome – they have added a fair number of typos in this document by way of sitting on my keyboard and turned off my computer no fewer than eight times in an attempt to get my attention while drafting. However, they have also kept me company in the wee hours of the evening when I have been corresponding during Australian business hours or squeezing in one last simulation before bed.

Finally, thanks to my wife, Liz, for a countless number of things. She has quite literally kept me alive in the final stretch of writing this dissertation, when I have done nothing but write and shown incredible tolerance for me exclaiming over Zoom – whether it was all the way back in 2020 and she was trying to focus on her 1L course lectures, or this year, when she would try to sleep while I was hashing out details in this thesis with my advisor at odd hours. More over, I owe her thanks for her love and patience throughout not just graduate school or the thesis writing process, but the whole of the ten years we have spent together. It is my privilege to spend my life with you.

TABLE OF CONTENTS

LIST OF ABBREVIATIONS

BU Breakup

BMIS Batch Mode Ion Source

CF Complete fusion

CFD Constant Fraction Discriminator

DSSD Double-sided Silicon Strip Detector

FABLE Fusion Array for Breakup of Light Elements

FWHM Full Width at Half Maximum

ICF Incomplete fusion

NCBU No-capture breakup

NSCL National Superconducting Cyclotron Laboratory

ReA Reaccelerator

RF Radiofrequency

VADIS Vertical Arc Discharge Ion Source

CHAPTER 1

INTRODUCTION

If a primary objective of nuclear physics is to accurately and precisely describe nucleons interacting via the strong nuclear force, then a direct corollary is that one job of the nuclear physicist is that they must better understand how nuclear matter *reacts* with other nuclear matter through measuring the outcomes of those reactions, and using that information to develop models for understanding the mechanisms that underpin reactions, and from those models, make new predictions.

Stating this goal so plainly may as well be a joke – novel measurements of reactions of interest require a careful and detailed understanding of the reactants, high-resolution detectors for measuring ejectiles to confirm that one studies the specific reaction, and of course, one has to be able to *produce* the reaction by ensuring they have an appropriate target and beam of high enough intensity that they can study processes with millibarn-scale (or much smaller) cross sections. Finally, and most importantly, one needs to be able to understand the interplay between the strong nuclear force and other forces, such as the electromagnetic force, at femtometer and zeptosecond scales. Such a task is no small feat.

Ignoring weak processes, nuclear matter is altered in reactions by splitting it apart or sticking it together. This can involve just a few nucleons (e.g. breakup, stripping, pickup, transfer, knockout) or with many nucleons, such as through fission or fusion reactions. A common theme that unites all of these is the balance between the electromagnetic, or Coulomb, force and the strong nuclear force, which will influence how nuclei react with each other. Depending on the energies of the participant reactants, one force may dominate, but near the Coulomb barrier (at energies roughly $3 - 5$ MeV/u), where the strong nuclear force and Coulomb force balance each other to produce a local maximum in the internuclear potential, both will be critical for predicting reaction outcomes. In this energy regime, the structure of reacting nuclei will also influence the resulting reactions.

An incident particle energy below the Coulomb barrier energy makes fusion very unlikely, and if not for quantum mechanical tunneling, disallowed completely. A vivid example of the interplay between the structure of nuclei and their reactions is the phenomenon of below-barrier

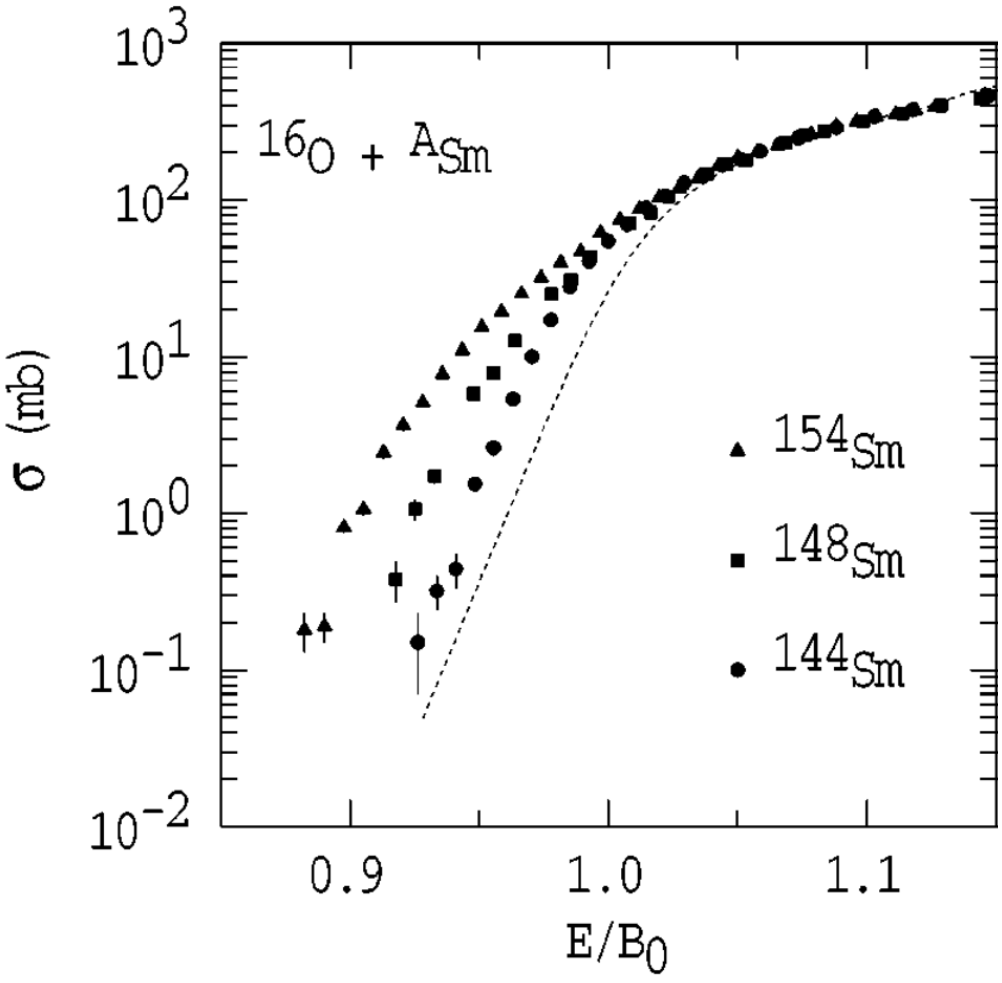

Figure 1.1 Excitation functions for fusion of $^{16}O + ^{144,148,154}Sm$, plotting the measured fusion cross section against a beam energy scaled by the barrier height of each reaction. At energies below the barrier, indicated by the ratio $E/B_0 < 1$, enhancement of the fusion cross section can be observed compared to a single barrier penetration calculation, indicated by the dashed line. Figure from Ref. [1].

fusion enhancement. This has been observed in fusion cross sections, such as in the example of $^{16}O + ^{144-154}Sm$, measured by Dasgupta et al. in Ref. [1], shown in Fig. 1.1. With increasing mass of the samarium isotope, and hence increasing deformation, access to additional low-lying collective rotational and vibrational excitations provide additional couplings for enhancement of the fusion cross section by orders of magnitude.

Weakly-bound nuclei, which have small breakup thresholds into fragments, are useful tools in the study of effects of nuclear structure in reaction dynamics. Their weak-binding means that they

can exhibit strong cluster structures in their low-lying states [2]. For instance, ^{7}Be and ^{7}Li both have low-lying $\alpha + x$ structures – in the case of ^{7}Be, it resembles a loosely-bound α and ^{3}He, and in the case of ^{7}Li, it similarly resembles an α and a triton bound together [3, 4].

A resulting phenomenon of particular note for this work is the above-barrier *complete fusion suppression* measured in weakly-bound nuclei. We define **complete fusion** (CF) as the total capture of the charge of a projectile. This operational definition focuses on charge transfer rather than mass transfer to avoid the difficulties associated with accounting of neutron evaporation when measuring fusion cross sections. In contrast, **incomplete fusion** is partial charge capture, separate from charged particle evaporation, resulting in the charge of the initial projectile being split between the target and an escaping fragment. **Total fusion** is the sum of all fusion processes. In other words, the total fusion cross section σ_{TF} can be expressed as

$$\sigma_{\mathrm{TF}} = \sigma_{\mathrm{ICF}} + \sigma_{\mathrm{CF}}, \tag{1.1}$$

where σ_{CF} and σ_{ICF} are the cross sections for complete and incomplete fusion, respectively. **Complete fusion suppression** is the phenomenon of significantly reduced CF cross-sections compared to calculations (such as single-barrier penetration models and coupled-channels calculations) and to reactions of tightly bound nuclei forming the same compound system. An example of this can be shown in Fig. 1.2, where the scaled excitation functions for complete fusion cross sections with ^{18}O (well-bound) on ^{198}Ot and ^{7}Li (weakly-bound) on ^{208}Bi are plotted, comparing measured and calculated cross sections in reactions forming the same compound nucleus[5]. The complete fusion cross section for ^{7}Li is suppressed when compared to ^{18}O when forming the same compound nucleus by up to 30% at energies above the fusion barrier. This suppression of the complete fusion cross section at above-barrier energies has been measured in a variety of weakly-bound nuclei and is accompanied by commensurately large incomplete fusion cross sections. Instead of only complete fusion, scattering, and transfer processes, one must consider the effects of incomplete fusion and breakup reactions to fully describe the dynamics.

The complete fusion suppression for a reaction can be quantified in the incomplete fusion factor,

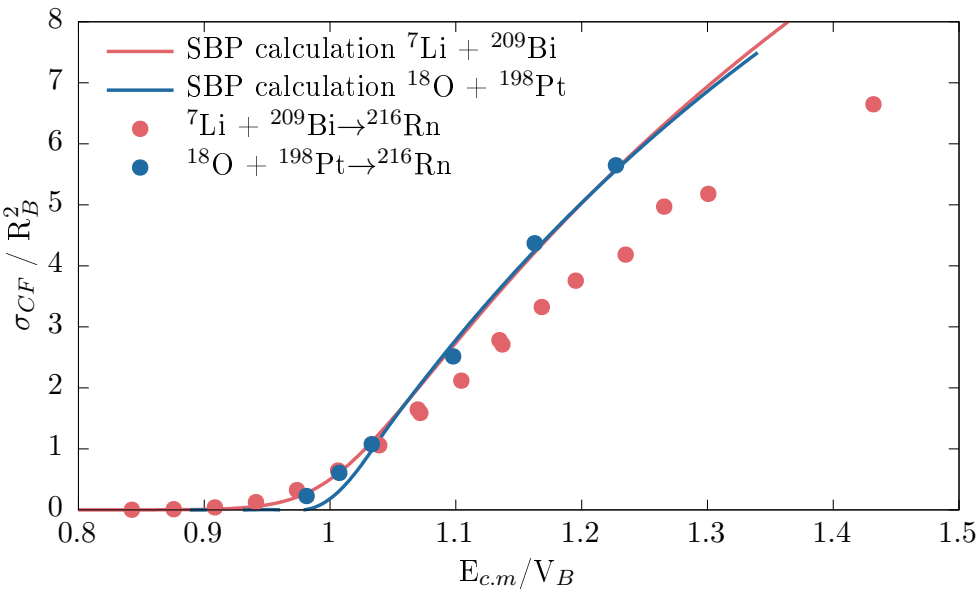

Figure 1.2 Excitation functions for complete fusion of ^{7}Li+^{209}Bi and ^{18}O+^{198}Pt, with energy and cross sections scaled by the barrier properties for each reaction, are plotted together [5]. Single barrier penetration calculations are also plotted for each reaction. The calculated cross sections for fusion of ^{7}Li overshoot the measured complete fusion cross sections significantly.

F_{ICF}, defined as the ratio between incomplete fusion and total fusion cross sections:

$$F_{\mathrm{ICF}} = \frac{\sigma_{\mathrm{ICF}}}{\sigma_{\mathrm{TF}}} = \frac{\sigma_{\mathrm{ICF}}}{\sigma_{\mathrm{CF}} + \sigma_{\mathrm{ICF}}}. \tag{1.2}$$

Figure 1.3 shows the measured incomplete fusion factors for a variety of weakly-bound nuclei studied in prior work[5–9], plotted against their breakup threshold into multiple charged fragments [10].[1] The breakup threshold into charged fragments may be of relevance in understanding the fusion dynamics of nuclei that are so prone to breaking into pieces. In fact, two different trends emerge when comparing the degree of complete fusion suppression versus the breakup threshold into two charged fragments for different isotopes – one for stable and one for unstable nuclei. Specifically, an enhancement of incomplete fusion yields has been measured in radioactive and weakly-bound nuclei.

The studied radioactive and weakly-bound nuclei have different low-lying structures (including $\alpha + x$ clusters versus halos) but share their enhancement of incomplete fusion. They also are all

[1]The distinction of breakup threshold into two or greater charged fragments will be made throughout this work. This is because of the operational definition of complete fusion focusing on charged yields – neutron breakup alone will not affect the complete fusion cross section as a result.

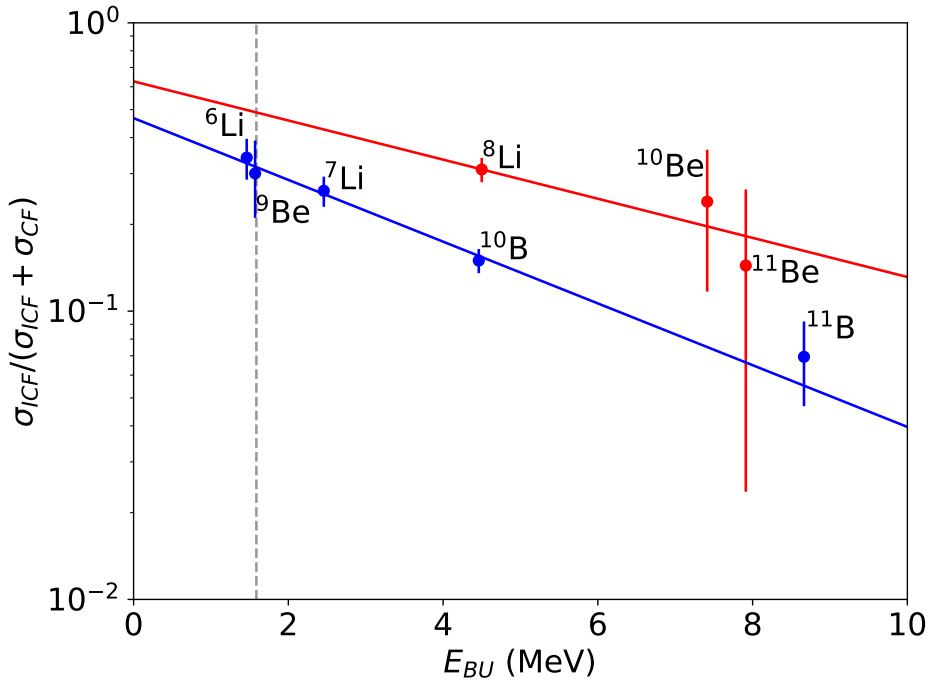

Figure 1.3 Degree of complete fusion suppression (the ratio of incomplete fusion and total fusion cross sections) plotted against the breakup threshold into two charged fragments for several different isotopes studied in prior experiments, each point and uncertainties having been digitized when not reported directly from Refs. [5–9]. The blue markers indicate measurements of stable isotopes and red markers indicate measurements of radioactive isotopes. The blue and red lines correspond to exponential fits of each group. This work intends to add the complete fusion suppression of ^{7}Be to the list of studied isotopes to better understand the relationship between breakup threshold versus low-lying structure for understanding the mechanism for complete fusion suppression. The breakup threshold for ^{7}Be is indicated by the dashed, vertical line.

neutron rich. By studying the incomplete fusion of ^{7}Be, a proton-rich, radioactive and weakly bound isotope, the separation between the radioactive and stable nuclei may be further supported or broken. I will also note here that it would be surprising for the breakup and fusion of ^{7}Be to differ significantly from ^{7}Li in view of their similar low-lying structure. However, a comparison of the two may instead reveal the importance of breakup threshold in better understanding the reaction dynamics in this case.

Prior studies have also demonstrated various complexities one must consider to fully describe reactions with weakly-bound nuclei near the barrier. Firstly, in a re-analysis of Rafei et al. [12], investigation of the multitude of breakup channels leading to ^{8}Be breakup reactions and compar-

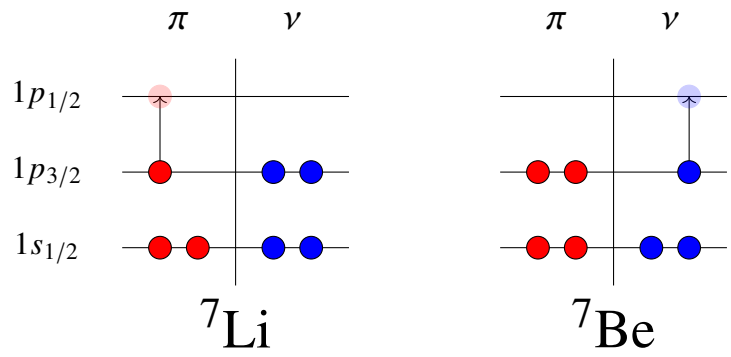

Figure 1.4 Shell model diagrams for ^{7}Li and ^{7}Be, respectively, in their ground state configurations. The first excited state for each isotope is generated by exciting the unpaired nucleon in each nucleus' $1p_{3/2}$ shell to the $1p_{1/2}$ shell, as indicated by the arrow for each isotope.

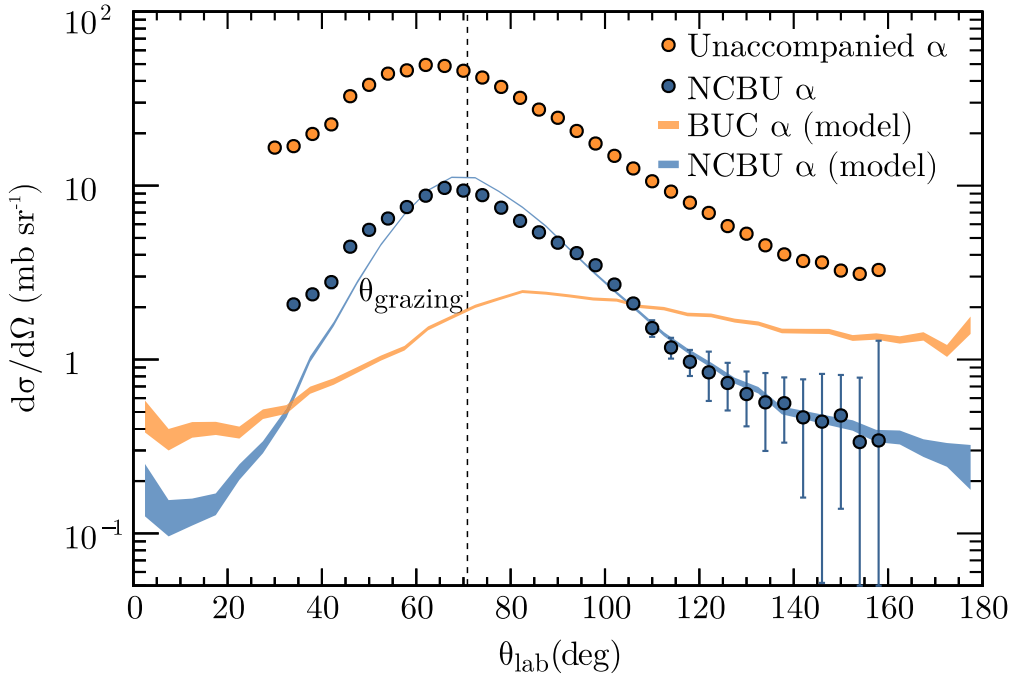

Figure 1.5 No-capture breakup (blue) and unaccompanied α (orange) differential cross sections resulting from impingement of ^{7}Li on ^{209}Bi at E_{CM} = 38.7 MeV, comparing the differential cross sections resulting from the α-yield associated with breakup and incomplete fusion measured by Cook et al. and a semi-classical breakup capture. model (shaded regions). While breakup can be accurately modeled by breakup, sequential breakup and capture is insufficient for modeling the enhanced incomplete fusion yields. The dashed vertical line indicates the grazing angle. Figure adapted from Ref. [11].

ison to simulations demonstrated that the timescales of projectile-like resonances are critical for understanding contributions of breakup near or far away from the target, but that even with this additional sophistication of a model, that only 1/3 of breakup could account for the resulting incomplete fusion yields in sub-barrier impingement of ^{9}Be on various heavy targets [13]. Secondly, the angular distribution of unaccompanied α-particles,[2] resulting from reactions of ^{7}Li on ^{209}Bi, measured by Cook et al., provided further evidence that breakup models under-predict the measured incomplete fusion products, indicating that breakup and capture alone is an incorrect model for explaining the enhancement of incomplete fusion products [11]. A comparison between simulated and measured differential cross sections for breakup and incomplete fusion α-yield is shown in Fig. 1.5. In the experimental differential cross section for unaccompanied α, one sees a peak at forward angles (smaller than the grazing angle) compared to the corresponding breakup-capture calculations, which peak at more intermediate angles (larger than the grazing angle). This difference in the spectrum indicates an alternative process must be the source of the enhanced incomplete fusion yields, rather than sequential breakup and capture. In this case, direct transfer of the tritium nucleus in the measurement of the ^{7}Li reactions was proposed to lead to the majority of the resulting α-yield, and hence, incomplete fusion. Effects of resonance timescales in breakup will be further discussed in Ch.6 and implications of the unaccompanied yields will be further discussed in Chs. 7 and 8.

Measurements near the fusion barrier provide a sensitive test for how the configuration of nuclear matter can influence the resulting reactions. The measurement of fusion reactions should also be a goal for informing other sub-fields of nuclear physics. By providing measurement inputs for nuclear calculations and theoretical models, informing astrophysical reaction rates through cross section measurements, and providing better insights into fusion and transfer processes for moving up the nuclear chart in the continued push for superheavy element studies, near-barrier fusion measurements serve an important role in advancing different goals in nuclear physics.

There are four main goals of this thesis in the study of breakup and fusion reactions of ^{7}Be on

[2]The measurement of so-called "unaccompanied" charged particles can be thought of as the yield of projectile-like particles associated with incomplete fusion. Further details are provided in Ch. 2.

^{208}Pb at above-barrier energies.

1. **Interplay between structure, breakup, and fusion:** By measuring fusion and breakup reactions of ^{7}Be on ^{208}Pb, this work will study the possibility of direct cluster transfer as a mechanism of complete fusion suppression. Measuring this direct cluster transfer mechanism in another isotope will elucidate the impact of cluster transfer reactions on fusion cross sections. Specifically, by measuring the breakup and fusion of ^{7}Be, the mirror nucleus of ^{7}Li, we can exploit the similar underlying structures to better understand how breakup thresholds (which differ by over 1 MeV) influence complete fusion suppression. Figure 1.6 shows the level schemes for both nuclei and Fig. 1.4 shows the shell model occupation diagrams for each isotope. Notably, they share a prominent $7/2^{-}$ resonance at similar excitation energies, which are unbound to decay into an α-particle and a secondary charged fragment.

2. **Role of Breakup Threshold in Predicting CF Suppression:** In addition to ^{7}Li, there are preexisting studies of the breakup and fusion of ^{6}Li [5]. In particular, the measurement of ^{6}Li + ^{209}Bi yields the same compound nucleus in the case of complete fusion as that of ^{7}Be + ^{208}Pb for this study. Therefore, the differences between breakup threshold and secondary residues for ^{7}Be, ^{7}Li, and ^{6}Li are noted in Table 1.1. These differences in breakup threshold and secondary fragment should inform the interpretation of differences in breakup and fusion cross sections for the different projectiles.

3. **Procedure in a Radioactive Ion Beam Environment:** This experiment is one of the early instances of making such a detailed near-barrier breakup measurement with a radioactive ion beam from which the incomplete fusion yields were directly measured, rather than fusion evaporation residues. While a similar procedure has been used in the past for measurement of the incomplete fusion yields in a stable beam environment [11], This attempt should serve as a foothold for future measurements, as well as a first-attempt from which we may learn from some issues for future trials. Furthermore, earlier measurements of incomplete fusion

cross sections indicate an enhancement of the incomplete fusion yield when using radioactive ion beams, as shown in Fig. 1.3. However, ^{7}Be may not be expected to behave similarly to the previously measured isotopes – ^{7}Be is *not* a halo nucleus, but prior measurements of other beryllium isotopes have focused on halo nuclei. Examining whether the breakup and fusion of ^{7}Be matches more closely with that of ^{7}Li or these other radioactive ion beam measurements may demonstrate how the reaction dynamics change when moving away from stability or confirm the importance of low-lying structure first and foremost. This experiment was also entailed the commissioning of the Fusion Array for Breakup of Light Elements (FABLE). Such an array was required to be able to measure the fragments from breakup with large angular separation in coincidence and to maximize solid angle coverage. The process of characterizing the detectors in the array and methods for analysis of its data will be discussed through the entirety of this thesis.

Isotope	Breakup fragment 1	Breakup fragment 2	Breakup Threshold (MeV)
^{7}Be	α	^{3}He	1.587
^{7}Li	α	t	2.467
^{6}Li	α	d	1.474

Table 1.1 Breakup thresholds into charged fragments for ^{7}Be and ^{6,7}Li.

The structure of this thesis is as follows:

1. Background theory and concepts for understanding the analysis of the experiment upon this work focuses are summarized in Ch. 2.

2. Specifics regarding the experimental apparatus, including the beam production, chamber and FABLE, are detailed in Ch. 3.

3. The analysis procedure of FABLE, including the process of turning a signal in a silicon detector into the position and energy of the inducing particle, is described in Ch. 4. Also included in this chapter are some basic features of the singles data from this experiment, including particle identification and the angular distribution.

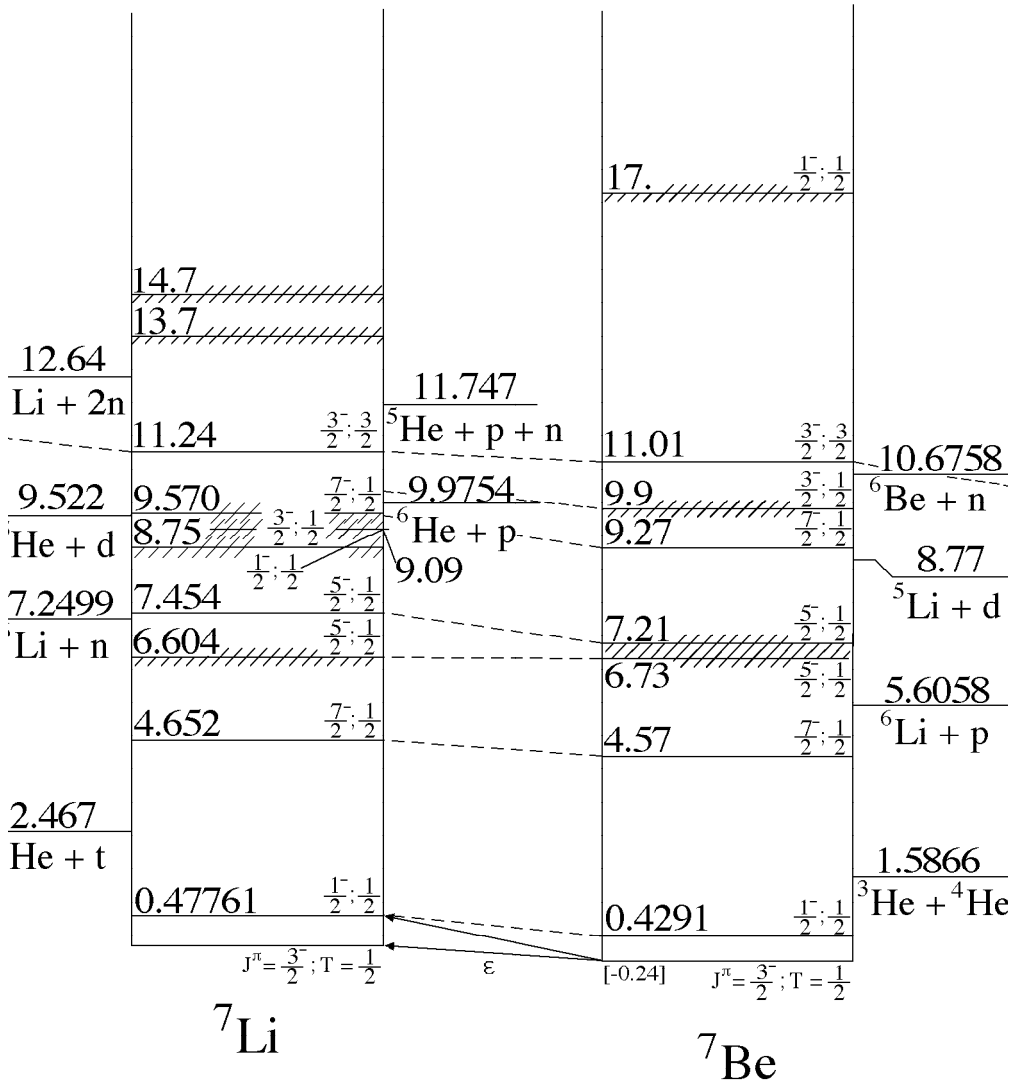

Figure 1.6 Energy level schemes for ^{7}Li and ^{7}Be by the TUNL Nuclear Data Evaluation Project, in Ref. [14].

4. One challenge of the analysis of this experiment was associated with the profile of the delivered beam. A procedure for quantifying the offset of the center-of-mass of the beam spot is described in Ch. 5.

5. The coincidence analysis of no-capture breakup fragments and corresponding simulations from *KOOKABURRA* is discussed in Ch. 6. Also present in this chapter are the details of efficiency determinations and breakup simulation validity.

6. Chapter 7 contains the main result of this work – the measured differential cross sections for the unaccompanied helium isotopes are presented in this chapter, alongside the corresponding degree of incomplete fusion for ^{7}Be + ^{208}Pb.

7. Lastly, Ch. 8 considers the implications of the complete fusion suppression measurement of ^{7}Be in this work and in the context of prior measurements, including comparisons to ^{6,7}Li data from prior experiments in Refs. [5] and [11].

CHAPTER 2

BACKGROUND

In the last chapter, the phenomenon of complete fusion suppression was introduced, along with context and motivation for measuring the breakup and fusion of ^{7}Be in particular at energies above the fusion barrier. In this chapter, theoretical concepts will be reviewed for the purposes of understanding and analyzing the measurements made for this thesis.

2.1 Reaction Channels

There are several reaction channels a projectile can enter when reacting with heavy targets at near-barrier energies. For the following discussion, see Fig. 2.1 for illustrations of the various reaction channels. The most peripheral process possible is scattering: either elastic scattering, where kinetic energy is conserved, or inelastic scattering, where some of the projectile energy is lost to excitations in the internal structure of the reacting nuclei. There can also be the transfer or one or more nucleons between the projectile and the target. More central collisions can result in **complete fusion** (CF), or total charge capture of the projectile by the target.

In reactions with weakly-bound nuclei, which are inherently prone to projectile breakup into charged fragments, the breakup fragments can still enter the complete fusion channel, where both fragments are captured. There is also **no-capture breakup** (NCBU), an analogue of scattering, where following breakup, both charged fragments interact with the target's Coulomb field and escape. Finally, there is **incomplete fusion**, where there is only partial charge capture from the projectile. Note also that incomplete fusion can occur by way of direct cluster transfer, in contrast to projectile breakup followed in sequence by capture. Both methods of incomplete fusion necessitate an escaping charged particle, which will be referred to in this work as an *unaccompanied particle*. The properties of the unaccompanied particles can be leveraged to determine an incomplete fusion cross section and interpret the reaction dynamics[11]. Consider the cross section associated with all reactions that generate an α-particle, σ_α:

$$\sigma_\alpha = \sigma_{\mathrm{ICF}} + \sigma_{\mathrm{NCBU}} + \sigma_{\mathrm{evap}} + \sigma_{\mathrm{decay}}, \tag{2.1}$$

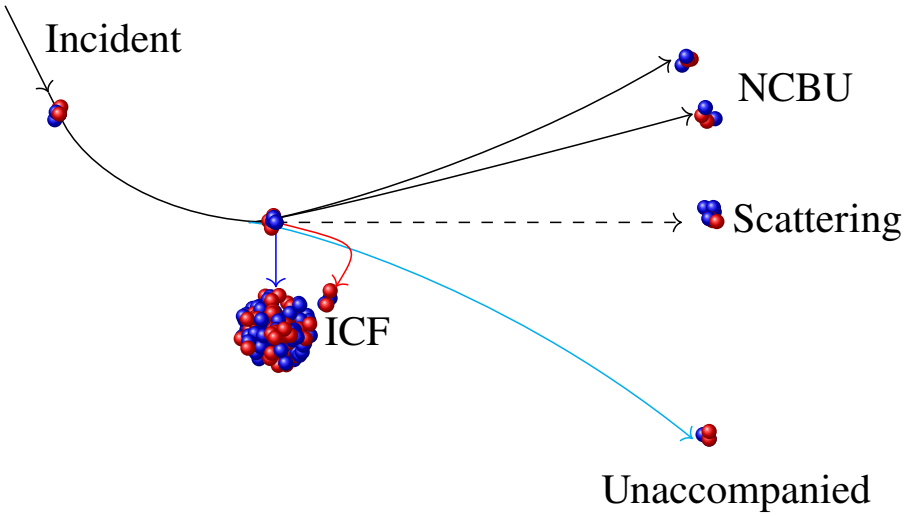

Figure 2.1 Cartoon of reaction channels with weakly-bound nuclei. The projectile can scatter, following the dashed, black trajectory. Alternatively, the weakly-bound projectile can disintegrate into fragments. After breakup occurs, both charged fragments can escape the target, as shown by the solid black trajectories, denoted as no-capture breakup (NCBU). Alternatively, one or more fragments can follow a trajectory similar to the one indicated in red, and fuse to the target. The case of partial charge capture is called incomplete fusion (ICF) and the case of total charge capture is referred to as complete fusion (CF). The projectile can also completely fuse to the target without breaking up, as indicated by the blue trajectory, and is indistinguishable from breakup followed by sequential capture of the fragments. Finally, note that in the case of ICF, the trajectory of the escaping unaccompanied breakup fragment is indicated in cyan. Measuring these unaccompanied particles is one signature of incomplete fusion. Note that the drawn trajectories in this cartoon do not correspond to realistic trajectories for each process.

where σ_{ICF} is the cross section for incomplete fusion generating an escaping alpha, σ_{NCBU} gives the cross section for α-yield from no-capture breakup, σ_{evap} is associated with α-particles arising from evaporation from a compound nucleus following fusion, and σ_{decay} is the cross section associated with α-decay of various reaction products formed in fusion. Decay products resulting from fusion can be removed based on their low, mono-energetic peaks compared to the energies expected from breakup fragments. Contributions due to fusion evaporation must be considered with sufficiently high excitation energy, and will be discussed in Ch. 7. We can measure σ_{α} and σ_{NCBU} directly and constrain σ_{evap}, thus, incomplete fusion cross section measured by the unaccompanied α particles can be expressed as

$$\sigma_{\mathrm{ICF}} = \sigma_{\alpha} - \sigma_{\mathrm{NCBU}} - \sigma_{\mathrm{evap}}, \tag{2.2}$$

or the difference between the cross section associated with the total α-yield and that arising from

Breakup Mode	σ (mb)
$^{7}\mathrm{Li} \rightarrow \alpha + t$	9.6 ± 0.6
$^{7}\mathrm{Li} - 2n \rightarrow {}^{5}\mathrm{Li} \rightarrow \alpha + p$	8.6 ± 0.5
$^{7}\mathrm{Li} - n \rightarrow {}^{6}\mathrm{Li} \rightarrow \alpha + d$	10.8 ± 0.5
$^{7}\mathrm{Li} + p \rightarrow {}^{8}\mathrm{Be} \rightarrow \alpha + \alpha$	7.3 ± 0.4

Table 2.1 No-capture breakup cross sections for $^{7}\mathrm{Li} + {}^{209}\mathrm{Bi}$ at $E_{\mathrm{CM}} = 38.7$ MeV [17] [11].

no-capture breakup and fusion evaporation.

One nuance not mentioned in the earlier discussion is that following transfer reactions, there can be another opportunity for secondary processes. *Transfer-triggered* breakup modes arise when a transfer reaction between the beam nucleus p and target T populates some unbound, resonant state in the resulting projectile-like nucleus and can also contribute to complete fusion suppression through no-capture breakup or breakup followed by capture:

$$p + T \rightarrow q^{*} + R \rightarrow a + b + R, \tag{2.3}$$

where q^{*} is the projectile-like resonance that forms following the initial transfer reaction, R is the recoiling target-like nucleus following transfer, and a and b are breakup fragments following the decay of $q^{*} \rightarrow a + b$. See Fig. 2.2 for an illustration of this process. In some cases, such as that of ^{7}Li, the transfer-triggered breakup modes through the resonance structures of the intermediate, unbound nuclei can contribute to breakup cross-sections at a similar scale to that of their direct counterparts and should not be ignored [13, 15–17]. Table 2.1 displays the no-capture breakup cross sections for $^{7}\mathrm{Li} + {}^{209}\mathrm{Bi}$ at $E_{\mathrm{CM}} = 38.7$ MeV. These data show that contributions from transfer-triggered breakup are of a similar scale to that of the direct breakup channel in this case.

Timescales for breakup are important for determining which resonant states may contribute to complete fusion suppression. If a projectile-like resonance is populated via transfer or direct excitation, its lifetime must be brief enough such that the nucleus breaks up during its trajectory near the target nucleus incomplete fusion can occur. One such example is in population of resonances in ^{8}Be, which will be discussed in Ch.6. The ^{8}Be 2^{+} resonance, with a lifetime of order 10^{-22} s, is short-lived and thus its breakup α particles will be emitted near the target. Along small ℓ trajectories, this leads to complete fusion by sequential capture of each fragment or incomplete

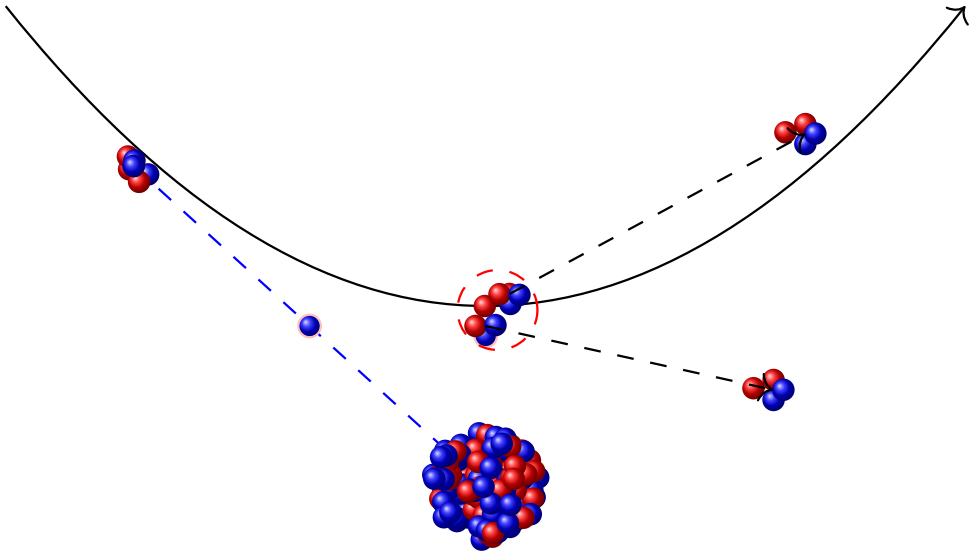

Figure 2.2 Cartoon illustrating transfer-triggered breakup, following the projectile along its trajectory. There is some initial nucleon transfer, depicted by the circled pink nucleon, exchanged between the incoming projectile and the target. This populates some weakly-bound resonant state within the projectile (indicated by the nucleus circled in red), which can then decay, or break up, into two or more charged fragments, which follow different trajectories than the initial one of the projectile. Whether or not this breakup occurs near or far from the target depends on the lifetime of the populated resonance.

fusion by capture of only one fragment. Along large ℓ trajectories, the ^{8}Be disintegration leads to no-capture breakup, typically. However, for long-lived resonances, like the 0^{+} resonance of ^{8}Be, with a lifetime of order 10^{-16} s, projectile disintegration far later than the zeptosecond-timescale. Therefore, particles along small ℓ trajectories that would typically lead to capture result in complete fusion more often, but not incomplete fusion. Meanwhile, particles along large ℓ trajectories end in no-capture breakup and the escape of the resulting fragments [13, 18].

2.2 Nuclear Scattering and Potentials

For interactions between charged fragments loosely bound together as a ^{7}Be nucleus or interactions between a lighter projectile and heavier target, one can describe the quantum mechanical states that these nuclei occupy based on a particle in a spherically symmetric potential well, which is a more general model. The radial Schrödinger equation for a particle with mass m is:

$$\frac{d^2u(r)}{dr^2} + \frac{2m}{\hbar^2}\left[E - V(r) - \frac{\hbar\ell(\ell+1)}{2mr^2}\right]u(r) = 0, \tag{2.4}$$

where ℓ is the angular momentum, $\hbar$ is Planck's reduced constant, and using the typical substitution $u(r) = rR(r)$.

The actual interaction can be defined as the sum of Coulomb, nuclear, and centrifugal potentials:

$$V(r) = V_C(r) + V_N(r) + V_\ell(r), \tag{2.5}$$

where the Coulomb potential is known to be a repulsive $1/r$ force proportionate to the charge product of the interacting nuclei. For interactions between a point-like charge and a charged sphere, the potential can be defined as

$$V_C(r) = \begin{cases} \frac{Z_1 Z_2 e^2}{r}, & r > r_c, \\ \frac{Z_1 Z_2 e^2}{2} \frac{3r_c^2 - r}{r_c^3} & r \leq r_c, \end{cases} \tag{2.6}$$

where r_c is the radius of the charged sphere and $e^2 = 1.44$ MeV fm.

Finally, the centrifugal term of the potential can be expressed as

$$V_\ell(r) = \frac{\ell(\ell+1)\hbar^2}{2\mu r^2}, \tag{2.7}$$

where ℓ is the angular momentum quantum number and $\mu = m_1 m_2/(m_1 + m_2)$ is the reduced mass between the interacting nuclei.

The nuclear potential should describe a short-range, attractive force and there are various options for different nuclear potentials. A common phenomenological choice for the parametrization of the nuclear potential is the Woods-Saxon potential:

$$V_N(r) = -\frac{V_0}{1 + \exp\left(\frac{r - R_0}{a_0}\right)}, \tag{2.8}$$

where V_0 is the depth of the potential well, r is the radial separation, $R_0 = r_0(A_1^{1/3} + A_2^{1/3})$ is the well radius based off the mass numbers of the reacting nuclei, and a_0 is the surface diffuseness parameter.

A more complex choice for the parametrization of the potential is based on the *optical model*, which defines real and imaginary components of a potential, $V(r) = U(r) + iW(r)$, to model scattering and absorption of an incoming beam on the target, respectively [19].

In this thesis, the São Paulo Potential version 2 (SPP2) was employed for determining the real part of the nuclear interactions between breakup fragments and recoiling targets for simulations. The SPP2 calculates a double-folding nuclear potential by integrating an effective nucleon-nucleon interaction over the proton and neutron density distributions within the nucleus. For a full description, see Ref. [20]. Potentials calculated with SPP2 were fit to functions of the form of the Woods-Saxon potential in Eq. 2.8 to describe particle interactions for breakup simulations, which will be described in Sec. 2.6 and Ch. 6.

2.3 Cross sections

Before continuing, cross sections have been mentioned throughout this text and should be formally defined. The **cross section** is the quantity we use to denote the probability of a nuclear reaction, with its size (given in area) corresponding to an area transverse to the direction of motion of the colliding nuclei. The cross section, σ for a process is

$$\sigma = \frac{Y}{IN}, \tag{2.9}$$

where Y is the is the yield rate of the reaction product in particles-per-second, I is the incident beam intensity in particles-per-second, and N is the target number density, given in atoms-per-unit area. The differential cross section is used to express the reaction rate in a region subtended with solid angle $\Delta\Omega = \sin\theta d\theta d\varphi$, as this will correspond to the likelihood of measuring a reaction within a detector's view in (θ, φ). This differential cross section is expressed as

$$\frac{d\sigma}{d\Omega} = \left.\frac{Y(\theta,\varphi)}{IN\Delta\Omega(\theta,\varphi)}\right|_{(\theta,\varphi)}. \tag{2.10}$$

Elastic scattering can be approximated as Rutherford scattering in cases where the nuclear contribution to the potential is negligible compared to that of the Coulomb force. Such situations include reactions at sufficiently sub-barrier energies and scattering at very forward angles. We can exploit this approximation for cross section normalization later in this thesis (see Ch. 6). The distance of closest approach, $R_{\min}$, for Rutherford scattering between nuclei with atomic numbers Z_1 and Z_2 is

$$R_{\text{min}} = \frac{Z_1 Z_2 e^2}{2E_{\text{CM}}} \left(1 + \frac{1}{\sin(\theta/2)}\right), \tag{2.11}$$

where here, θ is the center-of-mass frame scattering angle, Z_1 is the proton number of the projectile, Z_2 is the proton number of the target, and E_{CM} is the energy of the projectile in the center-of-mass frame. Note also that this quantity can be experimentally determined by measurement of the scattering angle along with knowledge of the reaction system in the case of Rutherford scattering. The scattering angle can be related to the impact parameter, b, which gives an effective radius for the relevant interaction. The impact parameter can be expressed as

$$b = \frac{Z_1 Z_2 e^2}{2E_{\text{CM}}} \cos\frac{\theta}{2}. \tag{2.12}$$

The impact parameter, b, relates the distance of closest approach of the projectile's trajectory *without* accounting for interaction with the potential field. Therefore, by relating the scattering angle to the impact parameter, one describes the relationship between the incoming and outgoing trajectories of the projectile thanks to the impact of the reactions with the target field. More central collisions, with smaller impact parameters, and thus leading to larger θ, result from more direct processes, while more peripheral reactions have greater influence on the outgoing projectile trajectories compared to the incoming, arising larger impact parameters. This also implies that by inspecting the angular distribution of different ejectiles, one can infer what kinds of collisions are associated with the resulting cross sections. This will be important when considering a comparison of the unaccompanied α and ^{3}He spectra from reactions in this work in Ch.7.

Now, note that the impact parameter is related to the differential scattering by

$$\frac{d\sigma}{d\Omega} = \left|\frac{b}{\sin\theta}\frac{db}{d\theta}\right|, \tag{2.13}$$

one can find that the differential Rutherford scattering cross section is

$$\frac{d\sigma_{\text{Ruth}}}{d\Omega} = \left(\frac{Z_1 Z_2 e^2}{4E_{\text{CM}}}\right)^2 \times \frac{1}{\sin^4(\theta_{\text{CM}}/2)}. \tag{2.14}$$

For a detailed derivation of scattering in a Central force field, of which Rutherford scattering is one case, see Goldstein's description in Ch. 3 in Ref. [21].

Finally, the classical cross section for total fusion, not accounting for weak-binding and in the classical limit ($E \gg V_B$), can be written as

$$\sigma_{\mathrm{TF}}(E) = \pi R_0^2 \left(1 - \frac{V_B}{E}\right), \tag{2.15}$$

where R_0 is the well radius and V_B is the barrier depth. The above-barrier total fusion cross section was estimated using the program *CCFULL* [22] and fusion evaporation cross sections were calculated using PACE4 in Ch. 7 [23, 24].

2.4 Q-values

The ground state-to-ground state *Q-value* of the reaction, denoted as Q_{gg}, is defined as the difference in the combined mass energies of reactants and products. This can be expressed as

$$Q_{gg} = \sum_i m_i c^2 - \sum_f m_f c^2, \tag{2.16}$$

where i sums over the nuclear masses of the initial reactant nuclei and f sums over the product masses. A reaction with a positive Q-value is energetically favorable, while a reaction with a negative Q-value has a threshold set requiring that amount of input energy. However, if the reaction populates an excited state in the exit channel, the energy required to excite the body should be accounted for to determine the Q-value for the particular reaction, which I will denote as simply Q. Then the Q for a reaction that populates an excited channel with energy E_x is

$$Q = Q_{gg} - E_x. \tag{2.17}$$

While there should be a distribution of Q-values thanks to the various excitations one can populate in the exit channels, the *optimum Q-value*, Q_{opt}, is the average expected Q-value for a transfer-based process, since a range of energies are viable, up to Q_{gg}. We can predict this Q_{opt} by matching the incoming projectile trajectory to the outgoing projectile-like particle trajectory, such that the excitation energies of the transferred nucleons match the height of the potential barrier between the reactants [25]. Ignoring the recoiling nucleus excitations, the optimum Q-value can be approximated as

$$Q_{\mathrm{opt}} = E_{\mathrm{CM}} \left(\frac{Z_p' Z_t'}{Z_p Z_t} - 1\right), \tag{2.18}$$

where E_{CM} is the center mass frame energy of the incident projectile, E'_{CM} is the energy of the outgoing projectile, Z'_p, Z'_t are the charges of the outgoing projectile-like and recoiling nuclei, and Z_p, Z_t are the charges of the incoming reactant nuclei. I will note that if the trajectories of the incoming and outgoing projectiles are matched, then $E_{\mathrm{CM}} = E'_{\mathrm{CM}}$ implicitly. The experimentally determined Q-value can thus give insight into the excitation of the recoiling target.

In the case of no-capture breakup, where two breakup fragments can be measured exclusively, the experimental Q-value is reconstructed as an observable of measured reactions in the experiment discussed in this work. When the energies of both breakup fragments are measured, the Q-value can be expressed as

$$E_{\mathrm{beam}} + Q = E_r + E_1 + E_2, \tag{2.19}$$

where E_{beam} is the beam energy after correcting for energy loss in the target[1], $E_{1,2}$ are the breakup fragment energies, and E_r is the recoiling nucleus' energy, which is calculated from the known two-body kinematics of the reaction by knowing the individual breakup fragment energies, angles, and identities. Therefore, the reconstructed Q-value, Q, is calculated in this work by

$$Q = E_1 + E_2 + E_r - E_{\mathrm{beam}}, \tag{2.20}$$

where I emphasize that the projectile-like excitations are already accounted for in the breakup fragment kinetic energies, E_1 and E_2. This means that the reconstructed Q-value reflects excitations in only the target-like nucleus.

2.5 Breakup Trajectories and Relative Energy

I will now provide a mathematical description of the relationship between breakup fragment locations and energies and their initial projectile. Let a weakly-bound projectile, p, (perhaps created by a preliminary transfer reaction) break up into charged fragments 1 and 2, at some point along its trajectory. The opening angle between 1 and 2 can be denoted as θ_{12}. We could imagine the trajectory of p had it *not* broken up. This trajectory can be defined as the pseudo-projectile

[1] In this work, it is assumed that all reactions occur halfway through the target. This means that energies of the incoming particle will be lowered according to this expected deposition, as well as outgoing particles will have their energies adjusted upward to account for further energy loss exiting the target. For more details on energy loss adjustments, see Sec. 2.7.

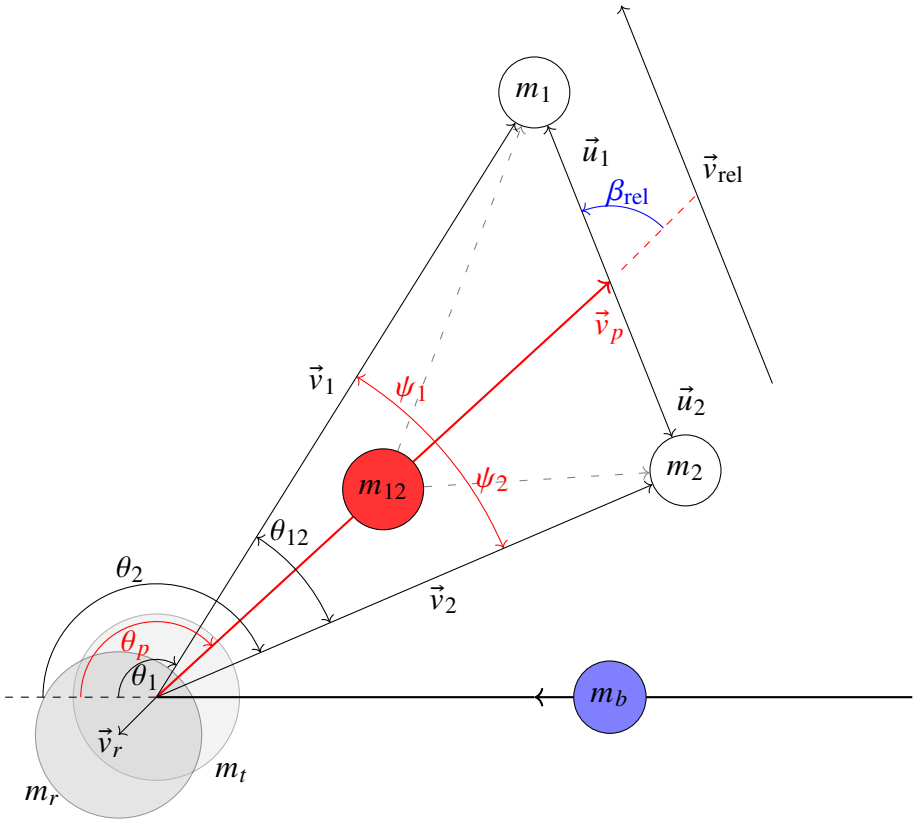

Figure 2.3 Depiction of the breakup of a pseudoprojectile m_{12} into two charged fragments, m_1 and m_2, each scattering at angles θ_1 and θ_2, with opening angle between the fragments $\theta_{12} = \psi_1 + \psi_2$, following the reaction of incoming beam particle m_b and target m_t, resulting a recoiling target with velocity $\vec{v}_r$ and the breakup fragments with velocities $\vec{v}_1$ and $\vec{v}_2$. The pseudoprojectile's scattering angle with respect to the target is θ_p. The breakup fragments have a relative velocity between each other, $\vec{v}_{\rm rel}$, and the angle between this separation vector and the pseudoprojectile velocity vector, $\vec{v}_p$ is denoted as $\beta_{\rm rel}$.

scattering angle, which I will denote as θ_p. By considering the opening angle between the real breakup fragments versus the trajectory of the virtual projectile, we can determine efficiencies for breakup, discussed in Ch. 6. This scheme is shown in Fig. 2.3.

The relative energy between the breakup fragments gives insight into the weakly-bound projectile's state prior to breakup by way of the invariant mass method. By measuring both breakup fragments' energies and positions, one can infer the identity of the recoiling nucleus and the remaining energy associated with excitation of the projectile. In this way, the relative energy can be reconstructed. The relative energy is defined as

$$E_{\rm rel} = \frac{1}{2}\mu v_{\rm rel}^2, \tag{2.21}$$

where $\mu = m_1 m_2/(m_1 + m_2)$ is the reduced mass and the relative velocity is

$$v_{\text{rel}} = \sqrt{v_1^2 + v_2^2 - 2|v_1||v_2|\cos\theta_{12}}, \tag{2.22}$$

which is the relative speed between the breakup fragments following disintegration, given as a function of the particle speeds and the opening angle, θ_{12}, between the breakup fragments. The opening angle can be calculated according to the individual breakup fragment positions by

$$\cos\theta_{12} = \cos\theta_1 \cos\theta_2 + \sin\theta_1 \sin\theta_2 \cos(\varphi_1 - \varphi_2), \tag{2.23}$$

where the scattering angles of each breakup fragment are given θ_1 and θ_2, and the azimuthal angles are given by φ_1 and φ_2.

Additionally, note that at the energy range of $3 - 5$ MeV/u, the non-relativistic limit is valid for relating particle velocities to their energies by $E = \frac{1}{2}mv^2$. By knowing the initial beam energy and final energies of the breakup fragments, along with their positions, this framework allows one to establish the energetics of the intermediary reactants.

Finally, the relative momentum between the fragments can be captured in the angle, β_{rel}, defined as

$$\sin\beta_{\text{rel}} = \frac{v_1 v_2 \sin\theta_{12}}{v_1^2 u_1^2 + v_2^2 u_2^2 - 2u_1 u_2 v_1 v_2 \cos\theta_{12}}, \tag{2.24}$$

where θ_{12} is the opening angle between fragments, $v_{1,2}$ are particle speeds in the laboratory frame and $u_{1,2}$ are the particle speeds in the center-of-mass frame. This quantity is useful in understanding the orientations of breakup fragments, as will be discussed in Ch. 6.

2.6 Simulating Breakup: *KOOKABURRA*

It is worthwhile to describe a model for breakup that can be used as a framework for interpreting the dynamics in reactions of weakly-bound nuclei. This model will later be used in simulations (to be discussed later in this chapter, as well as Ch. 6). The experimental analysis relies on breakup simulations to calculate detector efficiencies and confirm interpretations of experimental spectra. The simulation program, *KOOKABURRA*, written by E.C. Simpson, has been employed in this work for these purposes [26]. *KOOKABURRA* is a semi-classical, time-dependent, three-body

breakup simulation code that calculates the trajectories of both direct and transfer-triggered breakup fragments. The program requires the following inputs:

1. Potential interactions between the participating nuclei. In this work, Woods-Saxons potentials fitted to the São Paulo Potential 2 were used for the nucleus-nucleus interactions [20].

2. Q-values for transfer and breakup reactions.

3. Excitation-energy dependent lifetimes for each resonance in each projectile, provided by R-matrix calculations with relative strengths from the experimental relative energy spectra for each resonance.

4. Excitation energies of the target-like nuclei based on the reconstructed Q-value spectra.

5. The *breakup function*, described below.

Once these model inputs are provided, *KOOKABURRA* can simulate stochastic breakup for each mode. It does this by first simulating the incoming Rutherford trajectory of the projectile. It then simulates a transfer reaction between the projectile and target, assuming that a transfer-triggered breakup mode is being triggered. After this, for each timestep, there is a *chance* that the projectile will disintegrate. The program samples from a probability distribution of excitation energy-dependent mean lifetimes to stochastically simulate breakup,[2] at which point the projectile instantaneously breaks into pieces. The breakup fragment trajectories are then simulated, taking into account interactions with the target's field, as well as interactions between the breakup fragments, which are important for simulating observables from breakup realistically [18]. Within this framework, the locations and energies of the breakup fragments can be simulated for each breakup mode

[2]The lifetimes for decay are excitation energy-dependent because while breakup is simulated instantaneously in *KOOKABURRA*, the product fragment trajectories can remain localized for some time following disintegration. The spatial separation of the breakup fragments is then dependent on the excitation energy of the projectile prior to breakup. By sampling from a distribution of lifetimes based on the measured excitation energy distribution to stochastically determine the timestep for breakup, this is reflected in the model.

The breakup function is the relation between the probability for pseudoprojectile breakup to the distance of closest approach between the projectile and the target, modeled as the exponential

$$P(R_{\text{min}}) = e^{\mu R_{\text{min}} + \nu}, \tag{2.25}$$

where R_{min} is the distance of closest approach along a Rutherford trajectory as defined in Eq. 2.11, and μ and ν are fitted parameters for a particular reaction (in practice, reached iteratively by fitting based on the no-capture breakup cross sections, as discussed in Ch. 6). The larger distance of closest approach implies a more peripheral interaction, which means that the projectile is less likely to break up, and instead having a more Rutherford-like trajectory. Conversely, closer distances of closest approach will result in the strong nuclear force having greater influence, yielding more breakup and fusion processes. The resulting simulations were employed to identify and interpret contributions from the various resonances populated in the projectile prior to breakup within the experimental data and to determine the coincidence efficiency of the detector array.

2.7 Energy Loss

Energy deposition underpins the operating principle of radiation detection and $\Delta E - E$ particle identification. Additionally, accounting for energy lost through non-active materials is integral for accurately measuring energies of particles. The energy of a particle straggling through some material can be calculated via the Bethe-Bloch equation for stopping power,

$$-\frac{dE}{dx} = \frac{4\pi n Z_p^2}{m_e v^2} \left(\frac{e^2}{4\pi\epsilon_0}\right)^2 \ln\left[\frac{2m_e v^2}{I}\right], \tag{2.26}$$

where $-dE/dx$ is the stopping power, e is the fundamental charge, m_e is the electron mass, ϵ_0 is the vacuum permittivity constant, n is the electron density, Z_p is the atomic number of the projectile, v is the speed of the projectile, and $I = 10\ \text{eV} \cdot Z_t$ is is the mean excitation energy of the material through which the projectile passes, with atomic number Z_t [27]. This model for energy loss, implemented via Zeigler [28], will be used throughout this analysis. In particular, energy loss is taken into account for energy calibrations and dead layer determinations, as well as corrections in kinematic reconstruction of reaction participants after the particles are detected. In the coincidence analysis, the fragment energies can be used to reconstruct the Q-value of the reaction, along with

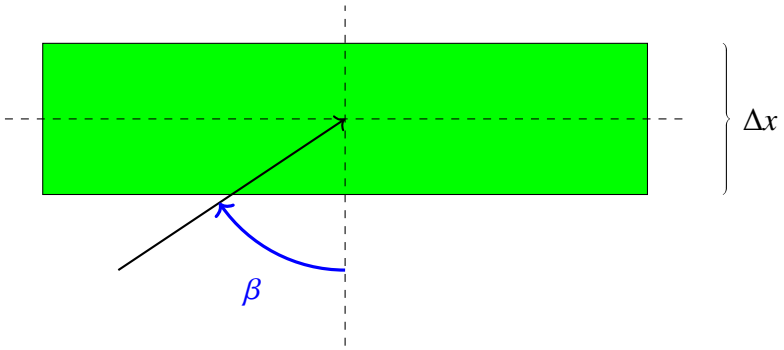

Figure 2.4 Diagram of a particle entering a material (shaded in green) with some thickness Δx at some angle of incidence β. The larger this angle is, the more energy is deposited as the particle passes through the material since its effective thickness becomes $\Delta x_{\text{eff}} = \Delta x / \cos\beta$.

properties of the pseudoprojectile in the case of coincidence measurement. Finally, note that while the energy loss is proportional to a factor of approximately $Z_p^2 / \ln Z_t$, the kinetic energy of a particle is related to its mass, which goes according to its total nucleon number. This means that the energy deposition in a material will be different for different isobars of the same element. This principle underpins particle identification with $\Delta E - E$ detectors – that is, measuring the energy deposited in a thin, front ΔE detector and the remaining projectile energy in a thick, back E_{res} detector. The different energy depositions creates a particle identification matrix with separate bands of energy for each isotope measured.

One note for energy corrections is that the effective thickness of a material depends on the angle of incidence of the incoming particle. When a particle enters a material at some angle, β, as shown in Fig. 2.4, the thickness of the material, Δx, should be multiplied by a factor of $1/\cos\beta$ to account for the increased interactions through the particle's trajectory. All routines throughout this work that correct for energy loss via depositions (in the target, detector dead-layers, and so on) will account for this corrective factor.

CHAPTER 3

EXPERIMENTAL DETAILS

3.1 Introduction

In the last chapter, the motivation for a study of the breakup and fusion of ^{7}Be was discussed, as well as some theoretical background enabling understanding the reactions of interest in this study and how we may measure them. In this chapter, the setup of the experiment to measure breakup and fusion cross sections will be discussed, including the detectors, electronics, and beam production.

3.2 Beam Production and Targets

The ^{7}Be beam was produced on the ReA6 ReAccelerator beamline at the National Superconducting Cyclotron Laboratory (NSCL), in a standalone mode, decoupled from the cyclotrons. Following proton irradiation of a ^{7}Li target, producing ^{7}Be by a (p,n) reaction, a pure sample of ^{7}Be was produced by chemical separation, the procedure of which is described in Ref. [29]. The pure ^{7}Be sample was then inserted into the Batch-Mode Ion Source (BMIS), consisting of a sample oven and a VD5 Versatile Arc Discharge Ion Source (VADIS). After heating the sample in the oven, nitrogen trifluoride was injected to reduce surface adsorption of the ^{7}Be, forming beryllium-fluoride. These compounds were then ionized with VADIS and accelerated through a mass separator to select only ^{7}Be [30]. From there, the beam was then injected into the electron ion beam trap to bunch the continuous stream of ions into a bunched and pulsed beam, as well as charge bred to a 4+ charge state for acceleration and to ensure purity by avoiding contamination of ^{7}Li. The beam was then selected in a Q/A separator, bunched with a radiofrequency quadrupole to 80.5 MHz, and accelerated in a system of quarter wave resonators until it was delivered to the experimental area in the ReA6 vault, resulting in a beam with an average intensity of 5000 particles per second [31, 32]. The beam had a 4^{+} charge state at 51.84 MeV before impinging on the ^{208}Pb self-supporting target. This energy, which was about 30% above the fusion barrier energy, was chosen to match the beam-to-barrier energy ratio from prior measurements of ^{6,7}Li on ^{209}Bi from Refs. [5] and [11]. The target was measured to have a thickness of 560 μg/cm^{2} using

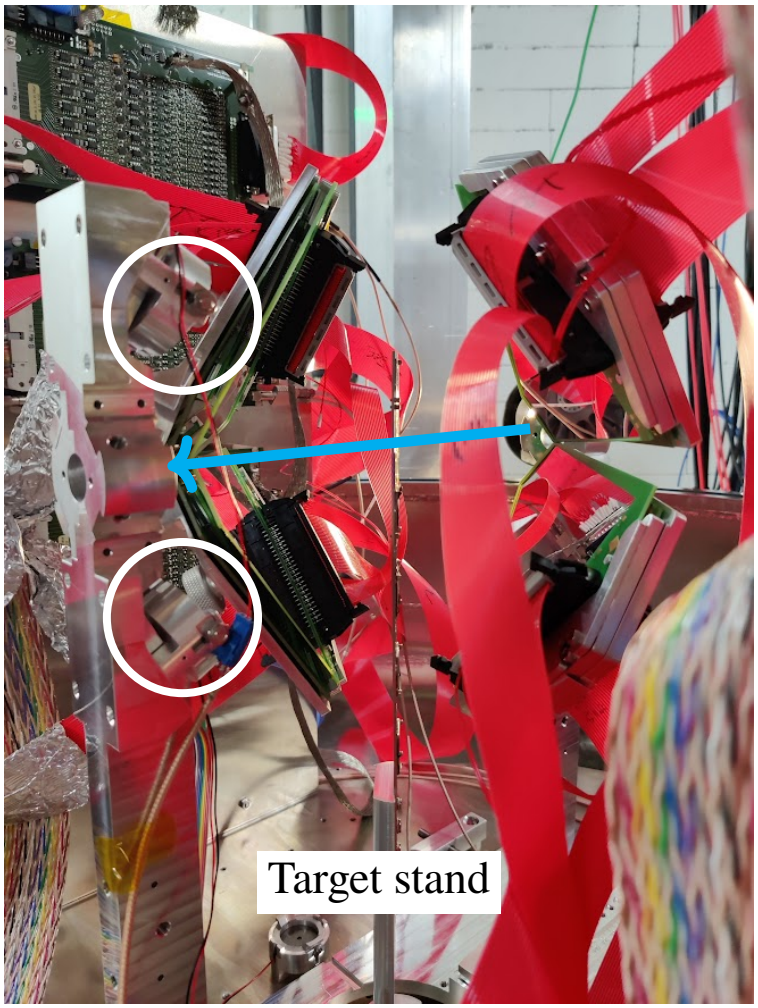

Figure 3.1 FABLE arranged in the front-back configuration for recording breakup fragments in coincidence with large angular separation at both forwards and backwards angles. The beam axis and direction is indicated with the cyan arrow. The target is placed at a 45° angle with respect to the beam. Silicon beam monitors were mounted at forward angles, indicated by the white circles, to measure elastic scattering for normalization. In this configuration, the breakup and incomplete fusion yields from ^{7}Be on ^{208}Pb were measured.

α-transmission with a ^{232}U source [1]. This measurement was made with FABLE in its "front-back" configuration, pictured in Fig. 3.1, where the detectors were positioned to maximize coverage at both forward and backward angles to measure breakup fragments with large angular separation.

In addition, a ^{14}N was also produced at 56 MeV with a 5^{+} charge state. FABLE recorded these data in a "lampshade" configuration placed at backwards angles, as depicted in Fig. 3.2. This measurement was used in the energy calibration of FABLE's ΔE detectors, since the ^{14}N would

[1] The ^{232}U source spectrum will be discussed in Sec. 4.2, as it was the same source used to eventually calibrate the detectors.

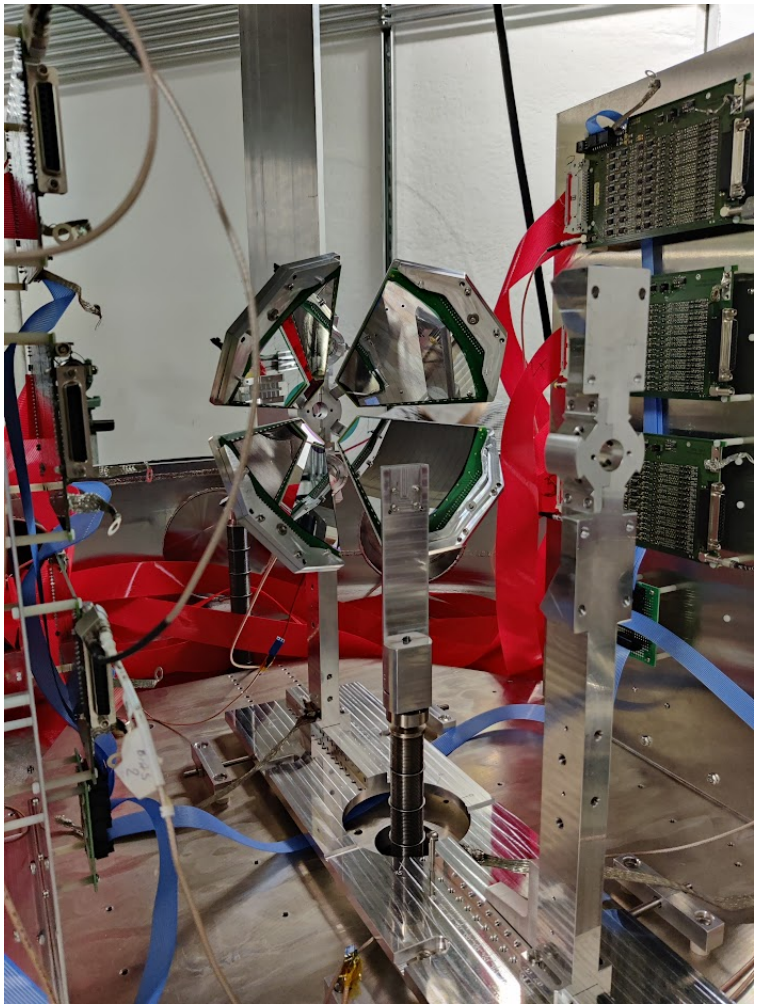

Figure 3.2 FABLE arranged in the lampshade configuration for recording elastic scattering of ^{14}N, which was used in the energy calibration of the detectors

deposit its full energy and stop in the ΔE detectors.

The measurement of Rutherford scattering in ^{14}N was also used to determine the solid angle of the silicon surface barrier detectors, or beam monitors, positioned at forward angles as pictured in both Fig. 3.1 and Fig. 3.2. The measurement of Rutherford scattering in these detectors is used to normalize breakup cross sections (see the discussion in Sec. 6.4.2).

3.3 Apparatus: CFFD and FABLE

The beam was received in the Charged Fission Fragment Detector (CFFD) chamber. Housed in the chamber was FABLE, the Fusion Array for Breakup of Light Elements. It is an array of eight wedge-shaped, double-sided silicon detectors (DSSD), model MMM manufactured by Micron

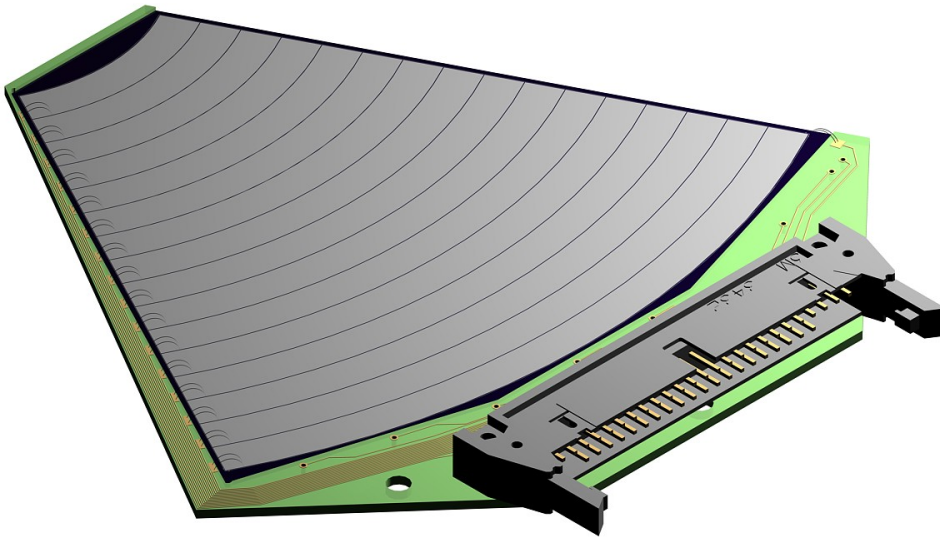

Figure 3.3 Graphic of the MMM detector design from Micron Semiconductors Ltd [33]. Eight of these double sided silicon detectors were arranged to form the four $\Delta E - E$ telescopes in FABLE.

Telescope	ΔE Thickness (μm)	Nominal E_{res} Thickness (μm)
W	111	500
X	109	500
Y	112	500
Z	112	500

Table 3.1 Detector thicknesses for each MMM within each telescope in FABLE.

semiconductors, the design of which is pictured in Fig.3.3. These neutron transumtation doped (NTD) detectors were arranged with a near detector of roughly 100 μm thickness, and behind it, a thick detector of roughly 500 μm thickness, to form four telescopes for $\Delta E - E$ particle identification. The exact detector thicknesses are listed in Table 3.1. Each DSSD has a thin aluminum coating on both the front and back of the detector.

Each DSSD has a 60° wedge design consisting of sixteen 6.4 mm wide latitudinal arcs (junction side) and 8 longitudinal sectors (ohmic side) subtending 6.8° in the plane of the detector, with the active area having an inner radius of 65.20 mm and an outer radius of 270.20 mm [33]. The overlap between signals from an arc and a sector form virtual "pixels" which give the location of a charged

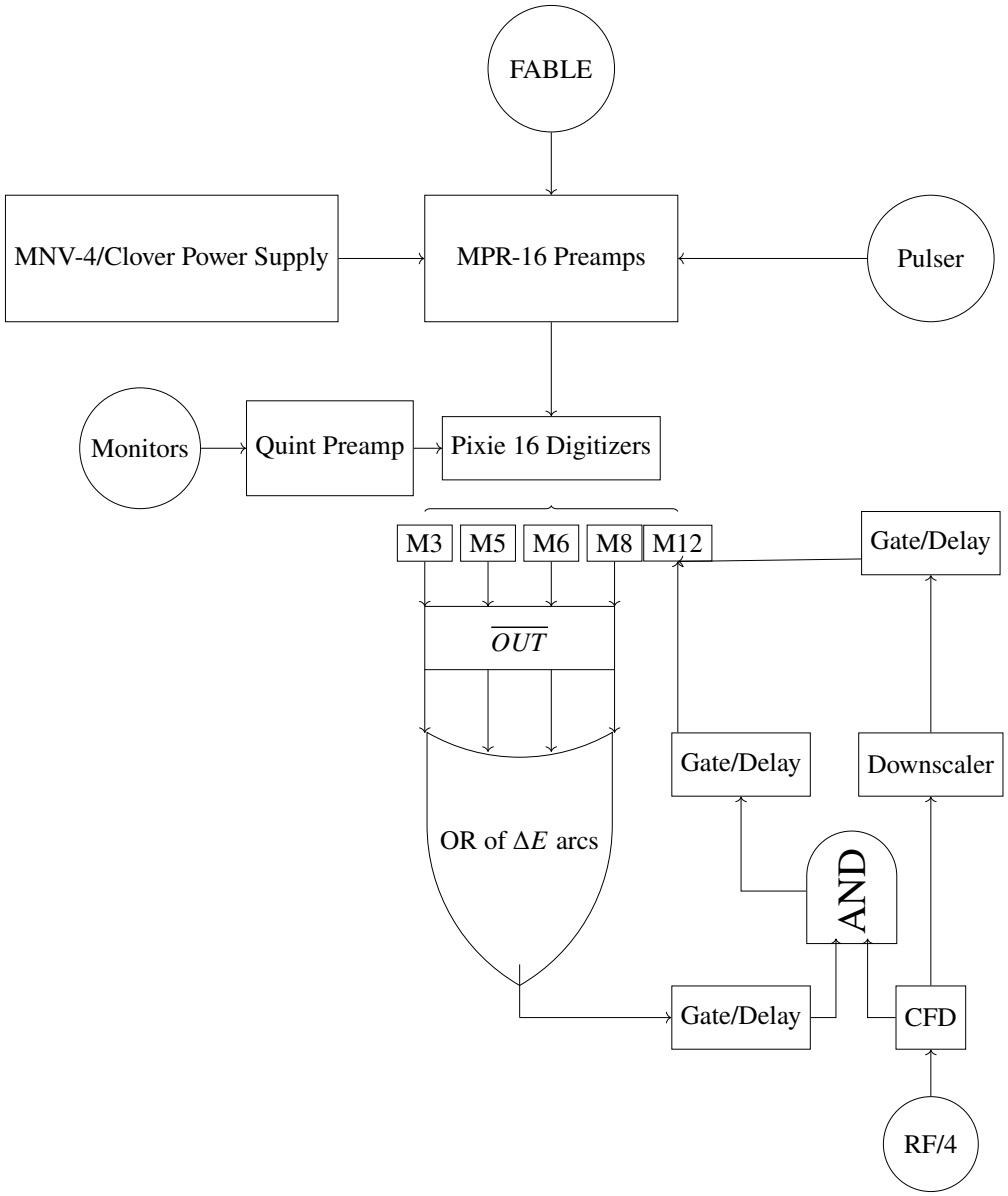

Figure 3.4 Block diagram of the signal chain used for recording data from FABLE and monitor detectors for this experiment. It is discussed in the text.

particle within the detector. Each arc spans $\Delta\theta = 4^\circ$ in polar angle and each sector spans $\Delta\varphi = 8^\circ$ in azimuthal angle when arranged around a target. More details about the pixelization procedure can be found in Ch. 4. Each detector was reverse-biased to improve charge collection and reduce noise [27].

During the experiment for this work, the readout from the detectors were amplified by the MPR-16 preamps and then the waveforms were digitized by the XIA Pixie-16 digitizers (100

MHz and 250 MHz sampling rate modules). The waveforms were processed by a fast trapezoidal filter algorithm[2] and a digital constant fraction discriminator (CFD) algorithm to extract timing and a slow trapezoidal filter for energy. The block diagram for the electronics setup used in this experiment is shown in Fig. 3.4. FABLE signals were amplified by MPR-16 preamplifiers, which were powered by a Clover power supply. A pulser signal was also input directly into the preamps, along with beam monitor signals, which were amplified by the quint preamp. The resulting signals were then recorded in Pixie-16 digitizers, indicated by M3-12 in the graphic. The OR of a livetime trigger of several digitizer modules were grouped to generate a gate corresponding to the OR of ΔE detector arc signals. Meanwhile, the beam radiofrequency (RF) signal (downscaled by a factor of 4) was input into an analogue CFD module. The AND of the ΔE arcs and downscaled RF was used to create a trigger for recording a digitized version of a further downscaled beam RF pulse in the module 12 digitizer in order to extract timing from the beam for a time-of-flight when compared to timing from FABLE. However, time-of-flight was not able to be used in the analysis of this experiment due to difficulty with the digitization of the full-scale beam RF and ambiguity in the time-of-flight spectra when using the downscaled beam RF.

3.4 Conclusion

In this chapter, the details of the experimental setup were reviewed. This included the production of the ^{7}Be beam, the introduction of FABLE, and the electronics chain used in the experiment. In the next chapter, the process of using the signals recorded in FABLE to extract position and energy information of particles will be discussed.

[2]For a review of trapezoidal filters in digital pulse processing, cf. Chapter 17 of Reference [27].

CHAPTER 4

ANALYSIS PROCEDURE

In Ch. 3, we measured particles punching through the FABLE array by digitally recording the charge signals of the individual arcs and sectors on each MMM Si detector with Pixie-16 digitizers. By processing the charge waveforms through trapezoidal filters, energies were then digitally written for each channel. However, there is still much work to be done to properly correlate individual signals after they are recorded. This chapter concerns the process of how a virtual pixel must be formed on the detectors where a particle entered, and then how a sorting routine is employed to properly pair ΔE and E pixels for a single particle that punches through a telescope in the array.

4.1 Coordinate Determination

I will now describe the coordinate scheme for localizing particles in experiments with FABLE, following the procedure described in Ref. [34]. When we measure a particle in one of the DSSDs, we can assert that it has landed within the *plane* of the detector, and assign coordinates on that plane

$$\begin{aligned} x &= R\sin(\gamma), \\ y &= R\cos(\gamma), \\ z &= 0, \end{aligned} \tag{4.1}$$

where R refers to the radial distance from the circle circumscribing the DSSD, and γ refers to the angle between the radial segment and the central axis splitting the DSSD in half. This scheme is shown in Fig. 4.1. This describes the location of a charged particle on the surface of the detector. Note that because a particle is measured in arc and sector strips, from which a position is determined based off a virtual pixel, the particle is localized within the pixel, but its position is not exactly known. Therefore, in the analysis routine, the location of the particle is randomized within the assigned pixel, and its appropriate R and γ values calculated.

After assigning a particle its position within the detector, through a series of coordinate transformations, the DSSD can be shifted to its true position in the lab frame, with the target at its origin.

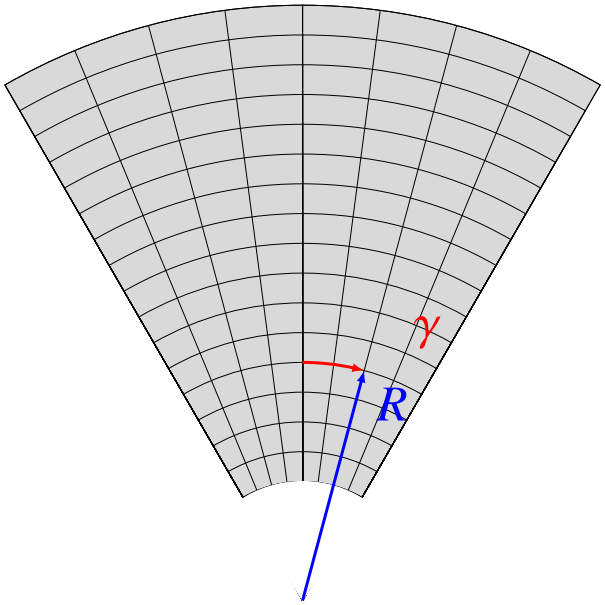

Figure 4.1 Coordinate system for hits in FABLE within the DSSD plane. Charged particles can be specified according to the radial offset, R, from the DSSD center, defined as the origin, alongside the polar angle from the central axis, defined as γ.

By doing this, the relative position of the particle within the detector can be transformed into its position relative to the target in a typical laboratory frame. This series of transformations that I will now describe is shown in Fig. 4.2. The coordinate system is defined such that the beam moves positively along the z-axis and impinges on a target at the origin. I will dive into the handling an "off-center" beam in Ch. 5. However, for the sake of defining a coordinate system, I simply note here that an additional translation with respect to the beam offset is the only transformation necessary to go between this coordinate system and one where the beam spot is off-axis.

First, the detectors are twisted about the y-axis in the $x - z$ plane by $\eta = 0$. The relevant transformations are

$$\begin{aligned} x &\longrightarrow z\cos\eta - x\sin\eta, \\ z &\longrightarrow z\sin\eta + x\cos\eta. \end{aligned} \tag{4.2}$$

For $\eta = 0$, as in this experiment, the detector plane has been moved from the $x - y$ plane into the $y - z$ plane.

The detectors then lean in the $y - z$ plane toward the target at an angle of $\zeta = 45°$, which can

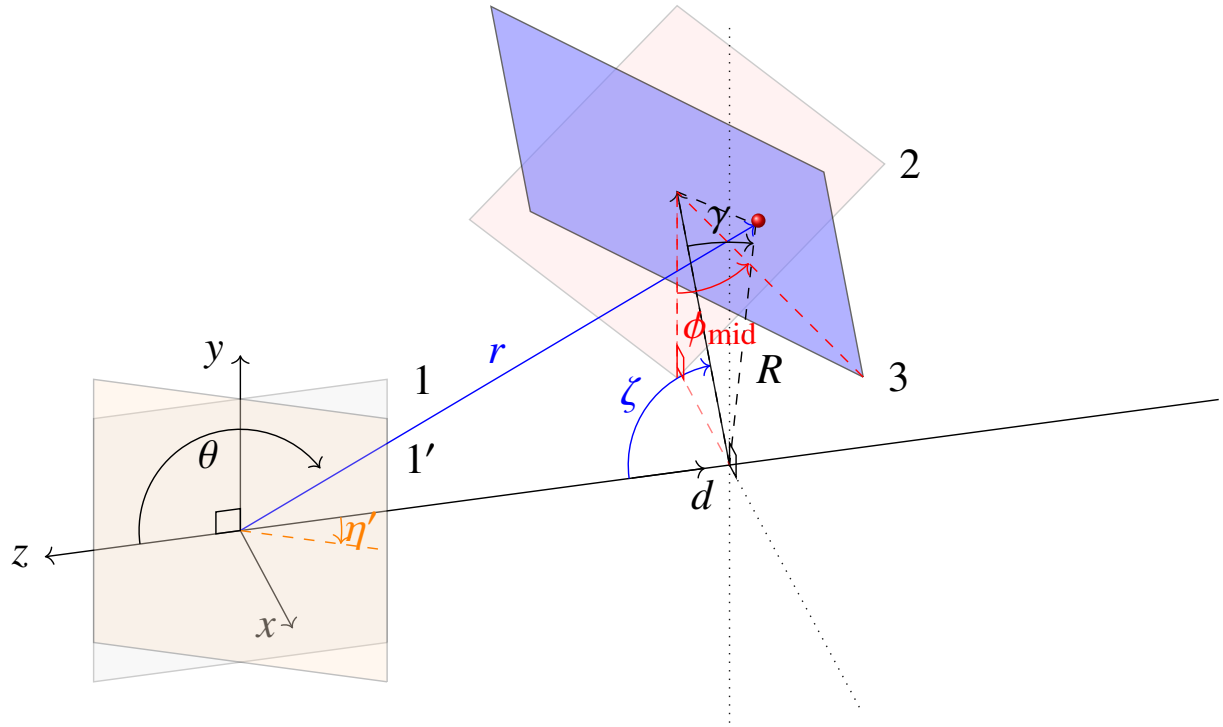

Figure 4.2 Illustration of the coordinate transformations for FABLE position determination. The DSSD starts at the origin in the $x-y$ plane. It then undergoes a twist of $\eta = 0$ in the $x-z$ plane, as shown by grey plane 1, but for demonstrative purposes, a twist of non-zero η' is also shown in the orange plane $1'$, although the following transformations will be revolving around the former case. After twisting, the detector plane is leaned by ζ in the $y-z$ plane, shown by the red plane 2. This lean, along with translational offsets for visual clarity, are applied from $1 \rightarrow 2$. The last rotation is by angle ϕ_{mid} in the $x-y$ plane. Again, along with the translational offset, this is shown by the blue plane 3.

be accounted for in the rotation transformation

$$\begin{aligned} z &\rightarrow z\cos\zeta - y\sin\zeta, \\ y &\rightarrow z\sin\zeta + y\cos\zeta. \end{aligned} \tag{4.3}$$

After leaning, the detectors are rotated within the x-y plane according to the azimuthal angle with respect to the middle of the detector, ϕ_{mid}:

$$\begin{aligned} x &\rightarrow x\cos\phi_{\text{mid}} - y\sin\phi_{\text{mid}}, \\ y &\rightarrow x\sin\phi_{\text{mid}} + y\cos\phi_{\text{mid}}. \end{aligned} \tag{4.4}$$

Last, the detector is translated according to cartesian offsets between the DSSD and its stand,

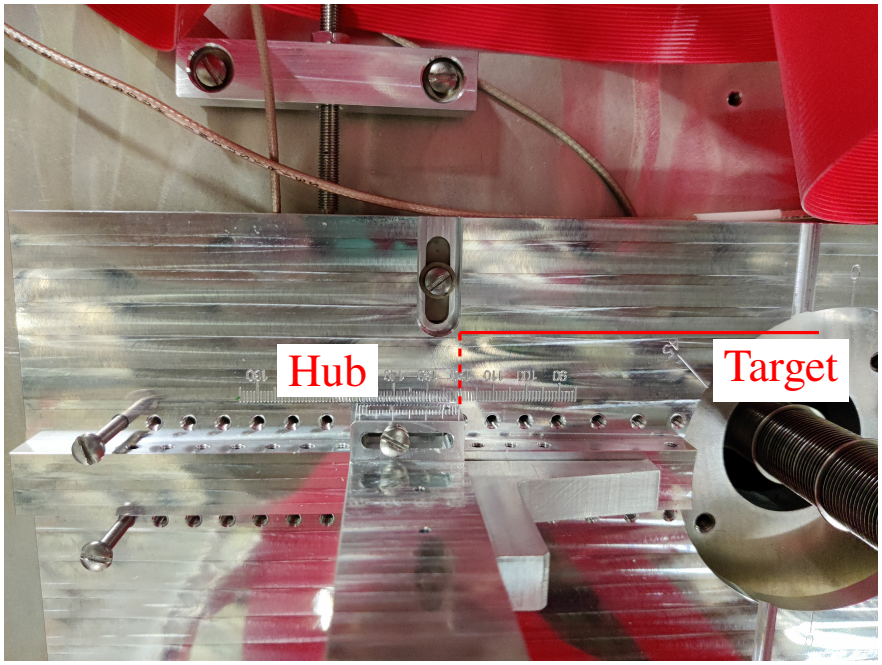

Figure 4.3 Top-down picture a FABLE hub placed to mount detectors at forward angles and the target stand. The distance between thew two is indicated with a red line and is the $z_{\text{hub-target}}$ used in the position determination procedure.

as well as the stand and the target.

$$\begin{aligned} x &\longrightarrow x + x_{\text{offset}}, \\ y &\longrightarrow y + y_{\text{offset}}, \\ z &\longrightarrow z + z_{\text{offset}} + z_{\text{hub-target}}, \end{aligned} \tag{4.5}$$

where $z_{\text{hub-target}}$ is the distance between the front face of the FABLE hub and the target mount along the beam axis. This distance is indicated in Fig. 4.3.

At this point, the pixel location is determined relative to the nominal beam spot and we can convert to spherical coordinates:

$$\begin{aligned} r &= \sqrt{x^2 + y^2 + z^2}, \\ \varphi &= \arctan \frac{x}{y}, \\ \theta &= \begin{cases} \arccos z/r & z \geq 0, \\ \pi - \arccos z/r & z < 0. \end{cases} \end{aligned} \tag{4.6}$$

Telescope	F/B	η	ζ	ϕ_{mid}	x_{offset} (mm)	y_{offset} (mm)	z_{offset} (mm)	$z_{\text{hub-target}}$ (mm)
0	F	0°	45°	47.5°	2.5	−5.04	8.39	103.5
1	F	0°	45°	132.5°	2.5	0.46	8.39	103.5
2	B	0°	45°	227.5°	7.5	−0.46	−1.61	103.5
3	B	0°	45°	312.5°	7.5	−5.04	−1.61	103.5

Table 4.1 Table of geometric parameters relating to each FABLE telescope when arranged in the front-back configuration for measuring breakup in this work. F/B refers to whether or not the telescope is placed at forward or backward angles, η is the twist, ζ is the lean, and ϕ_{mid} is the azimuthal rotation of the detectors within the $x - y$ plane, as described in the text. The cartesian offsets for each detector are then indicated. Note that these are the relative offsets of the detectors after taking into account the beam spot offset, the procedure of which is described in Ch. 5.

The parameters used for FABLE geometry in the "forward-backward" configuration for the measurement of breakup fragments in this experiment are indicated in Table 4.1.

4.2 Energy Calibration

An early step in processing FABLE data is to calibrate its energy signals for each arc and sector within the array. FABLE ΔE channels were calibrated using a ^{232}U α-decay source and elastic scattering of ^{14}N on a ^{208}Pb target, which did not punch through the front detectors at a lab-frame beam energy of 56 MeV. The FABLE E_{res} channels were calibrated with the same alpha source with the ΔE detectors removed, but also with the scattering of ^{7}Be (at E_{beam} = 51.84 MeV), which does punch through the initial ΔE detector layer. All energies used in the calibration were corrected for energy loss through detector dead-layers (described below), energy deposition in targets, and in the case of the ^{232}U source spectrum, energy loss through a thin gold window, taking into account the positional information of the particle by the routine described in Sec. 4.1. This positional information was also used to determine the expected elastic scattering energy within each pixel.[1]

The ^{232}U source spectrum is shown in Fig. 4.4. Note that only peaks labeled 4-7 were used in the energy calibration, as these peaks were less sensitive to the dead-layer determination. Additionally, the ^{7}Be scattering point was not used for the ΔE detector calibration, only the E_{res} calibration. Additionally, the ^{7}Be elastic scattering points were not used to calibrate the backward-

[1]While virtual pixel matching between the ΔE and E_{res} detectors in FABLE is required for the energy calibration, a simple matching algorithm was employed for the energy calibration, assuming that a particle punches through parallel pixels in each detector. While this is not always true, this approximation is sufficient for determining an energy calibration. A more sophisticated pixelization routine, employed for the analysis of the experimental data, is described in Sec. 4.3 and Sec. 4.5.

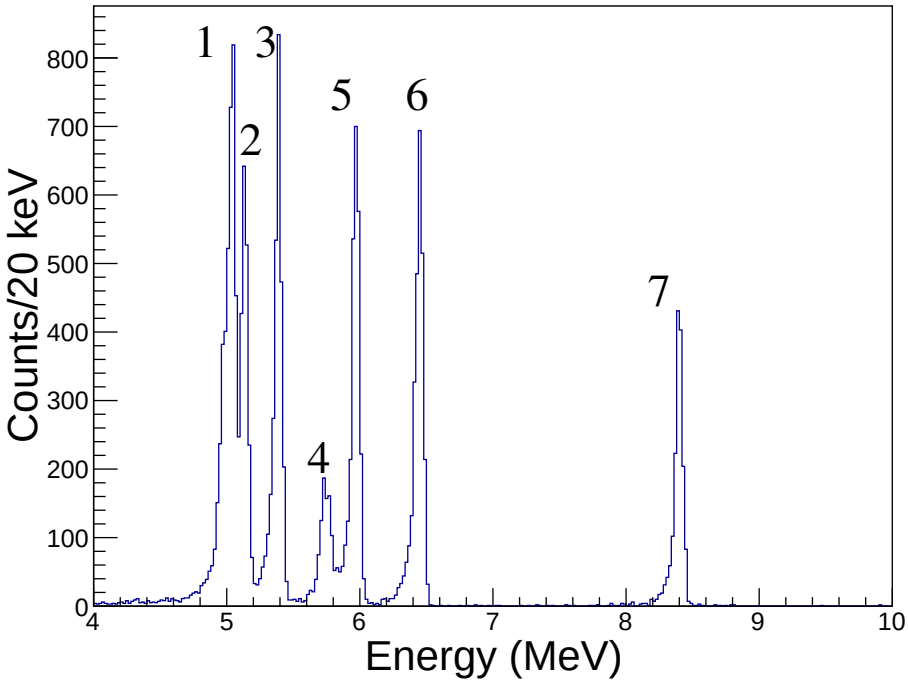

Figure 4.4 Calibrated source spectrum for ^{232}U measured in a single arc of FABLE. Seven peaks can be resolved clearly in most channels of the MMMs, but for consistent peak separation, only peaks 4-7 were used in the energy calibration for each segment.

angled detectors when the statistics were insufficient. Peak positions were determined by fitting range-limited Gaussians to each peak and using the mean fit parameter as the peak centroid.

The signals associated with arcs (junction side of the detector) are the primary energies used for the breakup analysis, but sectors (ohmic side of the detector) were also calibrated, albeit more poorly due to straggling through the DSSD. However, sector energies are only used in the virtual pixelization algorithm, while arc energies are used to reconstruct particle energies and reaction kinematics.

The FABLE dead-layers were determined in an iterative fashion by comparing the energy depositions of the source at different distances from the detector. At different distances, radiation enters the detector at different angles of incidence, and thus a different effective thickness of the dead-layer is experienced by the particle. Using this, one may determine a measured dead-layer by fitting to the energy difference and a function of the geometry. This, however, is dependent on the initial FABLE energy calibration. Thus, one may repeatedly calibrate the FABLE channel energies

Telescope	ΔE Al (F) (μm)	ΔE Si (F) (μm)
0	0.3	0.9
1	0.3	0.9
2	0.3	0.9
3	0.3	0.9

Table 4.2 Detector dead-layer thicknesses affecting the energy deposition within the ΔE DSSD of each telescope in FABLE. Each layer is labeled to indicate whether it is on the front (F) or back (B) of the active area of the detector.

Telescope	ΔE Si (B) (μm)	E_{res} Al (F) (μm)	E_{res} Si (F) (μm)
0	0.3	0.6	2.043
1	0.3	0.6	2.034
2	0.3	0.6	1.980
3	0.3	0.6	2.023

Table 4.3 Detector dead-layer thicknesses affecting the energy deposition within the E_{res} DSSD of each telescope in FABLE. Each layer is labeled to indicate whether it is on the front (F) or back (B) of the active area of the detector.

and redetermine the measured dead-layers until converging on a set of values such that the energy calibration curves are fully linear from low energy decay alpha calibration points to elastically scattered beam calibration points. The resulting dead-layers for the ΔE detectors are listed in Table 4.2 and for the E_{res} detectors in Table 4.3.

4.3 Pixel enumeration

Once FABLE's different channels have been energy-calibrated, the next step is the event-by-event position reconstruction. To do this, a program enumerates all possible hit patterns on the front ΔE detectors and all possible hit patterns on the back E_{res} detectors that *could* be paired with a front detector pixel and assigns coordinates to each hit enumerated based on the geometric localization of a hit within the coordinate framework described in Ch. 3. By "all possible hit patterns," I mean that there could be a perfectly reasonable back detector pixel constructed from signals, but if there are no signals on the front detector which could be reasonably correlated with the back, the back pixel should not be included in the enumeration. The reason for this is that there should be no usable physics events that correspond to a real particle landing in a back detector without first punching through a front detector. Therefore, the following conditions must be satisfied to enumerate a *possible* hit.

1. There is a ΔE arc with energy above threshold

2. There is a ΔE sector with energy above threshold on the same detector

3. To enumerate a possible $\Delta E - E$ pair, there must be an arc and a sector above threshold on the corresponding E_{res} detector, with pixels aligned within an acceptable margin. To accomplish this, the code requires $\text{abs}(n_a - n_r) \leq 1$ and $\text{abs}(n_s - n_j) \leq 1$, where n_a, n_s correspond to arc and sector segment numbers on the ΔE detector, and n_r, n_j correspond to arc and sector segment numbers on the E_{res} detector, respectively.

This process is also illustrated as a flow chart in Fig. 4.5. By using the prior criteria, the program enumerates a set of correlated hits and detector hit patterns, a subset of which corresponds to particle trajectories through the telescopes and we wish to keep for the analysis, but another subset will consist of spurious "junk" hits due to a variety issues, including cross-talk, charge sharing, induced charges, and pairing "double counts" (such events will be defined and addressed in the following section). Therefore, after we enumerate all possible hit patterns, we must begin cleaning and re-sorting the data to ensure only hits belonging to the former group are retained for further analysis.

4.4 Processing Hit Patterns

After enumerating all possible pixels and pairings within the requirements described in 4.3, the individual detector hit patterns are processed within the analysis code to handle possible complications in the hit enumeration (cross-talk, charge sharing, induced charge signals) on the ΔE and E_{res} detectors. For this, the ΔE and E_{res} detectors are treated *completely separately*, as these physical effects should only appear in the individual detectors rather than the full telescope. After handling these effects, another pixel-matching cycle is applied to choose which hit pattern enumeration between ΔE and E_{res} detectors is most appropriate. This step is referred to as *re-pairing* and is described in Sec. 4.5.

Before describing this hit pattern processing procedure, one can see the necessity of removing spurious events by inspecting arc and sector energy correlations in each detector of the telescope.

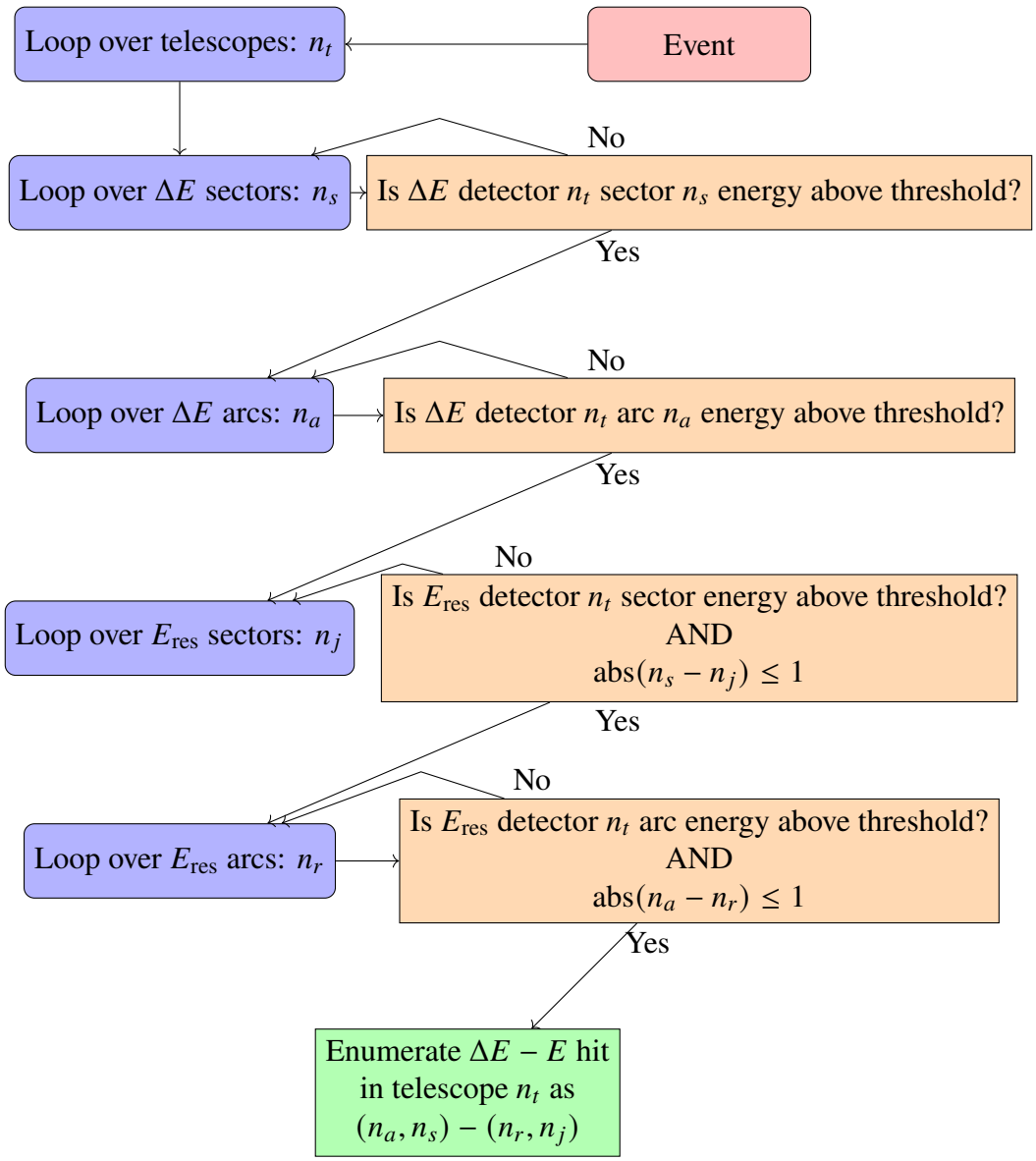

Figure 4.5 Flow chart of the hit enumeration process. Each colored block indicates a different "for" loop over the respective indices for each telescope, n_t, and within each telescope, its ΔE sectors, n_s, arcs, n_a and its E_{res} sectors, n_j and arcs, n_r. First, the analysis code loops over each event recorded in the run (pink). Each loop nexted within the decision tree for the event is indicated in lavender. First, ΔE detector hit patterns are enumerated in loops over the sector and arc segments. Then, this process is repeated for the E_{res} detector, with the requirement that $\text{abs}(n_r - n_a) \leq 1$ and $\text{abs}(n_s - n_j) \leq 1$. The decision gates are indicated in orange before proceeding to the next looping layer. If the decision gate is satisfied, the program follows the arrow indicated to the next step. Otherwise, it will proceed looping over the current loop. If all decision gates are satisfied, the $\Delta E - E$ hit is enumerated, as indicated in the green rectangle.

Figure 4.6a shows these energy correlations in the ΔE detector before the cleaning procedure to be described, and Fig. 4.6b shows the post-result. The magenta bars indicate the region of data where the energy correlations correspond to cross-talk in the detectors, which is significantly reduced following the procedure. This can also be observed in the corresponding plots for the E_{res} detector correlations are shown in Fig. 4.7a and Fig. 4.7b, respectively.

To process individual detector hit patterns, we assume that there is a maximum of two real fragments landing in coincidence in the DSSD, each of which produces at least one arc signal and one sector signal. That means that when we enumerate more than two possible hits in a single detector, spurious signals must be identified or the event must be discarded in total.

For the following discussion, I will focus on hits that are enumerated within the same detector, so when I mention arcs or sectors, hits or pixels, they are all contained within the same DSSD. The program applies the same method described in this chapter to all detectors separately. Here, I wish to introduce some nomenclature for the following discussion. N_a denotes the number of arc signals and N_s denotes the number of sector signals measured in the detector. Recall that each pixel consists of a pair of an arc and a sector on the detector, so I will denote individual pixels in this section with parentheses, and total numbers of arc and sector signals with square brackets, respectively. This means that $[2, 2]$ indicates $[N_a = 2, N_s = 2]$. The total possible enumerations before cleaning a [2,2] multiplicity event would include up to four potential pixels. If arcs i, j and sectors k, ℓ received signals, the possible enumerations would include *pixels* $(i, k), (i, \ell), (j, k), (j, \ell)$. For each case, I may focus on $[N_a = x, N_s = y]$ instead of $[N_a = y, N_s = x]$, but arcs and sectors are interchangeable, so both can be handled in the same manner.

4.4.1 $N_a = 1, N_s = 1$

This case, where there are signals in one arc and one sector, represents the base case for hit enumeration on the detector. If there is only one arc signal and one sector signal recorded, a single particle hit can uniquely attributed to a single pixel on the detector, as shown in Fig. 4.8. If there are any fewer signals recorded – that is, an arc without a sector or a sector fired without an arc ($\text{abs}(N_a - N_s) = 1$), we cannot enumerate a possible pixel and the associated signal should be

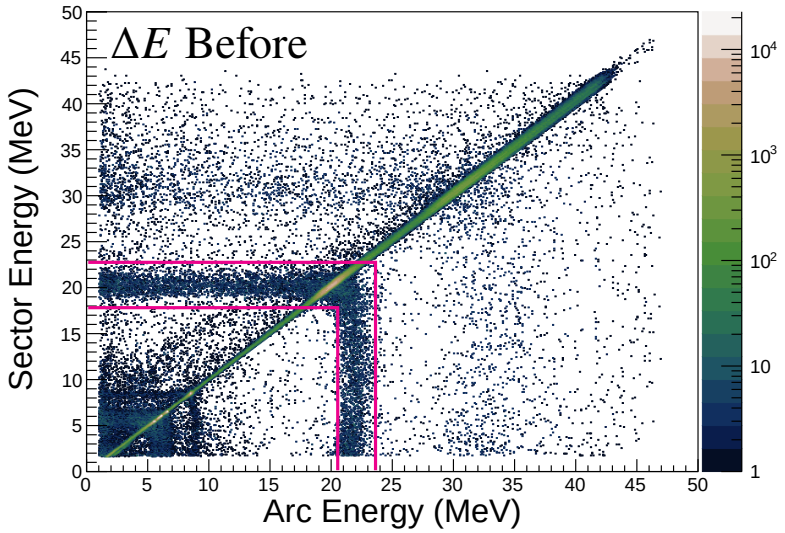

(a) Arc energy versus sector energy for enumerated pixels via the first step of the analysis pipeline. One can see bars of constant sector and arc energy. Bars such as those highlighted in the magenta region, are indicative of cross-talk between adjacent channels.

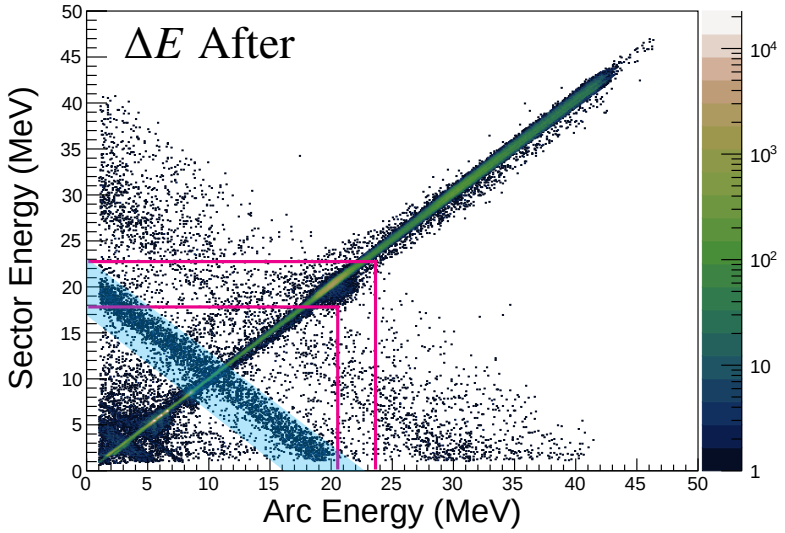

(b) Arc energy versus sector energy for enumerated pixels following rigorous repairing in the second step of the analysis pipeline. The bars of constant energy as shown in Fig. 4.6a have been significantly reduced, having the energies properly reconstructed, indicating improved pixel enumeration. During this process, some diagonally-barred charge sharing events are generated, such as those shaded in cyan, which could not successfully be reconstructed within the pairing algorithm limitations and must be discarded.

Figure 4.6 Arc and sector energy correlations within the ΔE detector before and after the hit pattern processing procedure described in Sec. 4.4.

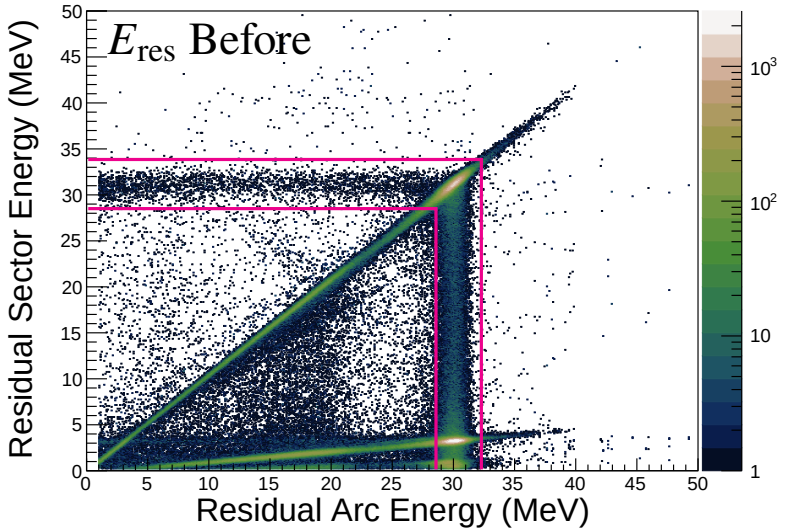

(a) Arc energy versus sector energy for enumerated pixels via the first step of the analysis pipeline. One can see bars of constant sector and arc energy. Bars such as those highlighted in the magenta region, are indicative of cross-talk between adjacent channels.

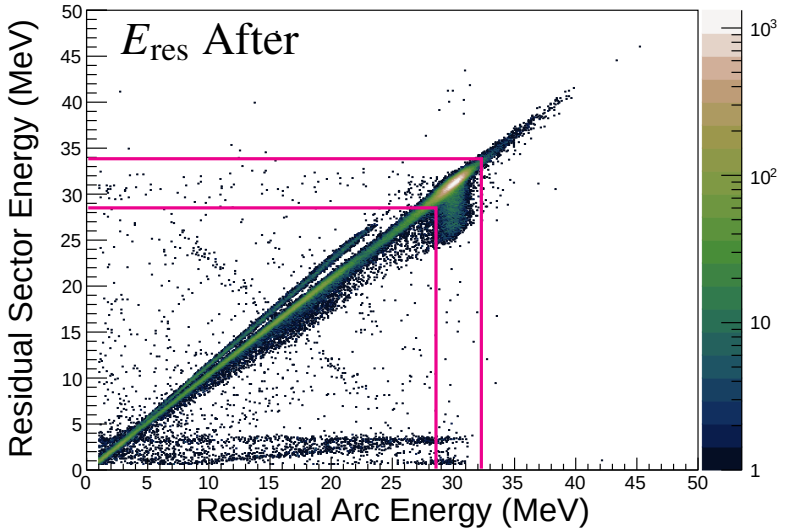

(b) Arc energy versus sector energy for enumerated pixels following rigorous repairing in the second step of the analysis pipeline. The bars of constant energy as shown in Fig. 4.7a have been significantly cleaned, indicating improved pixel enumeration.

Figure 4.7 Arc and sector energy correlations within the E_{res} detector before and after the hit pattern processing procedure described in Sec. 4.4.

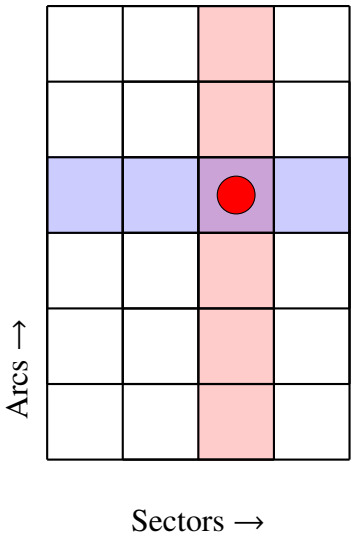

Figure 4.8 Base case for pixelization within the DSSD. Signals from only one sector (highlighted in red) and one arc (highlighted in blue) within a detector uniquely identify a single pixel in which a particle has landed, indicated with a red circle.

discarded. Additionally, $N_a > 0$ and $N_s > 0$ is required by the procedure described in the prior Sec. 4.3.

4.4.2 $N_a + N_s = 3$

Here is the first non-trivial case that necessitates cleaning. There are three signals in total: either $[N_a = 1, N_s = 2]$ or $[N_a = 2, N_s = 1]$. All signals in a single segment grouping, either $[N_a = 3, N_s = 0]$ or $[N_a = 0, N_s = 3]$ are discarded based on the procedure described in Sec. 4.3.

Let the following hits be recorded in the possible pixel enumeration for $[N_a = 2, N_s = 1]$: there are signals in two arcs, i and k, and only one signal in one sector, j, leading to two possible pixels being enumerated, (i, j) and (k, j). The analysis program must then identify which of the pixels correspond to true physics events, if any. This is because any of the following options could have occurred leading to the following hit pattern:

1. There were two breakup fragments which both landed in sector j, but different arcs i, k, as shown in Fig. 4.9. This would result in the energy associated with sector j being the sum of the fragment energies, but the energies in i, k having the individual fragment energies. This event can be recovered based on the arc energies E_i and E_k, and splitting the summed sector energy $E_j = E_i + E_k$ for assigning individual sector energies for each hit.

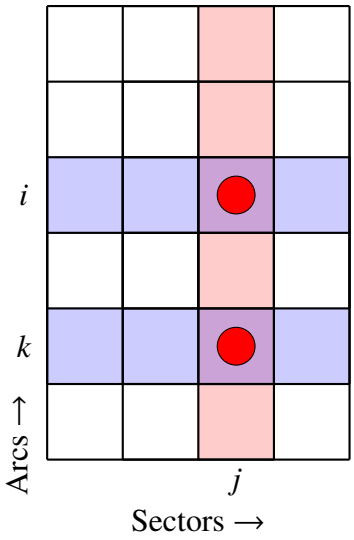

Figure 4.9 Hit pattern in the detector with two channels firing in coincidence with a perpendicular strip. The blue shaded regions indicate signals in various arcs, while the red shaded region indicates the sector firing. The red circles indicate each particle landing in a different part of the detector, leading to the enumeration of two separate pixels that share a sector. This hit pattern can results in the total energy in the sector being the sum of the arc energies: $E_j = E_i + E_k$. This event can be recovered by using the signals associated with the individual arcs as the basis for the formation of two different hits in the detector.

2. There was only one particle landing in one pixel, so sector signal E_j has a proper energy, but only one of adjacent arc energies E_i or E_k matches the sector energy. The other segment has provided a signal due to **induced charge** between adjacent channels ($i = k \pm 1$). In other words, this type of spurious signal when $k = i \pm 1$ and $E_j \approx E_i$, while $E_k << E_i$, if arc k has fired due to the induced charge. This case is illustrated in Fig. 4.10.

3. There was only one particle, but it landed in the boundary between adjacent ($k = i \pm 1$) arcs, so the sector energy E_j represents the full energy deposited by the particle, but only summed together do the arc energies E_i, E_k match the sector energy: $E_j \approx E_i + E_k$. The signals in the arc segments have been split due to **charge sharing** between the adjacent channels. This case is similar to induced charge signals in that $k = i \pm 1$, but differs in that the sector energy would be higher than each individual arc energy in the enumerated hits. Instead, the sector energy would roughly match the *sum* of the arc signal energies. Therefore, we combine sector energies and choose the pixel corresponding to the original higher energy segment for

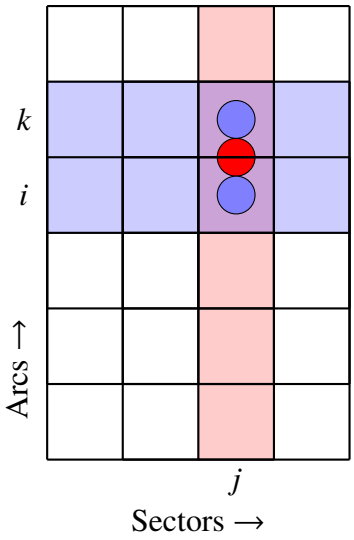

Figure 4.10 Hit pattern in the detector with two adjacent channels firing in coincidence with a perpendicular strip. The blue shaded regions indicate signals in various arcs, while the red shaded region indicates the sector firing. The red circle indicates the particle landing in the detector boundary, while the blue circles indicate possible pixel enumerations. This hit pattern can be associated with charge sharing, where a single fragment deposits its energy in both strips, illustrated here by the red circle. The energy can be summed to reconstruct the event. The hit pattern can also be associated with two particles hitting the detector in different arcs, but the same sector, as shown by the blue circles. This case can be identified by using the individual arc energies to match as the total sector energy.

the geometric enumeration.

4. Alternatively, it is possible that these hit patterns could be attributed to a single particle if there is induced charge or charge sharing in multiple segments. To eliminate this option, energy thresholds are carefully chosen to avoid enumerating this hit pattern permutation when there is only a single particle.

4.4.3 $N_a + N_s = 4$

For this case, we can have either $[N_a = 3, N_s = 1]$, $[N_a = 1, N_s = 3]$ or $[N_a = 2, N_s = 2]$. First, consider the cases where there are three arcs and one sector, which is illustrated in Fig. 4.11. Recall that this program assumes binary coincidence *at maximum* – it does not allow the scenario where there could be three particles hitting the same detector in coincidence. Therefore, up to two particles can be generating this hit pattern, as depicted by the groupings of either blue circles or red circles, indicating the possible hit combinations, in the figure, even though three hits would

be initially enumerated. One particle can cleanly hit the arc/sector pair, but the other generates an induced charge or charge sharing sub-case as discussed in the prior subsection 4.4.2, leading to a two-hit case. This can be verified by comparing energy depositions in the arcs and sector. Additionally, induced charges and charge sharing can lead to spurious signals in multiple segments, as discussed in the prior case, but the energy thresholds again serve to limit this possibility in the $[N_a = 1, N_s = 3]$ case.

However, for the $[N_a = 2, N_s = 2]$ case, things are more interesting, as there can be two real hits from breakup fragments, but two "ghost" events will also be enumerated in the possible pixel permutations. This is illustrated in Fig. 4.12, where the red and blue circles indicate two ways that particles could land in the detector and create the observed hit pattern. Again, recall the assumption of binary coincidence at maximum – this means that at most, two particles could punch through two pixels within a single detector. If they pass through completely unique arcs and sectors, this means two arcs and two sectors, which would net four possible pixels that will be enumerated, but only two should be chosen for further analysis. The correct enumerations are chosen based on minimizing the difference between arc and sector energies within each pixel.

4.4.4 $N_a + N_s > 4$

While it is possible to have more complicated hit patterns than those described in the prior sections, because of the requirement of binary coincidence at maximum, other hit patterns can be either discarded or reduced to the cases described in the prior subsections. If, with an abundance of segments, the hit pattern cannot be reduced on the basis of charge sharing or induced charges, the pattern will then be discarded. This occurred in fewer than 1% of events.

4.5 Rigorous Re-pairing

After the detector hit patterns have been processed for the cases discussed in Sec. 4.4, it is required to "re-pair" front and back detector pixels. This is necessary for several reasons. Firstly, if the reader recalls the initial hit enumeration routine illustrated in Fig. 4.5, all of the pixels are initially enumerated within a telescope, not just a single DSSD. In other words, the data structure representing each particle contains information from both the ΔE and E_{res} detectors. However, the

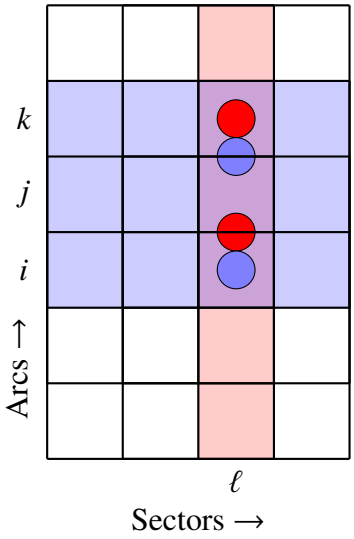

Figure 4.11 Case where there are three adjacent channels and one perpendicular channel firing. The blue shaded regions indicate signals in various arcs, while the red shaded region indicates the sector firing. The red circles indicate one possibility, where one particle shares its energy with two arcs and the other lands in its own separate arc and the blue circles indicate the alternative hit pattern of a similar scenario. This case is reducible after using the individual arc and sector energies to separate which hit can be clearly identified and then identifying the second hit based on the $[2, 1]$ cases discussed in the prior subsection.

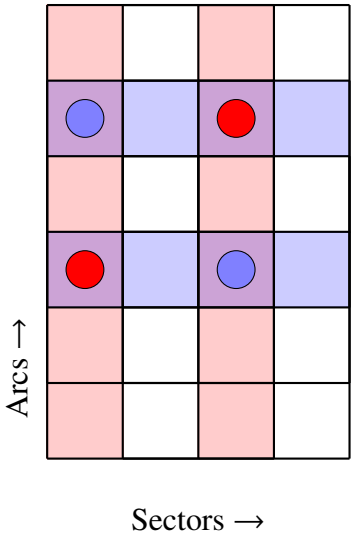

Figure 4.12 Case where there are two horizontal channels and two vertical channels firing. The blue shaded regions indicate signals in the arcs, while the red shaded region indicates signals in the sectors. Four possible hits can be enumerated from this hit pattern. Each grouping of particles landing in the detector is labeled by blue circles and red circles. Assuming binary breakup, this hit pattern implies that while all four pixels will be enumerated initially, two derived pixels result in the enumeration of ghost hits, and two correspond to true coordinates of the breakup fragments, as discussed in the text.

cleaning procedure described in the prior Sec. 4.4 treats information in the ΔE and E_{res} detectors *completely separately*. In fact, since they were separated for the hit pattern processing step described in the prior section, it is possible that the resulting hit patterns have decoupled former $\Delta E - E_{\text{res}}$ pairings that used to exist thanks to a spurious signal. Alternatively, it may make more sense to choose a new $\Delta E - E_{\text{res}}$ pairing after consolidating some particle energies that were initially split thanks to charge sharing or induced charges.

Additionally, potential pairing double counts that could have occurred in the original total hit enumeration step must now be taken into account. This occurs in the pixel enumeration step when a certain pixel for a back detector is used more than once in pairing possible combinations with different front detector pixels. This is analogous to the $[N_a = 2, N_s = 2]$ ghost hit problem discussed in the prior section, but rather than reducing permutations of segments within a single detector, one must reduce permutations of pixel pairings *between* detectors within a telescopic pair. See Fig. 4.13 for a visual representation of this issue. After cleaning the individual detector hit patterns, when we re-combine front and back correlated hits, it is therefore critical to use each enumerated pixel only once to ensure that no double counting occurs.

Finally, note that the pairing step alone cannot follow the "cleaning" procedure described in Sec. 4.4 in this work. While this simpler process is reasonable when one can hold stricter pairing requirements (e.g. parallel pixel requirements between ΔE and E_{res} detectors) and has been used in prior stable beam studies, "pairing" inefficiencies between each detector in the telescope (also discussed in Sec. 6.4.1) and the low beam intensity of this experiment necessitated further optimization in the sorting algorithm such that more permissive pairing was allowed. Once the parallel pixel criterion is loosened, initial pairing between the ΔE and E_{res} detectors is necessary to reduce the multiplicity of the sorting problem such that it is tractable without needless discarding of good hits.

Recall that in the detector cleaning step, channel contents may have changed according to induced charges or charge sharing being identified and corrected. Therefore, the possible hit pairings are re-enumerated and evaluated on whether or not one $\Delta E - E$ pairing is optimal compared

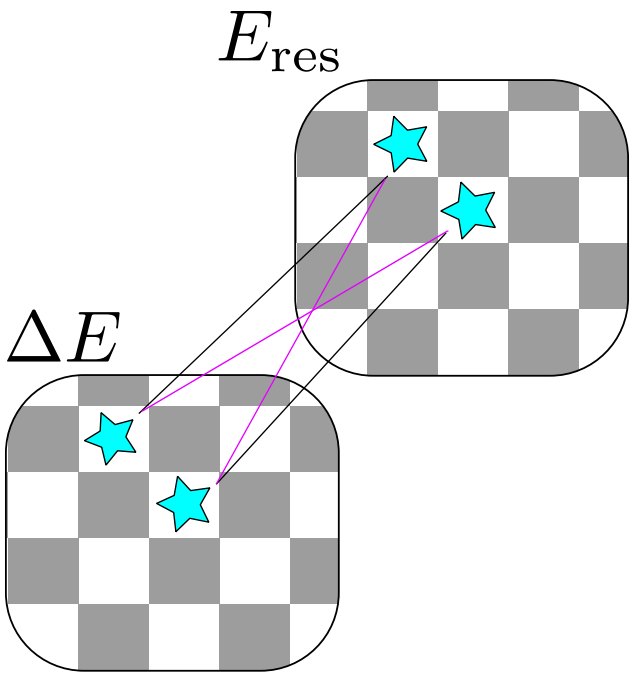

Figure 4.13 Example of the double count pairing problem. Two pixels are enumerated on the front ΔE detector and back E_{res} detector, respectively, indicated by teal stars. The possible pairing correlations of front and back pixels are indicated by black and fuchsia lines. Choosing the correct correlations is critical for correct kinematic and geometric reconstruction of breakup fragments.

to another possible pairing. Note that due to the ordering of the ΔE and E_{res} detectors, there will only be situations where there are more ΔE pixels enumerated that must be reduced down, rather than vice versa. The following criteria are used in this evaluation procedure of reducing *possible* hit patterns to a single hit pattern:

1. Are the candidate pixels likely valid hits? Ghost hits may have one good pixel ($E_A - E_S \approx 0$) and one bad pixel enumerated in correlation and should be discarded, making the re-pairing step simple. See Fig. 4.13 for an illustration of this issue.

2. Are front and back detector pixels to be correlated reasonably close to each other in (θ, ϕ)? Ideally, this should always be true for perfect alignment and parallel mounting between the ΔE and E_{res} detectors within the telescope, but due to flaws within the mechanical mounts for FABLE, this is not guaranteed. Additionally, even with perfect alignment, the FABLE DSSDs are all identical in size, which means that mounting them in any telescopic configuration will result in small differences of (θ, φ) for the same pixel. Lastly, because the beamspot was

off-center on average by several millimeters (as discussed in Ch. 5), depending on the angles at which a charged particle resulting from reactions with the target, passes through each detector, it should be expected that the firing segments will not always perfectly match, even if it should be *expected* for a majority of events. This alignment association is then determined by proxy via difference in arc and sector numbers between the front and back pixels. The expectation that a charged fragment passes through both detectors relatively straight, such that the difference in arc and sector number is minimized between each detector in the telescope, is used as a "tiebreaker" in the sorting algorithm when the pixel energies are reasonable. Of the fewer than 0.4% of hits which have ambiguous $\Delta E - E_{\text{res}}$ pairings at this stage, 33% of those events have their pairing decided according to the tiebreaker criterion.

3. If competing hits have equidistant pixel separation between the ΔE and E_{res} detectors, a final tiebreaker for determining paired pixels is the energy agreement between arc and sector segments for each ΔE pixel (fewer than 1% of events). The pixel with the best energy agreement is chosen as the candidate for pairing with the E_{res} detector pixel.

After this re-pairing is completed, we are left with uniquely paired $\Delta E - E$ events with which we can carry out the remaining analysis. Once particles hitting detectors have been assigned appropriate coordinates and coincidence levels, we now have positions and energies for each event.

4.6 Position and Energy of Singles Charged Particles

Following the energy calibration described in Ch. 4.2, pixel enumeration and pattern matching as described in this chapter, and geometric associations between the pixels and lab frame coordinates as described in Ch. 3, every single particle recorded should have its total energy and the location of its trajectory into FABLE described within the analysis framework. Total energy, E, versus lab-frame scattering angle, θ, for all data recorded in the ^{7}Be runs is plotted in Fig. 4.14. Here we can see elastically scattered beam at the highest energies, along with $Z = 2$ breakup fragments at intermediate energies and $Z = 1$ particles at lower energies.

These associations can be confirmed using the $\Delta E - E$ particle identification plot, shown in

Fig. 4.15. For lower-energy fragments, this figure has been zoomed in Fig. 4.16. Note that in the particle identification plots, the ΔE for each particle is multiplied by a factor of $\cos(\beta)$. This scaling adjusts for energy lost in the detector depending on the angle of incidence to enhance separation between each isotope band.

One should note that in the identification of some of the $Z = 2$ breakup fragments and many of the $Z = 1$ breakup fragments, the band of events folds over. This is occurs when the particle has sufficiently high energy that it does not deposit its full energy and stop in the E_{res} detector along its forward trajectory. As a result, these "punch-through" events have the expected ΔE energy deposition, but a smaller E_{res} deposition according to the particle energy. Such events were gated out for the purpose of analysis since their full energy cannot be reconstructed, but there are instances at the beginning of the knee in each particle band where there is some ambiguity of where to draw each particle gate such that one does not any events where the band has already "folded," indicating punch-through and leading to mistaken energy reconstruction. Such events must be considered in the coincidence analysis to ensure that exit channels of breakup are properly identified and reconstructed, or if not, discarded. This process is discussed in Ch. 6.

However, there are some other features in these figures that should be discussed. One may notice that at the most forward and backward angles in Fig. 4.14, a significant amount of particles near but below the beam energy appear with an intensity of the same magnitude of the elastic scattering. In Fig. 4.15, the population of ^{9}Be has been identified and labeled, which correspond to the aforementioned particles in the angular distribution. This can be attributed to an unfortunately offset and misshaped beam profile. This offset beam caused a variety of issues which are discussed in more detail in Ch. 5, but for now, what is noteworthy is the production of ^{9}Be by way of $2n$ pickup off of the aluminium target frame. There are also some light impurities due to reactions with oxygen and carbon visible at forward angles between $20 - 30$ MeV, indicated in the cyan box in Fig. 4.14. By gating in the $E - \theta$ matrix similar to the region indicated by the cyan rectangle, but drawn more tightly in combination with gating in the particle identification plot, these particles can be removed from the breakup data. Also, in Fig. 4.14, kinematic lines for the elastic scattering

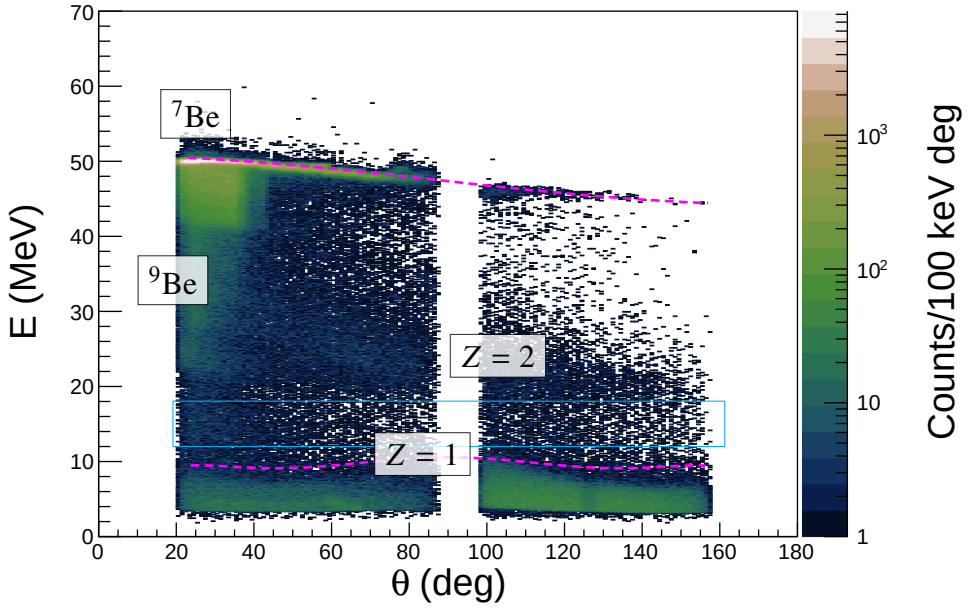

Figure 4.14 Energy versus scattering angle for charged particles measured in the reactions of ^{7}Be on ^{208}Pb, where the color axis plots the counts per bin. The dashed magenta line at high energy indicates the kinematic line for elastic scattering, and at low energy indicates the upper $Z = 1$ fragment threshold. The kinematic curves were calculated using CATKIN [35]. Ejectiles resulting from reactions with impurities in the target (oxygen, carbon) can be seen in the region indicated with the cyan rectangle, but can be gated out in this spectrum.

of the ^{7}Be beam near 50 MeV and the upper threshold of $Z = 1$ breakup fragments is plotted near 10 MeV, which were calculated using CATKIN [35]. By gating on the ^{7}Be and $Z = 1$ breakup fragments in the particle identification, these data match the kinematic lines and serve to provide further confirmation of the position and energy determinations.

4.7 Conclusion

In this chapter, the program by which FABLE signals are processed and analyzed as particles with energies and positions in coincidence was detailed. The singles spectrum of ^{7}Be reacting with ^{208}Pb at $E_{\mathrm{CM}} = 50.05$ MeV was shown. In the next chapter, I will discuss the handling of a beam offset determination, which is required to properly reconstruct the kinematics of breakup in Ch. 6.

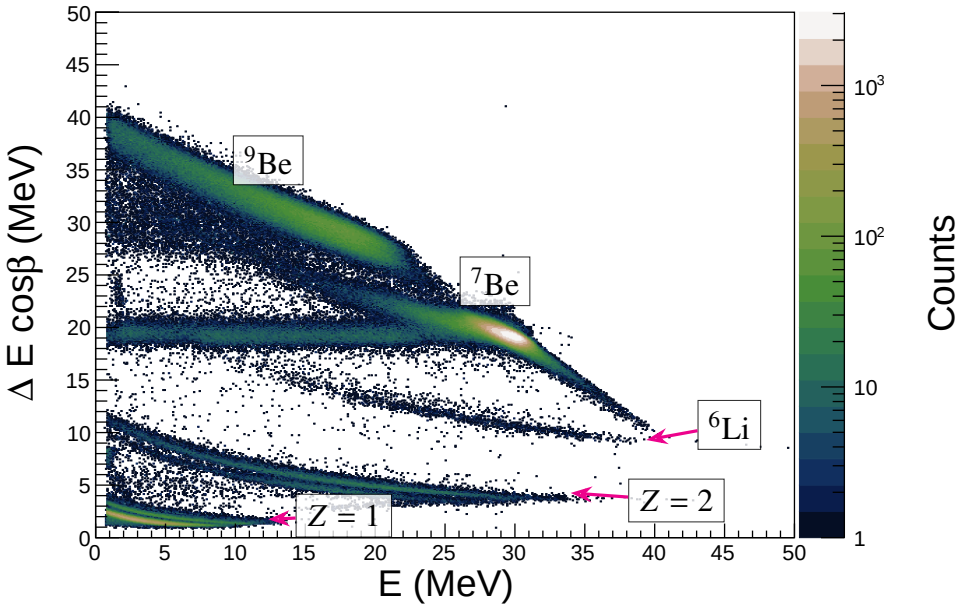

Figure 4.15 Particle identification matrix for singles events achieved by plotting the ΔE corrected for the energy loss by angle of impingement β against the residual E.

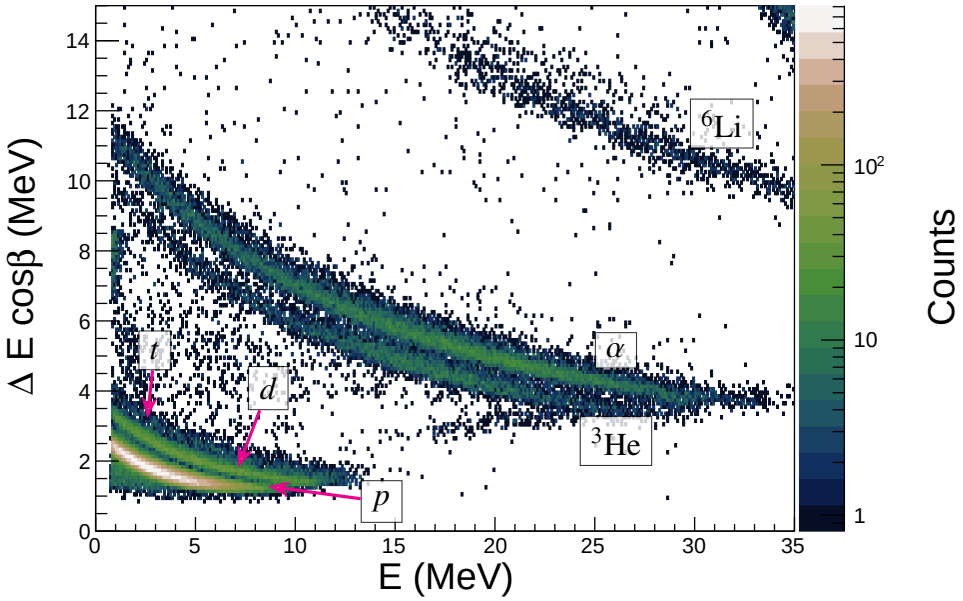

Figure 4.16 Particle identification matrix for singles events achieved by plotting the ΔE corrected for the energy loss by angle of impingement β against the residual E, zoomed into energies focused on $Z \leq 2$ particles.

CHAPTER 5

BEAM SPOT RECONSTRUCTION

5.1 Introduction

The beam spot for this experiment was not optimal in profile and position. Note that the coordinate system defined in Sec. 4.1 requires us to define the origin relative to the average reaction site. An off-axis beam spot introduces issues in the analysis in kinematic reconstruction of breakup and when determining an accurate evaluation of the solid angle of the detectors, which is critical to extracting valid cross sections, as will be discussed in Ch. 6. Therefore, a rigorous determination of the beam spot relative to the detector positions is required.

I should mention here *why* a beam offset correction was necessary for these data. There are two pieces of evidence. The first piece of evidence is that skewness of what should be a uniform distribution in φ can be observed in the distribution of the elastics at forward scattering angles. Elastic scattering data, gated on the ^{7}Be in $\Delta E - E$ and scattering angles ranging $\theta \in (36°, 38°)$ are

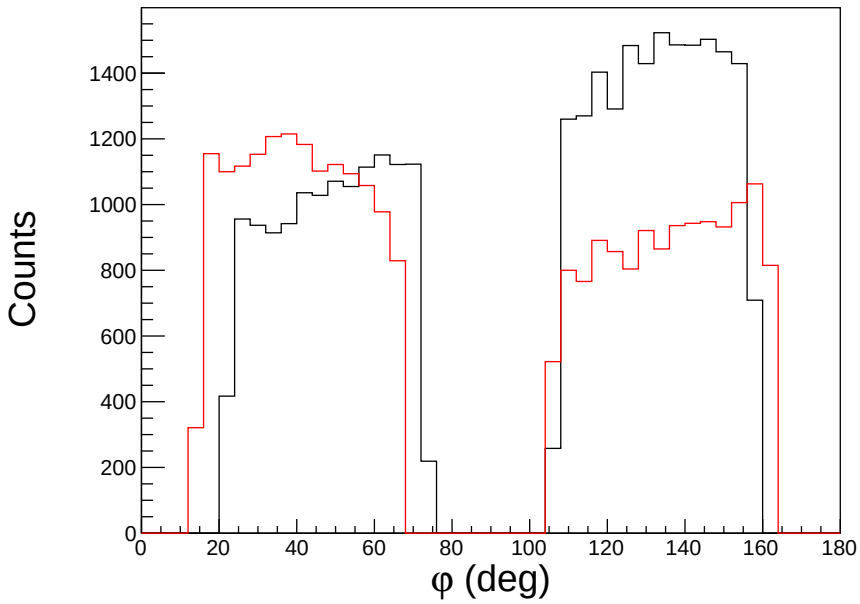

Figure 5.1 Comparison between the φ distribution of elastic scattering of ^{7}Bebeam at $\theta_{\text{lab}} \in (36°, 38°)$ before (black) and after (red) offset corrections. The offset correction shifts the detectors in space slightly and results in a far more uniform distribution expected for elastically scattered beam.

shown in Fig. 5.1. In black, the elastic distribution is shown without a beam offset correction and there is a large slope in the distribution. In red, the resulting φ distribution following beam offset correction is shown. While the correction does not result in a uniform distribution still, the slope has been significantly reduced compared to the data without the offset adjustment. Additionally, the strong population of ^{9}Be at forward angles suggests that we are populating $2n$ pickup with a thick target. Specifically, instead of reactions with the thin ^{208}Pb target, these reaction products instead were resulting from impingement upon the thick aluminum frame in which the target was housed. The consequence of this thick frame, when combined with the beam offset, results in the observed skewing of elastics at forward angles with some azimuthal dependence. If one must work with an unshapely or off-center beam, ideally, one would measure it with some sort of position-sensitive detector. These data could not be measured with a beam tracking detector, since the anticipated beam currents were too high to permit 0° tracking. Careful beam tuning was to be achieved by tuning through a 3 mm aperture onto a Faraday cup, but this was not possible with the much lower beam rate and profile actually delivered during the experiment. Therefore, we were forced to determine the beam position offline.

5.2 Procedure for Beam Offset Determination

The offset of the beam was quantified by leveraging the azimuthal independence of the elastic scattering cross section. For small slices in the scattering angle, θ, the φ-distribution should then be roughly uniform along our detectors. Therefore, we can determine the correct beam offset by intentionally offsetting the detector geometry in the opposite direction and reprocess the data to find the correct geometry which leaves our φ-distribution uniform.

Sphere point picking was used to emulate the isotropic emission from a target (with a nonzero offset from an origin in the chosen coordinate system, ultimately arriving at the detector offsets described in Table 4.1), which was then filtered through FABLE's geometric acceptance. The resulting φ distribution, should match that of the measured elastic distribution shown in black in Fig. 5.1. This process is illustrated in the flow chart in Fig. 5.2. Then, by minimizing the difference between the simulated and observed φ distributions, the correct offset of the average reaction site

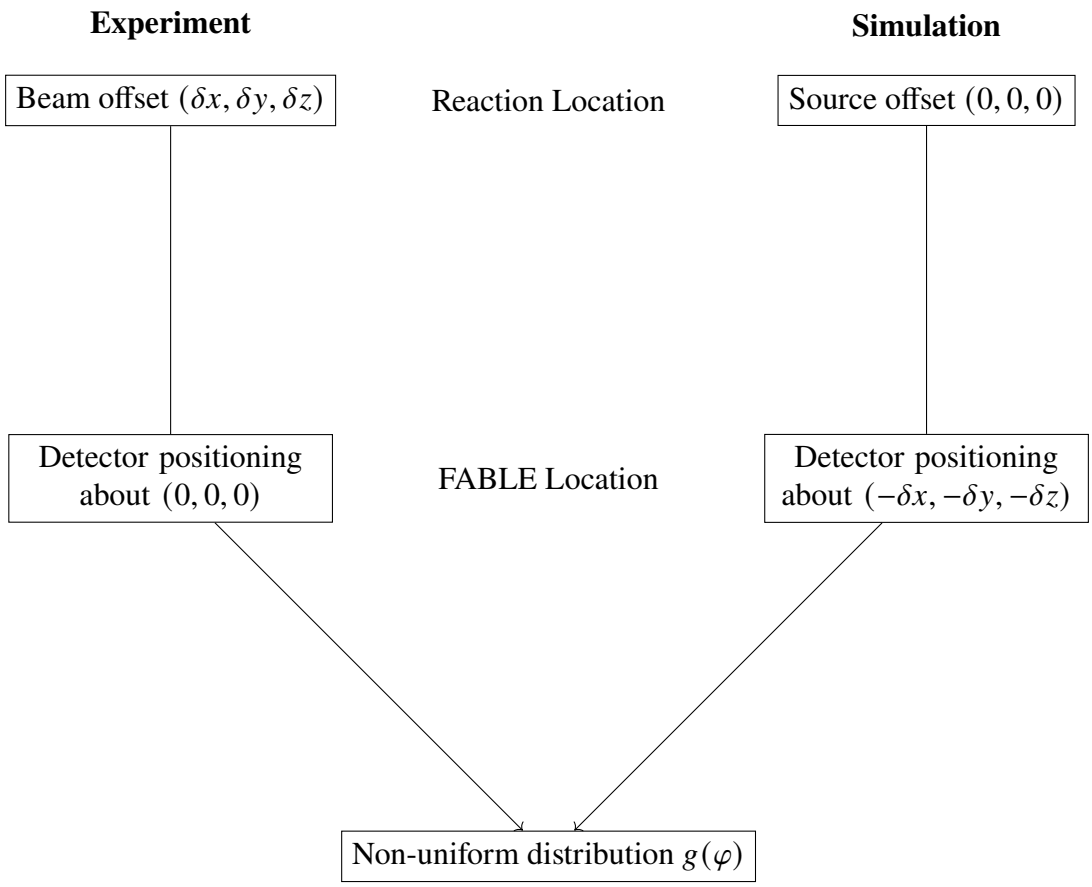

Figure 5.2 Flow chart illustrating how the relationship of the beam positioning/average reaction site and the detector positioning within the coordinate system can be manipulated to yield the same yield distribution.

was extracted.

I also employed a brute-force empirical approach to verify the beam offset that I determined through the above method. We have a reasonable understanding of what elastic scattering-to-Rutherford ratio of cross sections should look like – near unity at forward angles, with a steep drop after the grazing angle, which then smooths out to a small but steady decline. This understanding can be leveraged to develop a metric for evaluating the validity of an offset choice.

An example cross section ratio plot for an arbitrary, incorrect offset is shown in Fig. 5.3, with two linear fits indicated to evaluate the "reasonability" of the offset. The first fit, at forward angles, gives linear fit parameters, with offset, b_1, and slope, m_1. Ideally, $b_1 \rightarrow 1$ and $m_1 \rightarrow 0$ to capture the roughly unity Rutherford ratio behavior expected at forward angles. Meanwhile, the second fit, with parameters b_2 and m_2, is used to enforce the smoothness and continuity along the detector

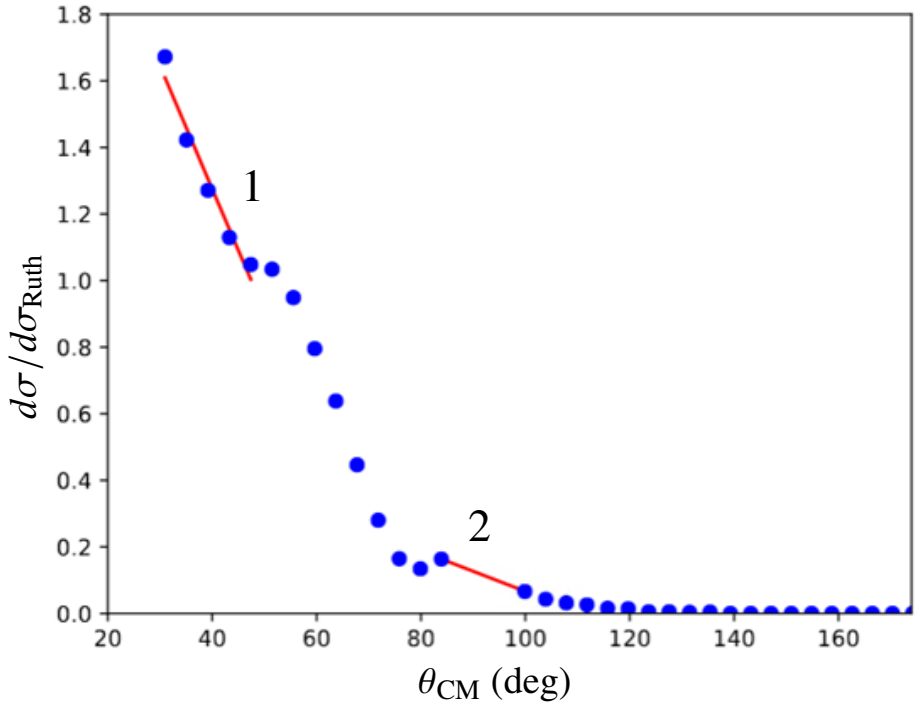

Figure 5.3 Example of the elastic-to-Rutherford cross section ratio for an arbitrary, incorrect offset to demonstrate how the indicated linear fits were used to evaluate the viability of the offset.

coverage gap. For this, one expects m_2 to be small and negative. To this end, I assert the following cost function based on this heuristic understanding:

$$C = |m_1| + |m_2| + |b_1 - 1|, \tag{5.1}$$

where C, the cost heuristic, is a simple sum of the magnitude of the linear fit parameters at very forward angles and the level of change at the discontinuity point in detector coverage between front and back angle detectors. The idea is that the slopes in these two spots should be near zero and that the y-intercept should be near unity to capture the normalization appropriately. However, I emphasize that this optimization method is based on a *heuristic* and can only be appropriately understood within the context of the data – the skewing of the elastics specifically was used to roughly localize the beam spot near the edge of the target frame. The heuristic evaluation method was only used to cross-validate the first result. This method can be evaluated over the sum of detectors as well as individual detector yields. The results of the offset search by heuristic

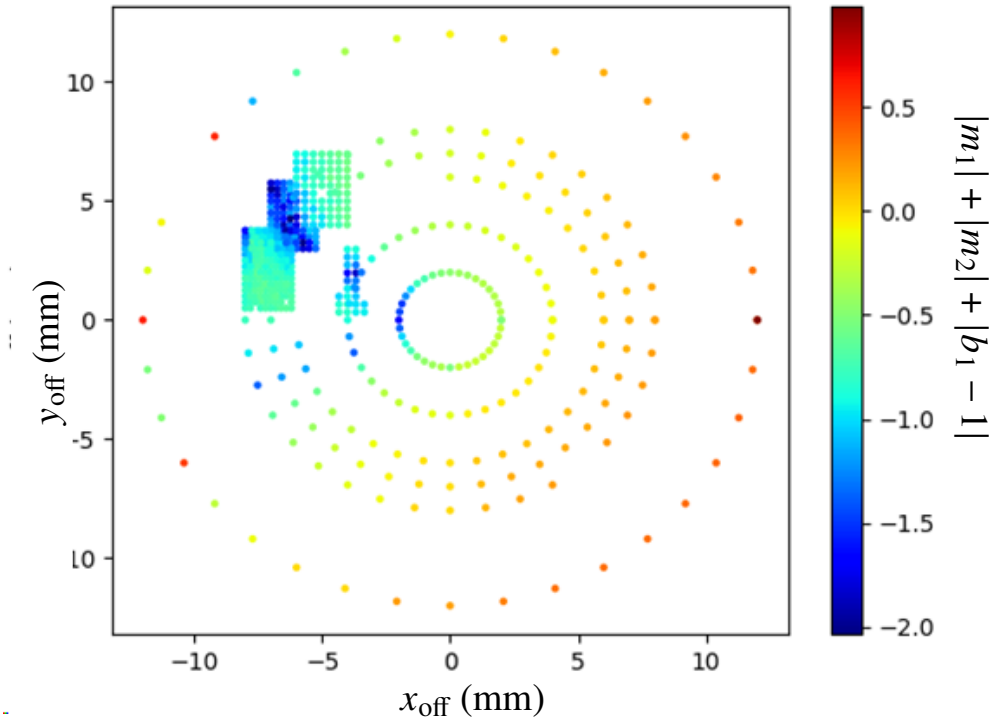

Figure 5.4 Results of offset search based on the heuristic described in Eq. 5.1. Low values indicate a better offset choice.

evaluation are shown in Fig. 5.4.

Through both methods, I ultimately settled on implementing an offset of $x \rightarrow x - 5$ mm and $y \rightarrow y + 2.75$ mm to the detector translational offsets. The difference of the beam offset correction is evident by comparing the ratio of elastic scattering to Rutherford without (blue) and with (green) the offset correction, shown in Fig. 5.5. The ratio without the offset correction has a peaking shoulder near 20-30° and another shoulder in the region of discontinuity between detectors near 100°, which are symptoms of distortion in the solid angle of the detectors due to the beam offset. Following the corrections, both shoulders are smoothed out and there is improved continuity in the measurement between the forward-angled and backward-angled detectors.

Note that while the offset is presented here in Cartesian coordinates, one could define the offset in polar coordinates in the $x - y$ plane, as well, since $x = r_{\text{off}} \cos \phi_{\text{off}}$ and $y = r_{\text{off}} \sin \phi_{\text{off}}$, where r_{off} is the radial offset and ϕ_{off} is the angle of the offset in the x-y plane. The heuristic is more sensitive to changes in ϕ_{off} than r_{off}, which can be seen by inspecting Fig. 5.4. Therefore, offsets within ±0.5 mm along ϕ_{off} in each direction were also tested, but the normalization based on forward-angled

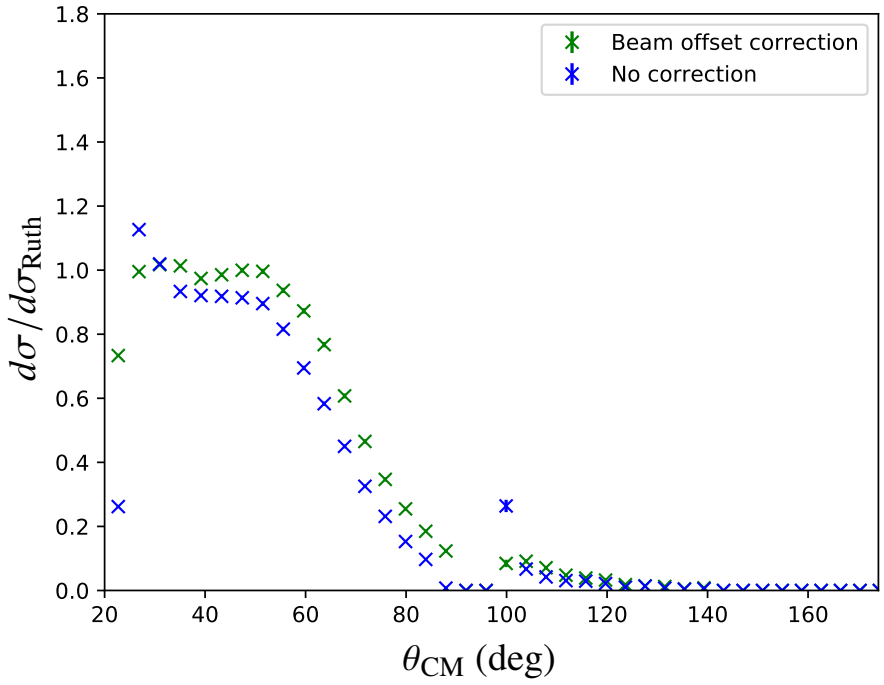

Figure 5.5 Ratio of elastic scattering cross sections to Rutherford cross sections plotted for the scattering of ^{7}Be on ^{208}Pb with and without the beam offset correction.

data of the elastic-to-Rutherford ratio was not sensitive to these offsets beyond uncertainty.

To achieve proper normalization with elastic scattering yields, the beam spot center-of-mass position relative to the detectors must be taken into account. Recall that the target is angled at 45° relative to the beam axis. If the beam were off-center when impinging on the target, the resulting reaction sites would be shifted both along the beam axis (strongly affecting the solid angle between front and back detectors) as well as orthogonally (primarily affecting the solid angle at detector edges). Explicitly, this means that any offset applied on the horizontal x-axis should also be applied along the beam axis and of opposite sign for forwards versus backwards angle detectors. See Sec. 4.1 for a thorough explanation of the coordinate system for describing reactions relative to FABLE. This also means that horizontal shifts in the beam spot result in the displacement of the average reaction site along the beam axis, further changing its positioning relative to the detectors. This can be observed in Fig. 5.4, where the heuristic parameter changes more rapidly with offsets along only the x-axis compared to those just along the y-axis.

With the beam offset properly determined, we can now continue forward with the analysis. Knowledge of the location of the average reaction site is critical for proper kinematic reconstruction of coincidence measurements of breakup, which will be discussed in the next chapter.

CHAPTER 6

EXTRACTING NO-CAPTURE BREAKUP YIELDS

6.1 Introduction

In Ch. 4, the analysis procedure was described for turning signals recorded within FABLE into events with position and energy data, ready for analysis. The singles spectra were reviewed and particle identification via $\Delta E - E$ was demonstrated. With these particle identifications, positions, and raw energy signals, the reaction kinematics can be reconstructed in coincidence events. The goal is to then extract breakup yields, and then cross sections, from this information.

In this chapter, I will discuss the procedure for identifying signatures of different breakup modes in the experimental data and simulations performed with *KOOKABURRA* to aid in the interpretation of these various spectra. Additionally, comparisons between experiment and simulation kinematics ensure that realistic breakup has been simulated for the purposes of coincidence efficiency determinations. I will then discuss the efficiency determination and normalization routines used to eventually extract cross sections that take into account the efficiencies of the detectors in singles and coincidence modes. Finally, the validity of the simulations will be established by an examination of the breakup functions.

6.2 Identifying Breakup Channels

Each event in FABLE data can store multiple hits in the array in coincidence, as discussed in Ch. 4. By gating on the $\Delta E - E$ particle identification for each hit, the exit channels of breakup were identified. However, it is necessary to leverage additional information in the kinematic reconstruction to separate different resonances populated prior to projectile decay. This allows separation of asymptotic and near-target breakup, as discussed in Ch. 2. Additionally, this insures that the breakup kinematics are reconstructed properly and to confirm each breakup mode being examined, including the removal of products due to reactions with light impurities in the target by gating in both $E - \theta$ and $Q - E_{\mathrm{rel}}$. Finally, separation of each breakup channel by resonance allows verification of the simulations used for determining coincidence efficiencies, which will be

discussed in Sec. 6.6.

One must confirm that the breakup fragments measured are due to reactions with the ^{208}Pb target rather than light impurities. Since the relative energy reveals the excitation of the projectile prior to breakup and the Q-value reveals excitations within the target, as discussed in Ch. 2, the combination of the two allows for examination of excited states in both the projectile and target nuclei. See, for example, Fig. 6.1, which shows the $Q - E_{\mathrm{rel}}$ matrix for the ^{8}Be breakup channels in the experimental data. There is separation between the 0^{+} and 2^{+} resonances in relative energy. This can be seen more clearly in the one-dimensional projection in relative energy, shown in Fig. 6.2.

Also, note that there is a matching distribution of Q-values for both resonances, up to roughly $Q = 12$ MeV. Recall that the ground state-to-ground state Q-value for $^{7}\mathrm{Be} + {}^{208}\mathrm{Pb} \rightarrow \alpha + \alpha + {}^{207}\mathrm{Pb}$ is $Q_{gg} = 11.6$ MeV and in this case, $Q_{\mathrm{opt}} = 0$ MeV. Recall that the Q_{opt} (defined in Eq. 2.18 goes to zero when the charges of the projectile and target remain unchanged in the exit channel. In other words, neutron transfer reactions, the optimum Q-value is zero, which drives the distribution of reconstructed Q-values to be centered about zero.

Meanwhile, Q_{gg} should be the upper limit of the reconstructed Q-value. There are some slightly higher Q-values reconstructed due to some smearing in the reconstruction. This can be attributed to randomization of each particle position within the pixel, which in turn randomly changes the angle of incidence used in energy reconstruction.

While Q_{gg} sets the upper limit of Q-values for each exit channel, it is possible to reconstruct higher energy Q-values. Such cases occur when the full energy of a particle is not deposited in the detector. This is observed primarily in higher-energy $Z = 1$ fragments, as discussed in Sec. 4.6. If one gates on such "punch-through" events in the exit channel, the full energy of the particle is not represented in the measured data, such that the reconstructed Q-value will be spuriously high after inferring the recoiling target's energy. Therefore, Q-values significantly higher than the Q_{gg} are gated out in the enumeration of breakup yields.

Due to target-like excitations, the Q-value can be smaller than this ground state-to-ground state

Exit Channel	Q (MeV)	E_{rel} (MeV)
$\alpha + \alpha$	(-12,12)	(0,10)
$\alpha + {}^{3}\mathrm{He}$	(-3,1)	(0,10)
$\alpha + d$	(-20,-2)	(0,10)

Table 6.1 Boundaries of gates in $Q - E_{\mathrm{rel}}$ for each exit channel to ensure that tabulated yields are products from reactions between the projectile and target with correctly reconstructed kinematics.

Q-value, in discrete levels corresponding to the recoiling nucleus' structure. However, the levels of ^{207}Pb cannot be resolved in the figure due to a lack of statistics and resolution. While the energy resolution of the silicon detectors is about 40 keV, the reconstructed Q-value resolution depends not only on the energy resolution of the breakup fragments, but also the positional resolution. This results in a broader Q-value reconstruction, approximately 700 keV in full width at half maximum, which washes out the structure of the recoiling target-like nucleus in this work. Q-values much lower than the optimum Q-value are unlikely to be associated with reactions between the beam and target and instead can be attributed to reactions with the beam and light impurities in the target. These events should not be counted in the final enumeration of breakup yields for a given mode and are gated out in cross section determinations. The boundaries of the gates in $Q - E_{\mathrm{rel}}$ for each exit channel are shown in Table 6.1.

The corresponding spectra for $\alpha + {}^{3}\mathrm{He}$ and $\alpha + d$ exit channels are shown in Figures 6.3 and 6.4, respectively. For $\alpha + {}^{3}\mathrm{He}$, there is no transfer reaction prior to breakup, so the expected Q-value distribution should just be a sharp peak at the breakup threshold, and if there were more statistics, one might expect to resolve smaller peaks at lower Q-values associated with the low-lying excited states of ^{208}Pb that may be populated in the process. For the $\alpha + d$ exit channel, $Q_{\mathrm{opt}} = -12.08$ MeV and the ground state-to-ground state Q-value is $Q_{gg} = -3.28$ MeV. Therefore, we see in Fig. 6.4 that the distribution starts around 3 MeV and is centered near the optimum Q-value, around -12 MeV.

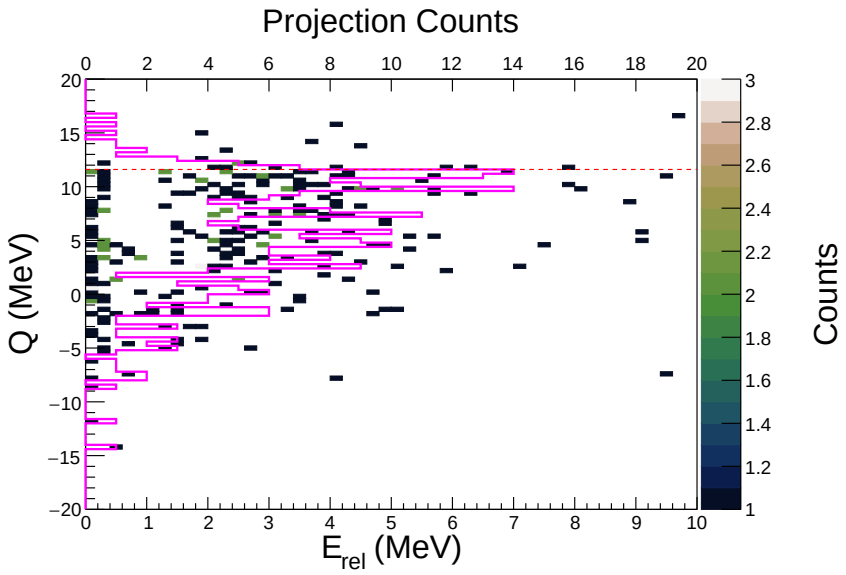

Figure 6.1 Plot of reconstructed Q-value versus relative energy for the $\alpha + \alpha$ exit channel. The one-dimensional projection of the Q-value is plotted in magenta along the y-axis. The maximum expected Q-value, indicated by the red, dashed line, is $Q_{gg} = 11.6$ MeV. This is based on the ground state-to-ground state Q-value for transfer and then breakup. One can also observe two distinct groups in these data based on the relative energies – a simple cut at 500 keV largely separates breakup resulting from the 0^+ and 2^+ resonances in ^{8}Be.

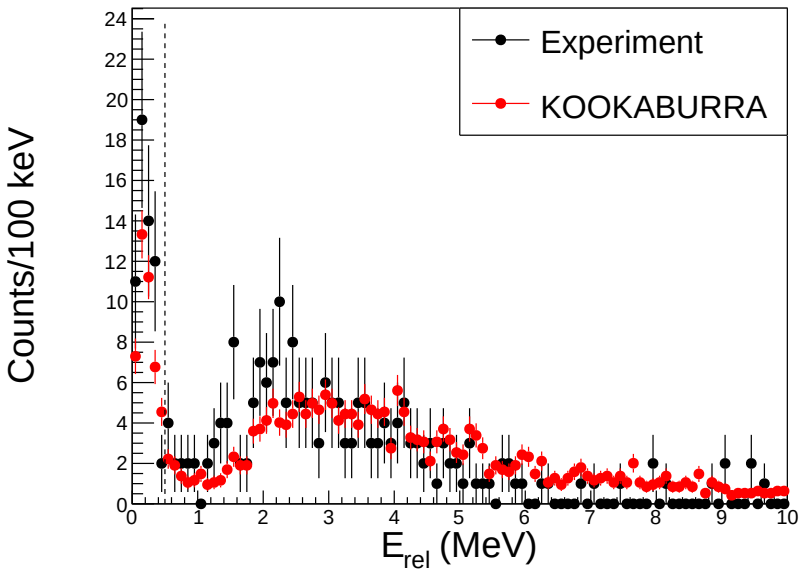

Figure 6.2 Relative energy spectrum for the transfer-triggered breakup of ^{8}Be $\rightarrow \alpha + \alpha$. In black are the experimental data and in red are the simulated data from *KOOKABURRA*, scaled down to match the statistics of the measurement. Error bars are statistical for both measured and simulated data.

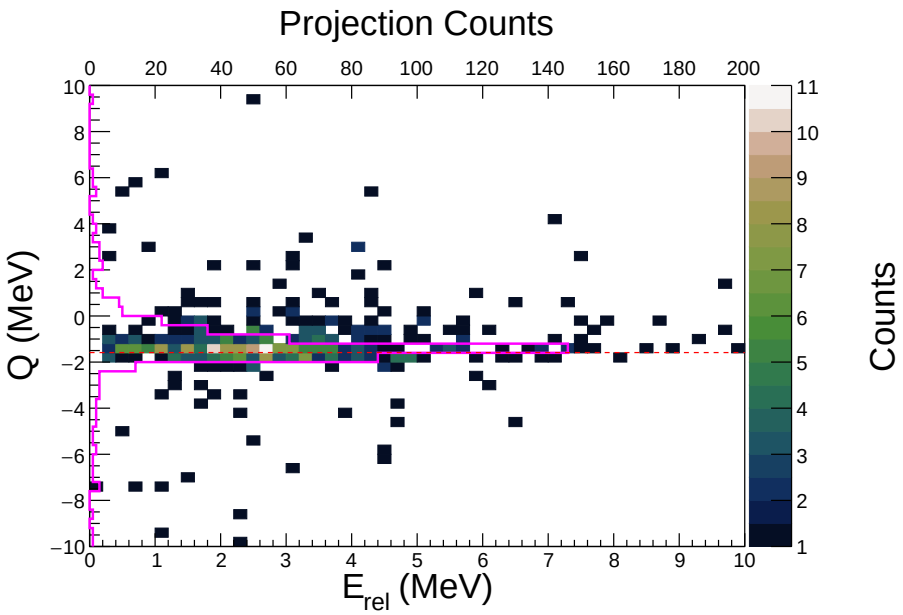

Figure 6.3 Plot of reconstructed Q-value versus relative energy for the α + ^{3}He exit channel. The one-dimensional projection of the Q-value is plotted in magenta along the y-axis. The breakup Q-value, indicated by the red, dashed line, is -1.587 MeV

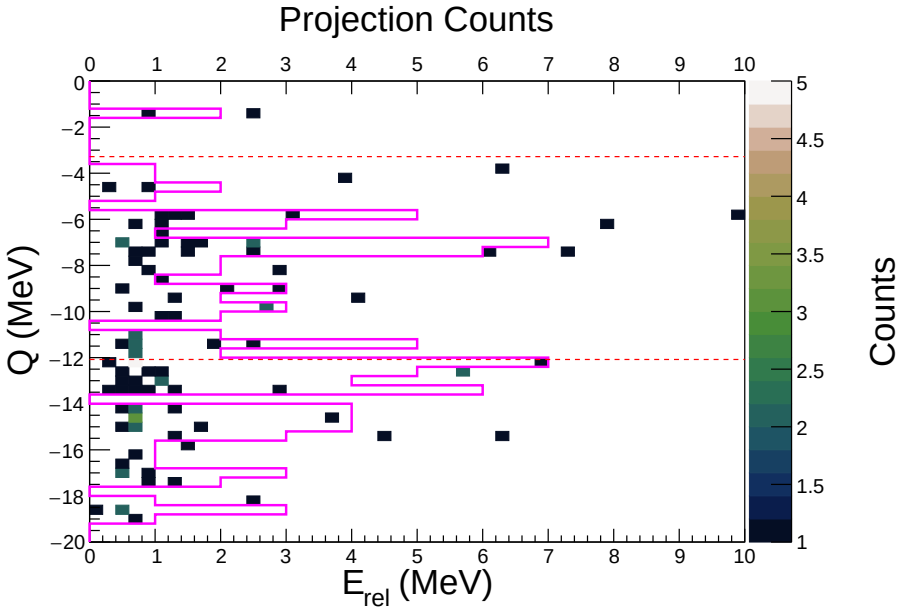

Figure 6.4 Plot of reconstructed Q-value versus relative energy for the $\alpha + d$ exit channel. The one-dimensional projection fo the Q-value is plotted in magenta along the y-axis. The maximum expected Q-value is indicated by the higher of the red, dashed lines. The lower red, dashed line indicates the average expected Q-value, based on the optimum Q-value.

Breakup Mode	Resonance	Width (keV)	On-Resonance Lifetime (s)	Near-Target Breakup?
$^{8}\mathrm{Be} \rightarrow \alpha + \alpha$	0^{+}	5.57	1.2×10^{-16}	No
	2^{+}	1513	4.4×10^{-22}	Yes
$^{7}\mathrm{Be} \rightarrow \alpha + {}^{3}\mathrm{He}$	$7/2^{-}$	175	3.8×10^{-21}	Yes
$^{6}\mathrm{Li} \rightarrow \alpha + d$	3^{+}	24	2.7×10^{-20}	Yes

Table 6.2 Table indicating the resonant breakup channels and their decay widths and lifetimes. Also indicated is whether near-target breakup, leading to potential sequential capture, is dominant in each case based on these lifetimes. Resonance data are from the National Nuclear Data Center evaluations in Refs. [4] and [36].

6.3 Separating Near-Target and Asymptotic Breakup

One step of this analysis is to ensure that breakup is simulated in a realistic manner. To do this, comparisons between *KOOKABURRA* and the measured data allow for validation of the simulated data. In this section, these comparisons will be made in part to demonstrate the validity of the simulation, but also to interpret the reaction dynamics for each process. Before going forward, I emphasize that in the following one dimensional relative energy spectra, the simulation data are scaled down to match the statistics of the experimental data for easier comparison, which is why the error bars are much smaller.

The relative energy spectra (measured in black and simulated with *KOOKABURRA* in red) for transfer-triggered breakup $^{7}\mathrm{Be} + {}^{208}\mathrm{Pb} \rightarrow {}^{8}\mathrm{Be}^{*} + {}^{207}\mathrm{Pb} \rightarrow \alpha + \alpha + {}^{207}\mathrm{Pb}$ are plotted in Fig. 6.2. As discussed in the prior section, the two resonances observed can be separated in relative energy alone, indicated by the dashed line in this projection plot. In one dimension, one can observe the 0^{+} resonance of ^{8}Be, sharply peaked below 500 keV, near where it is expected at 92 keV. Meanwhile, the 2^{+} resonance is broad, spanning higher relative energies, although peaking near 2 MeV. First, note the on-resonance lifetimes of these states, indicated in Table 6.2. The 0^{+} ($\tau = 1.2 \times 10^{-16}$ s) is much more long-lived than the 2^{+} resonance ($\tau = 4.4 \times 10^{-22}$ s) and this makes a significant difference in understanding how the relative energy spectrum reflects the trajectories of the breakup fragments. Because of the timescale for fusion being roughly 10^{-21} s, breakup of the 0^{+} resonance occurs asymptotically far from the target, such that the resulting α-yields will only escape. When trajectories pass closer to the target, they will result in complete fusion. However, the 2^{+} resonance disintegrates fast enough such that trajectories that pass near enough the target

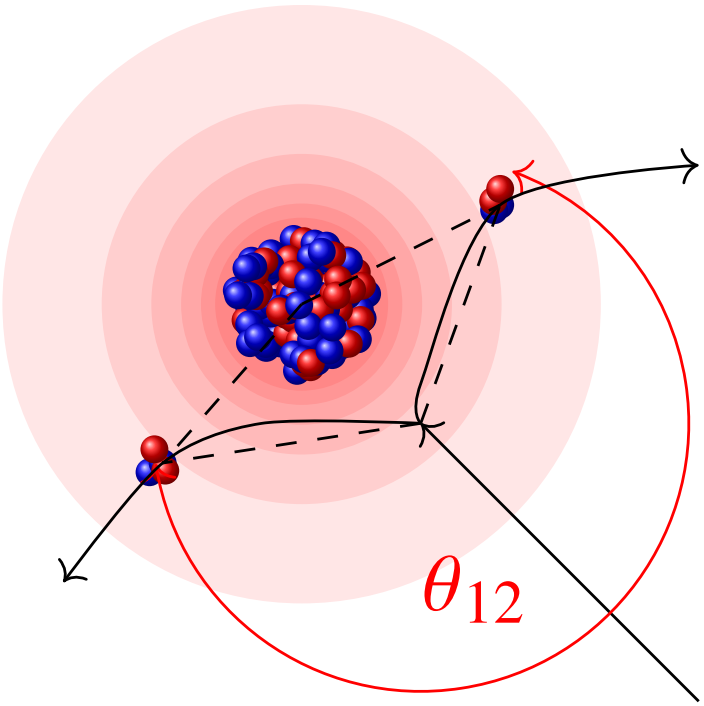

Figure 6.5 Cartoon illustrating the effects Coulomb perturbations in near-target breakup. The incoming projectile decays close to the target. The resulting breakup fragments are subject to accelerations from the target's field, which will in turn affect their outgoing trajectories. This broadens the range of accessible opening angles and relative momenta of the breakup fragments.

can result in incomplete fusion or complete fusion, and that trajectories passing farther from the target could result in fusion or no-capture breakup, since the projectile disintegrates *near* the target, perturbing the paths of the reaction products, unlike breakup via long-lived resonances.

This can also be confirmed in the relative energy spectrum. Without the effects of the target field, one would expect peaks in relative energy to have widths corresponding to the decay width of each resonance – the 0^+ resonance, with a width of 5.57 eV, is narrow, while the 2^+ resonance has a broader width of 1.513 MeV.

When one examines the corresponding relative energy spectrum in Fig. 6.2, one sees that the 0^+ resonance is peaked sharply since the breakup fragments are not subject to the Coulomb accelerations near the target, so one expects the peak width to match the resonance width. In comparison, the 2^+ resonance, which has a shorter lifetime, results in breakup yields near the target, and are therefore subject to such accelerations. This is seen in the smeared relative energy peak for the associated resonance. Rather than the energy peaking at an energy corresponding to the

difference between the resonance energy and the breakup threshold (E_{rel} = 2.9 MeV) with a width of 1.5 MeV, the peak takes a broader distribution in excitation energy than just the decay width of 1.5 MeV. See Fig. 6.5 for a cartoon illustrating the effect of the target field on the trajectories of the outgoing breakup fragments. Note that the smearing of the relative energy peak is expected to be asymmetric. This is because the Coulomb field of the target can accelerate the fragments away from each other *or* towards each other, depending on whether breakup occurs on the incoming or outgoing trajectory. However, because the populated transfer-triggered resonances have some lifetime, for a given resonance, breakup may be more likely to occur on the incoming versus the outgoing trajectory, resulting in target field perturbations to *more often* increase or decrease the relative energy between fragments [34].

Finally, note that in Fig. 6.2, the simulated relative energy spectrum for ^{8}Be breakup (in red) closely matches the measured breakup (in black). This serves as one indicator that the breakup is being accurately simulated for the purposes of efficiency determination, which will be discussed later in Sec. 6.6.

The relative energy spectra for ^{7}Be breakup into α + ^{3}He from the experimental and simulated data are shown in Fig. 6.6. The simulation accurately reproduces the $7/2^{-}$ resonance peak at the expected energy near 3 MeV and we observe the same peak in the measurement. Broad, higher-lying states of ^{7}Be result in a continuum excitation energies, rather than a singular resonant state associated with some single energy level. These couplings are modeled in simulation as non-resonant breakup [18]. For the breakup of ^{7}Be, the non-resonant breakup was determined to make up 61% of the projectile's disintegration [37]. The non-resonant breakup simulation is in good agreement with the measured counts.

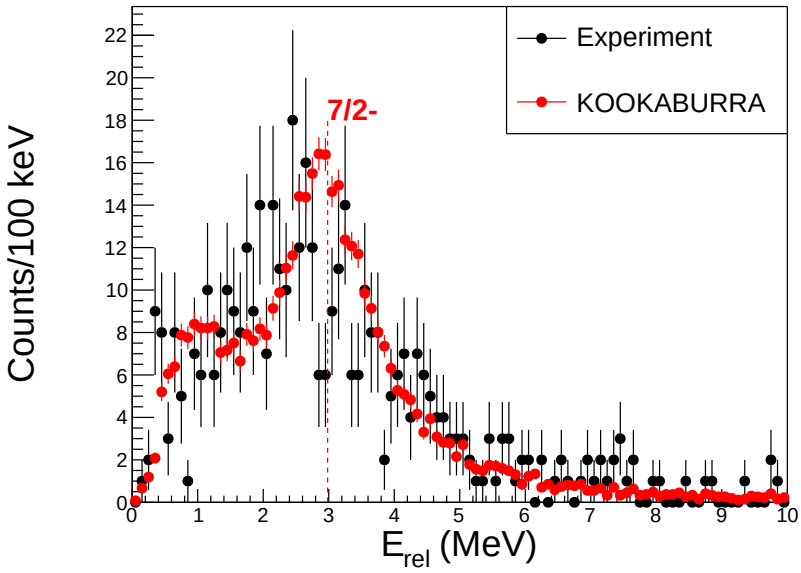

Figure 6.6 Relative energy spectrum for the α + ^{3}He exit channel resulting from breakup of ^{7}Be. The experimental data are plotted in black and the data simulated with *KOOKABURRA* are plotted in red. The red, dashed line indicates the expected energy of the peak associated with the $7/2^{-}$ resonance in ^{7}Be.

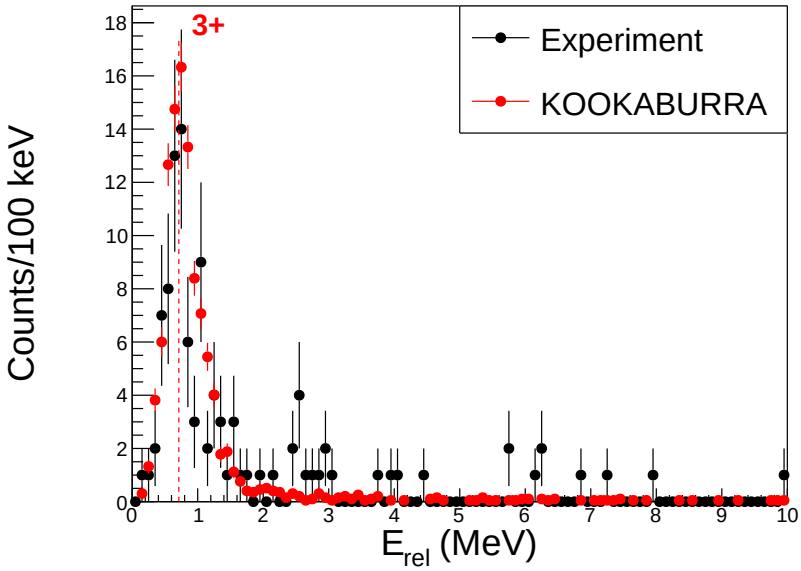

Figure 6.7 Measured (black) and simulated (red) relative energy spectra for the breakup of the $\alpha + d$ exit channel from the proton stripping mode of ^{7}Be + ^{208}Pb. Only breakup through the 3^{+} resonance was simulated, but this matches the measured data well. The red, dashed line indicates the expected location of the resonance peak.

The reconstructed relative energy spectrum for breakup of ^{6}Li, populated via proton-stripping of ^{7}Be, is shown in Fig. 6.7. Again, the measured data are plotted in black and the simulated data are plotted in red. Here, the breakup can be associated with the 3^{+} resonance in ^{6}Li, which decays quickly enough to break up near the target. While the resonance peak is not very broad, it is still smeared broader than the 24 keV decay width of the 3^{+} resonance due to perturbations of the target field on the breakup fragments.

The orientation of the breakup fragments serves as an additional, more sensitive method for separating near-target and asymptotic breakup modes. Recall from Eq. 2.24 that the β angle of the breakup fragments should have a sinusoidal relationship with respect to the opening angle, θ_{12}. This can be observed in asymptotic breakup, where the fragment trajectories are not distorted by interactions with the target field following breakup. In contrast, breakup near the target results in the perturbations of fragment trajectories, such that there is a broader range of opening angles, θ_{12}, possible [18].

Figure 6.8 shows the measured orientation spectrum for the breakup of ^{8}Be into two α-particles. There is clear separation between the band at small θ_{12}, corresponding to the asymptotic breakup from the 0^{+} resonance, and the near-target breakup from the 2^{+} resonance, which accesses a broader distribution of θ_{12} and β angles due to accelerations from the target's Coulomb field [26]. The simulation of breakup aids this interpretation. See the simulated breakup orientation for the $\alpha + \alpha$ exit channel in Fig. 6.9, where each simulated resonance is identified and plotted in separate panels. The asymptotic breakup resulting from the decay of the 0^{+} resonance is restricted to more closed opening angles when compared to that of the 2^{+} resonance.

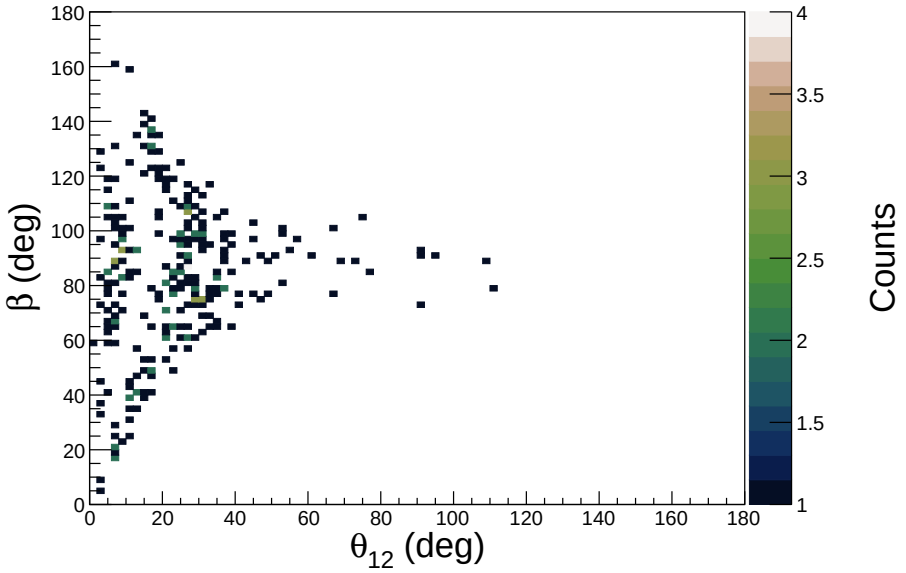

Figure 6.8 Orientation matrix, plotting the opening angle between breakup fragments, θ_{12}, against their angle of relative momentum, β for the transfer-triggered breakup mode $^{7}\mathrm{Be} + n \rightarrow {}^{8}\mathrm{Be}^{*} \rightarrow \alpha{+}\alpha$. There are two separate bands from which near-target and asymptotic breakup can be separated based on the populated resonances, as discussed in the text.

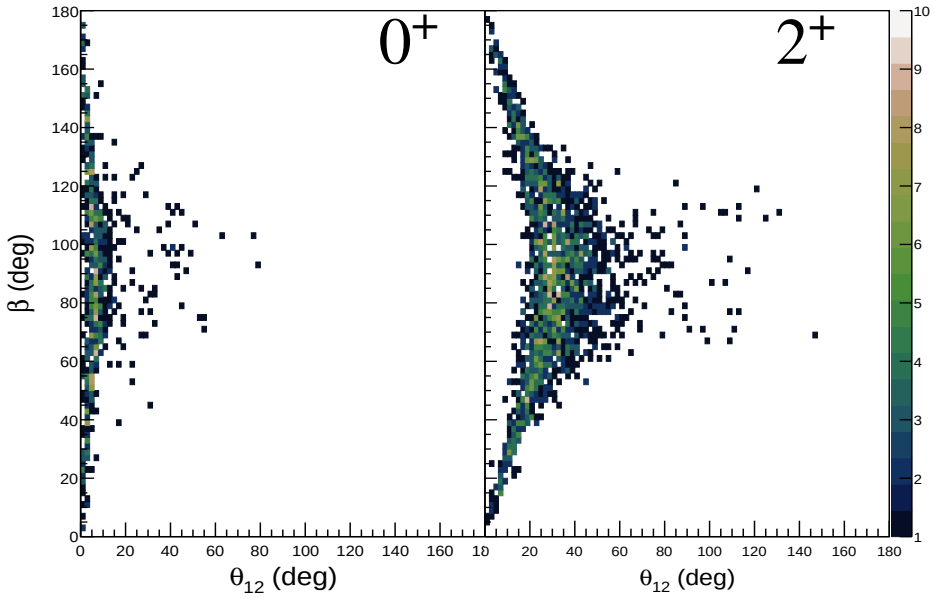

Figure 6.9 Simulated orientation matrix for the decay of ^{8}Be into the $\alpha + \alpha$ exit channel. The two simulated resonances of ^{8}Be prior to breakup were the 0^{+} (plotted on the left panel) and 2^{+} (plotted on the right panel) states. Based on the lifetime of each resonance, the effects of the target's Coulomb field can be observed in the orientations of the resulting breakup fragments, as discussed in the text.

The breakup orientation matrix for the direct breakup of ^{7}Be is shown in Fig. 6.10. There again is a band of resonant breakup, which can be attributed to decay from the $7/2^{-}$ resonance in ^{7}Be, but non-resonant breakup can also be observed at broader opening angles. In Fig. 6.11, the simulated orientation matrix for both the resonant and non-resonant breakup are plotted in separate panels. One discrepancy worthy of note here is that while the simulated breakup orientation is slightly more intense at higher β than lower, the measured orientation matrix in Fig. 6.10 is far less symmetric. Asymmetry in the breakup orientation matrix is expected when the resulting fragments are not the same mass, but the difference in asymmetry may signal that the breakup simulations do not represent the measured data as accurately as the relative energy agreement shown in Fig. 6.6 would suggest. However, this discrepancy may only be due to a lack of statistics, since one can make the shape out of the lower β band, but with very few counts. The simulation breakup also shows that the resonant breakup has more asymptotic breakup (smaller θ_{12}) than the non-resonant breakup, which has breakup events with much larger opening angles.

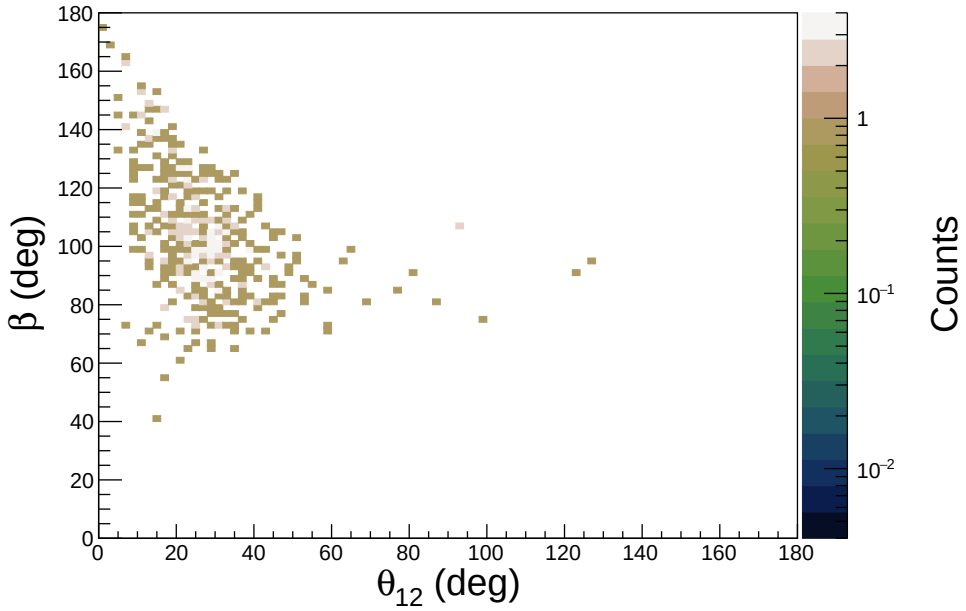

Figure 6.10 Orientation matrix, plotting the measured opening angle between breakup fragments, θ_{12}, against their angle of relative momentum, β for the direct breakup mode $^{7}\text{Be} \rightarrow \alpha + {}^{3}\text{He}$. Present are contributions from near-target, resonant $7/2^{-}$ breakup and non-resonant breakup.

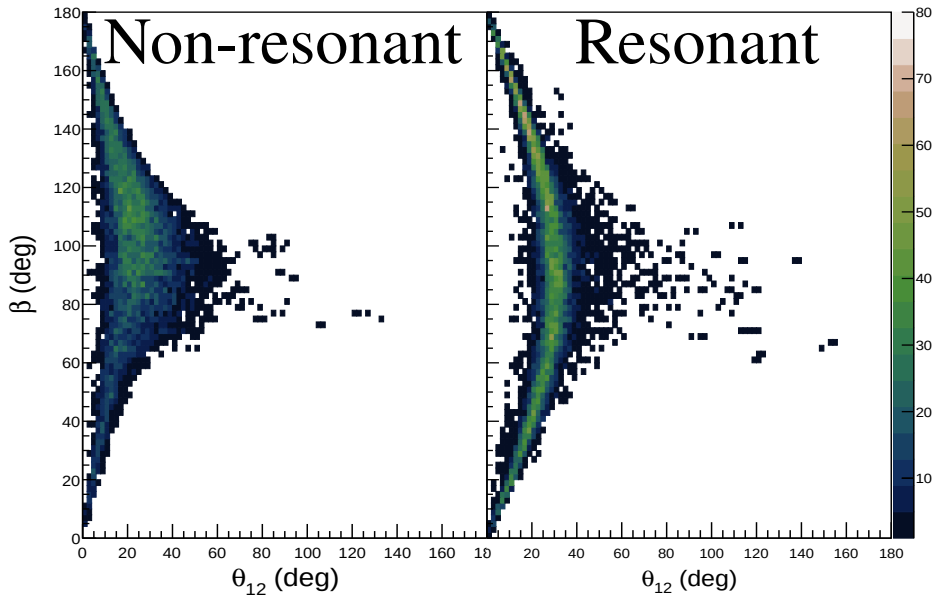

Figure 6.11 Simulated orientation matrix for the breakup of ^{7}Be into the $\alpha + {}^{3}$He exit channel. The resonant (right) and non-resonant (left) breakup are plotted separately in each panel. While both appear to have near-target and resonant breakup, more of the non-resonant breakup seems to occur near-target than in the case of the resonant breakup.

Finally, by inspecting the orientation spectrum for breakup of ^{6}Li, shown in Fig. 6.12, there is only evidence of a single resonance being populated prior to breakup. Comparing to the simulated orientation matrix for $\alpha + d$, shown in Fig. 6.13, which is simulated with only the inclusion of breakup through the 3^{+} resonance, the breakup orientation distribution is reasonably reproduced. This aids in the interpretation of the relative energy spectrum in Fig. 6.7. While there is a discrepancy between experiment and simulated data near 2-3 MeV, where one could maybe identify a small peak in the relative energy spectrum, the breakup orientation matrix provides evidence that there is only one resonance present in this breakup mode.

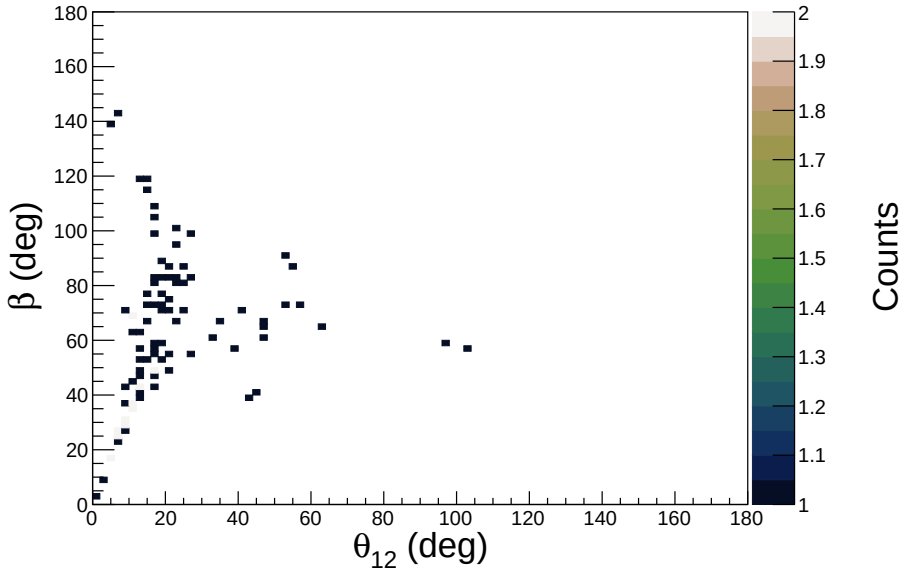

Figure 6.12 Orientation matrix, plotting the **measured** opening angle between breakup fragments, θ_{12}, against their angle of relative momentum, β for the transfer-triggered breakup mode $^{7}\mathrm{Be} - p \rightarrow {}^{6}\mathrm{Li}^{*} \rightarrow \alpha + d$. There is only one band of near-target breakup present, attributed to the population of the 3^{+} resonance in ^{6}Li.

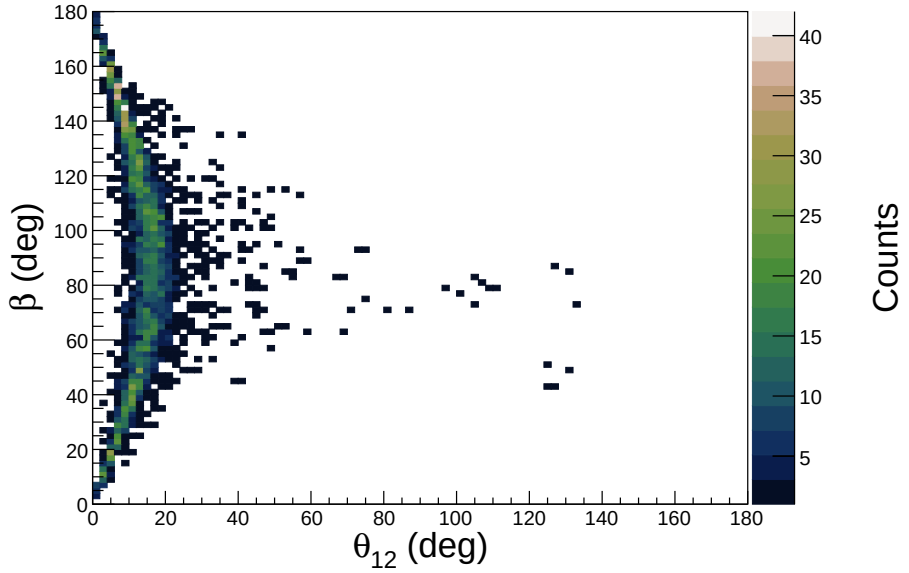

Figure 6.13 Orientation matrix, plotting the **simulated** opening angle between breakup fragments, θ_{12}, against their angle of relative momentum, β for the transfer-triggered breakup mode $^{7}\mathrm{Be} - p \rightarrow {}^{6}\mathrm{Li}^{*} \rightarrow \alpha + d$. Only breakup via the 3^{+} resonance were simulated here. Based on the agreement between this spectrum and the reconstructed experimental spectrum, the presence of breakup primarily through the 3^{+} resonance can be confirmed.

6.4 Efficiency Corrections and Normalization

After raw coincidence yields have been determined, one must account for the efficiencies within the detector array, as well as a normalization of the overall cross sections based on the measured Rutherford scattering. In this section, each of these processes will be discussed.

A consequence of the beam offset determination, discussed in Ch. 5, is that there are distortions in the calculated solid angle of the detector edges based off of the adjusted detector positioning, as slight offset adjustments will have a disproportionately large impact on the detector edges compared to the middle of the detectors. As a result, in this chapter and in Ch. 7, where cross sections are presented, points associated with the first and last arc and sector of each detector have been discarded.

6.4.1 $\Delta E - E$ Pairing Correction

The data in this experiment suffers from "pairing" inefficiencies – the ability to appropriately match virtual pixels in the ΔE and E_{res} detectors, required for particle identification – due to a combination of the beam offset, mechanical detector mounts, and virtual pixel sizes. While the procedure for pixelization, described in Ch. 4 minimizes these effects, they are not completely eliminated. For this reason, a subtle pairing efficiency correction has been applied to all yields to mitigate this issue. The pairing efficiency was determined by comparing the yield of $\Delta E - E$ paired elastic scattering events to that of the total elastic events, determined by gating on the elastic band in a $\Delta E - \theta$ matrix. This allows the elastic events to be easily identifiable without $\Delta E - E$ identification as long as they were measured in the ΔE detector, since the kinematic line of elastic scattering appears very differently from that of breakup fragments. This is also shown in the full particle energy versus scattering angle plot in Fig. 4.14.

The resulting efficiency determination is shown in Fig. 6.14. These factors are then used to scale the yields accordingly along the scattering angle up to 140°, at which point, the scattering data was too sparse at backwards angles for a reasonable determination, so no pairing correction was applied.

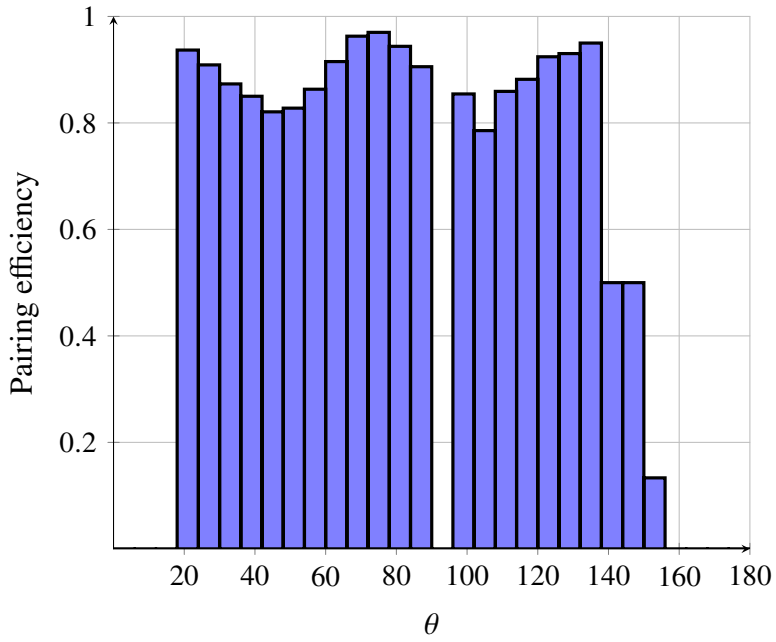

Figure 6.14 Pairing efficiency as a function of scattering angle. The correction factor implemented on the yields to correct for inefficiencies in pairing between ΔE and E_{res} detectors is the inverse of the pairing efficiency. The method for determining the correction factors is described in the text.

6.4.2 Rutherford Normalization

The cross sections for breakup and fusion measured in FABLE are normalized against a simultaneous Rutherford scattering measurement at forward angles in the beam monitor detectors, where the measured elastic scattering is well approximated by Rutherford scattering. This approach means that systematic uncertainties associated with the beam current, target thickness, and solid angle can be canceled out. Therefore, I will now go over the process for Rutherford normalization. Recall that we can express the yield, Y, measured in some solid angle $d\Omega$, for a given reaction as a function of its differential cross section, $d\sigma/d\Omega$, by

$$Y(\theta) = \int_{\Omega} IN \frac{d\sigma(\theta)}{d\Omega} d\Omega \times \epsilon, \tag{6.1}$$

where I is the beam current, N is the target number density, ϵ is the efficiency of the measurement, and $d\Omega$ is the differential solid angle subtended at a given angle, θ. In cases where the total solid angle of the measurement, $\Delta\Omega$ is small, the integral can be approximated as a multiplicative factor of $\Delta\Omega$:

$$Y(\theta) = IN \frac{d\sigma(\theta)}{d\Omega} \Delta\Omega \times \epsilon. \tag{6.2}$$

We can write this expression for breakup in FABLE as

$$Y_{\mathrm{BU}}(\theta) = IN\frac{d\sigma_{\mathrm{BU}}(\theta)}{d\Omega}\Delta\Omega_{\mathrm{FABLE}} \times \epsilon_{\mathrm{coin}}, \tag{6.3}$$

where $\Delta\Omega_{\mathrm{FABLE}}$ is the solid angle of FABLE and ϵ_{coin} refers to the coincidence efficiency of the measurement. The yield for Rutherford scattering in the monitor detectors can also be expressed as

$$Y_{\mathrm{Ruth}}(\theta) = IN\frac{d\sigma_{\mathrm{Ruth}}(\theta)}{d\Omega}\Delta\Omega_{M} \times \epsilon_{M}, \tag{6.4}$$

where ϵ_M is the efficiency of the monitor detector and $\Delta\Omega_M$ is the solid angle of the detector. We can then take the ratio of the two expressions to express the differential cross-sections as a function of the solid angles and yields while removing systematic dependencies on the beam current and target thickness:

$$\frac{Y_{\mathrm{BU}}(\theta)}{Y_{\mathrm{Ruth}}(\theta')} = \frac{\frac{d\sigma_{\mathrm{BU}}(\theta)}{d\Omega}}{\frac{d\sigma_{\mathrm{Ruth}}(\theta')}{d\Omega'}}\frac{\Delta\Omega}{\Delta\Omega'}\frac{\epsilon_{\mathrm{coin}}}{\epsilon_M}. \tag{6.5}$$

Using this, reaction probabilities can be normalized based on Rutherford scattering measured in the beam monitors at forward angles. We then must determine the ratio of solid angles, $\Delta\Omega_{\mathrm{FABLE}}/\Delta\Omega_M$. The yield in these monitors $Y_{\mathrm{Ruth}}(\theta = \theta_M)$ can be expressed as

$$Y_{\mathrm{Ruth}}(\theta_M) = IN\frac{d\sigma_{\mathrm{Ruth}}(\theta = \theta_M)}{d\Omega_M}\Delta\Omega_{M} \times \epsilon_{M}, \tag{6.6}$$

where θ_M is the scattering angle position of the monitor and $\Delta\Omega_M$ is its solid angle. Recall that the elastic scattering of ^{14}N was measured in the alternative "lampshade" configuration (see Ch. 3). The beam energy, at 56 MeV, was sufficiently low such that scattering at even backwards angles would be Coulomb-dominated. Therefore, the ^{14}N Rutherford scattering data were also used to determine the solid angle, $\Delta\Omega_M$, of the beam monitor detectors.

In this reaction, the Rutherford yield measured in FABLE is

$$Y_{\mathrm{Ruth}}(\theta_{\mathrm{FABLE}}) = IN\frac{d\sigma_{\mathrm{Ruth}}(\theta_{\mathrm{FABLE}})}{d\Omega_{\mathrm{FABLE}}}\Delta\Omega_{\mathrm{FABLE}} \times \epsilon_{\mathrm{FABLE}}, \tag{6.7}$$

where $\epsilon_{\mathrm{FABLE}}$ is the singles efficiency of FABLE. By taking the ratio of Eqs. 6.6 and 6.7, the dependence on the beam current and target thickness are canceled out. Rearranging this ratio, the

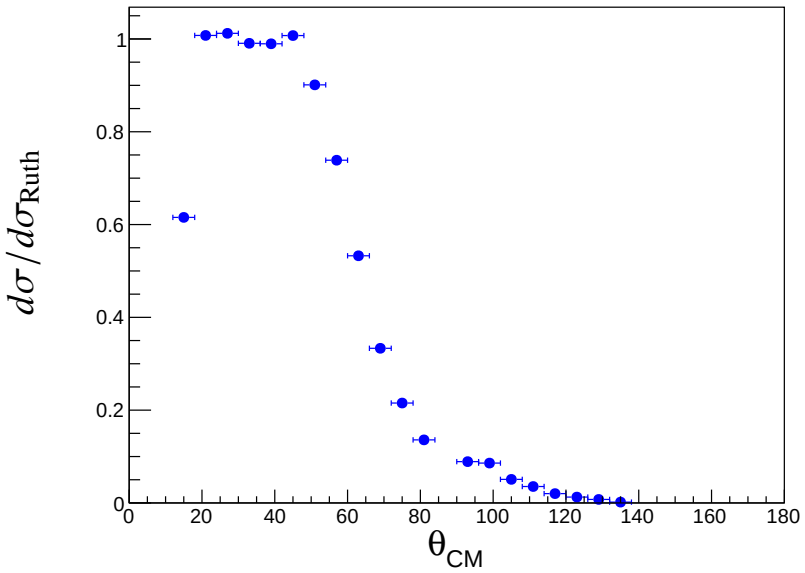

Figure 6.15 Ratio of the differential cross sections for elastic scattering with respect to the Rutherford cross section for ^{7}Be on ^{208}Pb at E_{lab} = 51.74 MeV after accounting for energy loss in the target. The first point near 18° was not included in the pinning of the normalization.

solid angle of the beam monitor detector, $\Delta\Omega_M$ is found in terms of the ^{14}N scattering measurement:

$$\Delta\Omega_M = \Delta\Omega_{\text{FABLE}} \frac{Y_{\text{Ruth}}(\theta_M)}{Y_{\text{Ruth}}(\theta_{\text{FABLE}})} \frac{\frac{d\sigma_{\text{Ruth}}(\theta_{\text{FABLE}})}{d\Omega_{\text{FABLE}}}}{\frac{d\sigma_{\text{Ruth}}(\theta_M)}{d\Omega_M}} \frac{\epsilon_{\text{FABLE}}}{\epsilon_M}. \tag{6.8}$$

This expression can then be used to plug the solid angle, $\Delta\Omega_M$, into Eq. 6.5 for normalizing breakup yields to ultimately extract cross sections, giving

$$\frac{d\sigma_{\text{BU}}(\theta)}{d\Omega} = \frac{Y_{\text{BU}}(\theta)\Delta\Omega_M}{Y_{\text{Ruth}}(\theta_M)\Delta\Omega_{\text{FABLE}}} \times \epsilon_{\text{coin}}(\theta, \varphi), \tag{6.9}$$

where the yields are associated with the ^{7}Be measurement here.

The Rutherford normalization can be verified by inspecting the measured elastic scattering-to-Rutherford ratio differential cross section, which is shown in Fig. 6.15. While the cross section was self-normalized based on the forward-angled measured points by a scaling factor of 0.94, the lack of significant changes in the cross section between 20-40 degrees suggest that the normalization using these points as an anchor is valid.

6.4.3 Coincidence Efficiency Correction

KOOKABURRA was used to simulate 10^8 non-elastic events to determine how likely it was that one may measure a breakup fragment in (θ_1, φ_1), given that another fragment was measured in (θ_2, φ_2) following projectile disintegration. To illustrate this idea, see Fig. 6.16, which shows FABLE's acceptance in $\theta - \varphi$ space and a cyan star to indicate the measurement of a breakup fragment in one of the telescopes. The ellipse corresponds to the possible locations of breakup fragments for a constant opening angle θ_{12}. Since the simulation gives breakup fragment locations and energies, and they can be filtered through FABLE's geometric and acceptance, following the description of FABLE's geometry and coordinate system in Sec. 4.1, as well as FABLE's energy thresholds. Then, the breakup simulation and filtering routine together can be used to determine coincidence breakup efficiencies for each breakup channel. In addition, the particle locations and energies were used to generate spectra of breakup fragment relative energies and orientations, which were compared to the experimental spectra. Since the simulation data can be gated on individual breakup channels and resonances, this aided in the interpretation of the measured data, as discussed in earlier sections of this chapter.

Recall that the pseudoprojectile, or the trajectory of the projectile prior to breakup, can be reconstructed from the resulting fragments' positions and energies (see Sec. 2.5 for the full description). Therefore, it is more convenient to apply a coincidence efficiency correction for the exclusive breakup measurement with respect to the pseudoprojectile's scattering angle, θ_p, and the opening angle between fragments, θ_{12}, rather than expressing the coincidence efficiency as a function of $(\theta_1, \varphi_1, \theta_2, \varphi_2)$. However, using only (θ_{12}, θ_p) completely determines the positions of both breakup fragments, so this was how the efficiency spectra were applied. In this analysis, the efficiency correction was applied with 6° bin widths as appropriate for the statistics of the experimental data. The yields, after correcting for coincidence efficiencies, are shown for each exit channel: Figure 6.17 plots the $\alpha + \alpha$ exit channel, Fig. 6.18 plots the $\alpha + {}^3\mathrm{He}$ exit channel, and Fig. 6.19 shows the $\alpha + d$ exit channel.

After determining coincidence efficiency-corrected yields for no-capture breakup, the yields

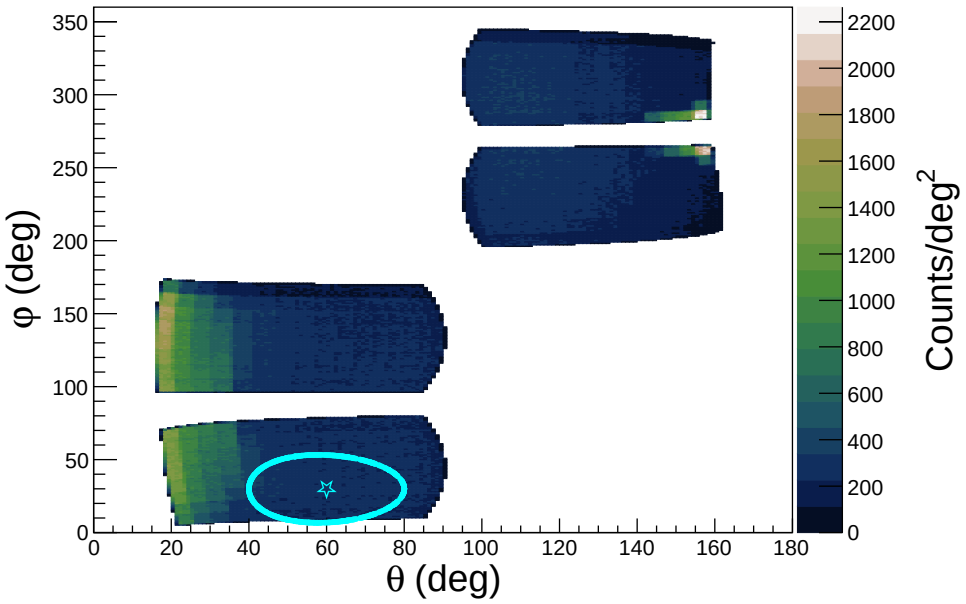

Figure 6.16 Matrix of φ versus θ for charged particles measured in FABLE to illustrate the goal of coincidence efficiency determination. If a breakup fragment is measured in the detector at the cyan star, any breakup fragment that lands in the detector's coverage that intersects with the cyan line indicates a breakup event in which FABLE is sensitive to both particles to be measured in coincidence for breakup occurring at an opening angle of $\theta_{12} = 20°$. The simulated breakup can then be used to extract a coincidence efficiency based off this method.

associated with breakup for each particle must also be efficiency-corrected for the determination of unaccompanied cross sections. This correction was applied as a function of the charged particle's scattering angle θ and its energy E.

6.5 No-Capture Breakup Cross Sections

Once the coincidence yields for each exit channel have been extracted and the normalization has been established, the no-capture breakup cross sections can be determined for each breakup mode. The no-capture breakup differential cross sections with respect to the pseudoangle of the projectile prior to breakup for the $\alpha+\alpha$ exit channel through each resonance are shown in Fig. 6.20. The no-capture breakup cross sections for the direct breakup into $\alpha + {}^3$He are shown in Fig. 6.21 and for the $\alpha + d$ channel are shown in Fig. 6.22. Note that they all peak near $\theta_p \approx 60°$, near the grazing angle. These differential cross sections will be used in combination with the singles cross sections to extract unaccompanied α and ^{3}He cross sections in the following Ch. 7. The integrated

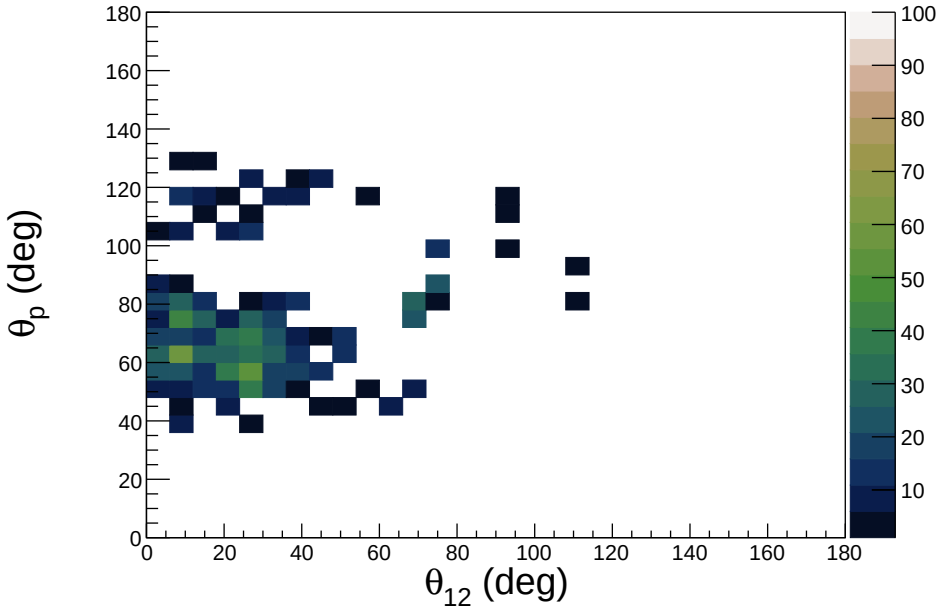

Figure 6.17 Efficiency-corrected matrix for pseudoangle of the projectile prior to breakup versus opening angle between breakup fragments in the $\alpha + \alpha$ exit channel.

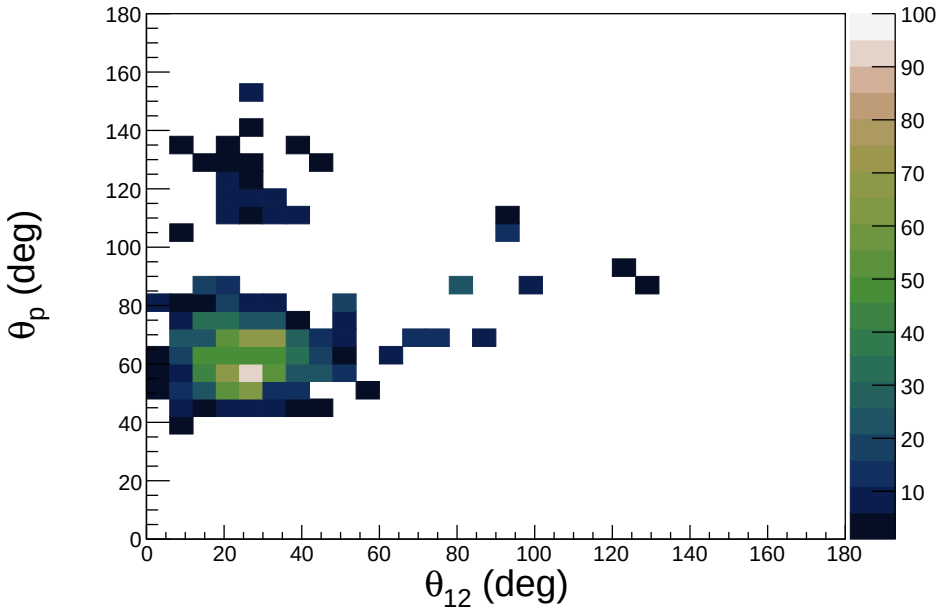

Figure 6.18 Efficiency-corrected matrix for pseudoangle of the projectile prior to breakup versus opening angle between breakup fragments in the $\alpha + {}^{3}\mathrm{He}$ exit channel. The color scale shows the counts per bin.

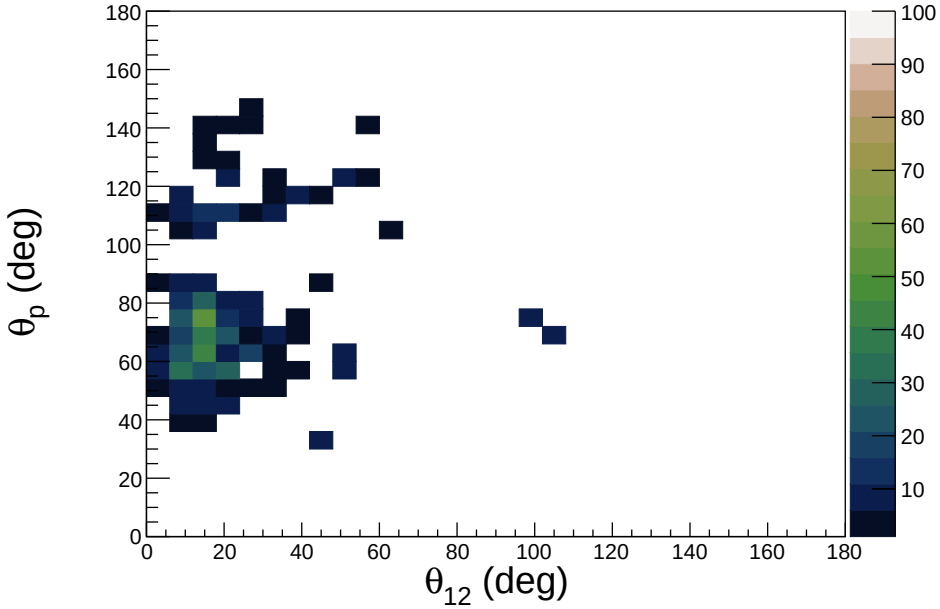

Figure 6.19 Efficiency-corrected matrix for pseudoangle of the projectile prior to breakup versus opening angle between breakup fragments in the $\alpha + d$ exit channel. The color scale shows the counts per bin.

Exit Channel	σ (mb)
$^{7}\mathrm{Be} \rightarrow \alpha + {}^{3}\mathrm{He}$	7.9 ± 2
$^{6}\mathrm{Li}^{*} \rightarrow \alpha + d$	3.2 ± 0.6
$^{8}\mathrm{Be}^{*} \rightarrow \alpha + \alpha$	4.5 ± 1
$^{8}\mathrm{Be}^{0^{+}} \rightarrow \alpha + \alpha$	1.1 ± 0.4
$^{8}\mathrm{Be}^{2^{+}} \rightarrow \alpha + \alpha$	3.3 ± 0.8

Table 6.3 Integrated no-capture breakup cross sections for ^{7}Be + ^{208}Pb at $E_{\mathrm{CM}} = 50.05$ MeV, measured in this work. The contributions for the separable resonances in ^{8}Be have also been indicated.

cross sections for each exit channel are indicated in Table 6.3.

6.6 Simulation Validity

Breakup simulations, based off the breakup cross sections, were calculated using *KOOK-ABURRA*, a semi-classical three-body dynamics code [26]. For each breakup channel, one specifies a breakup function, $P(R_{\mathrm{min}}) = \exp(\mu R_{\mathrm{min}} + \nu)$, which gives the probability for disintegration as a function of the distance of closest approach. Alongside this function, the lifetimes and excited states for each product must be given. The code then outputs the outgoing trajectories for the incident

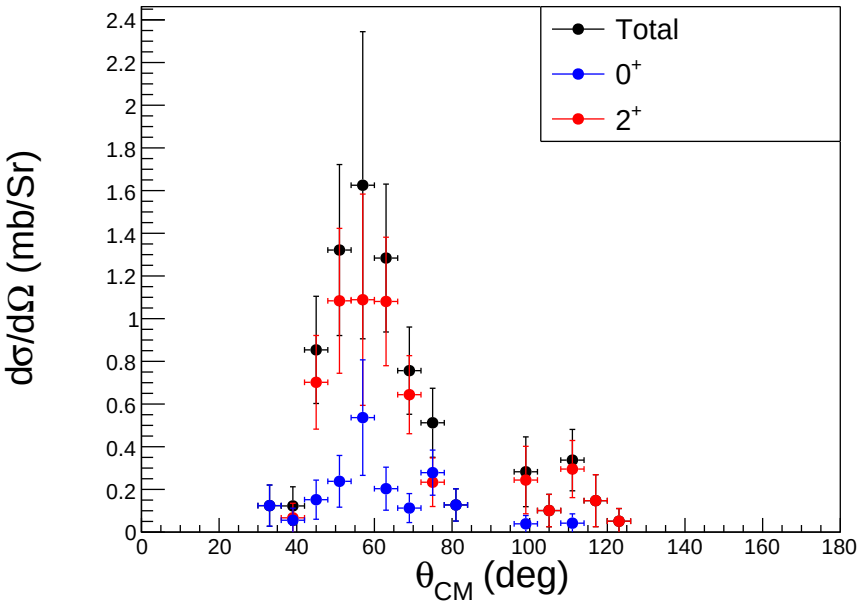

Figure 6.20 Differential cross section for the transfer-triggered no-capture breakup of ^{8}Be in the 0^{+} resonance (red) and the 2^{+} resonance (blue) decaying into two α-particles. The total no-capture breakup differential cross section for $^{8}\mathrm{Be} \rightarrow \alpha + \alpha$ is plotted in black.

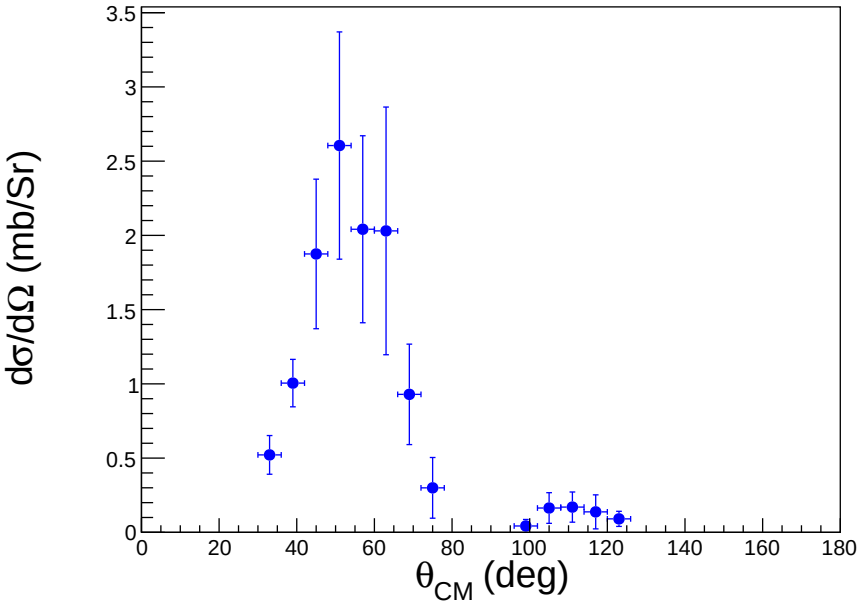

Figure 6.21 Differential cross section for the direct no-capture breakup of ^{7}Be into an α and ^{3}He.

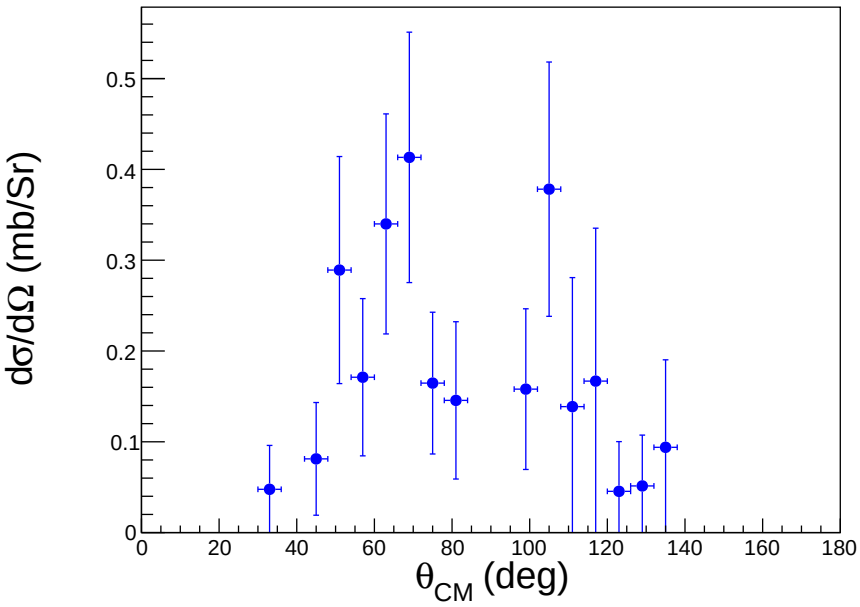

Figure 6.22 Differential cross section for the transfer-triggered no-capture breakup of ^{6}Li in the 3^{+} resonance decaying into an α and a deuteron.

particle, simulates transfer (if probing a transfer-triggered breakup channel), then calculates the trajectories of resulting breakup fragments following stochastic breakup based on the projectile's excitation energy-dependent mean lifetime for the projectile. The breakup fragment locations are then geometrically filtered through FABLE's acceptance using the same pixelization requirements. Through this process, one can calculate both the relevant kinematic spectra for interpretation of breakup modes, as well as the coincidence efficiency for each mode simulated.

Throughout this chapter, there have been several comparisons between measured and simulated breakup with *KOOKABURRA*. In addition, simulations were employed for determination of efficiency corrections. Therefore, it is worth establishing that the breakup simulations are sound for these purposes beyond a simple comparison between the observable quantities (such as relative energy and breakup orientation spectra).

Since this work focuses on reactions of ^{7}Be and ^{208}Pb at energies *above* the fusion barrier, *most* non-elastic processes simulated by *KOOKABURRA* result in complete or incomplete fusion. As a result, using such calculations to determine a coincidence efficiency of the measurement of

no-capture breakup yields proves difficult to gain sufficient statistics. Therefore, calculations were performed with the effects of absorption *ignored* to determine the coincidence efficiency of FABLE with reasonable statistics. This is valid in the determination of the coincidence efficiency since ϵ_{coin} is predominantly geometric. Recall that one of the core inputs for the model calculations is the breakup function for each mode. The breakup function was to be determined from the experimental data, albeit with limited sensitivity to the input breakup function via the coincidence efficiency determination. By iteratively comparing fitted breakup functions to the original input breakup functions, one can converge upon μ and ν exponential fit parameters which result in the simulation of realistic breakup events. The breakup functions, along with their exponential fits, are shown for the $\alpha + \alpha$ resonant breakup modes in Fig. 6.23, for the $\alpha + {}^{3}\text{He}$ exit channel in Fig. 6.24, and for the $\alpha + d$ exit channel in Fig. 6.25.

The fits used do not all span the full domain of distances of closest approach measured in this work to avoid effects of absorption, more common along smaller R_{min} trajectories, which can be observed in the significantly reduced the probabilities of breakup at smaller $R_{\text{min}} < 13$ fm. The breakup function fits are listed in Table 6.4. Because these smaller R_{min} points were discarded, the small amount of remaining points and limited statistics mean that the breakup function heights (ν) are not well constrained. However, the breakup function slopes (μ) could be constrained more reasonably and do converge between the input and output of iterative simulations. Note that the parameter uncertainties represent 1σ errors in the exponential fit, but they do not account for covariances between the correlated μ and ν parameters. To confirm that the efficiency matrices were not sensitive to the breakup function parameters, additional simulations were performed at the extrema of the fits based on these 1σ uncertainties, and efficiency matrices were shown to be unchanged. This demonstrates that the coincidence efficiency determination is not overly-sensitive to the model inputs. These breakup functions, along with excitation energy spectra from the measured data, and potential interactions calculated by SPP2 [20], were the model inputs for the simulations, as described in Ch.2 and allowed for an accurate determination of the efficiency for measurement of no-capture breakup fragments in FABLE.

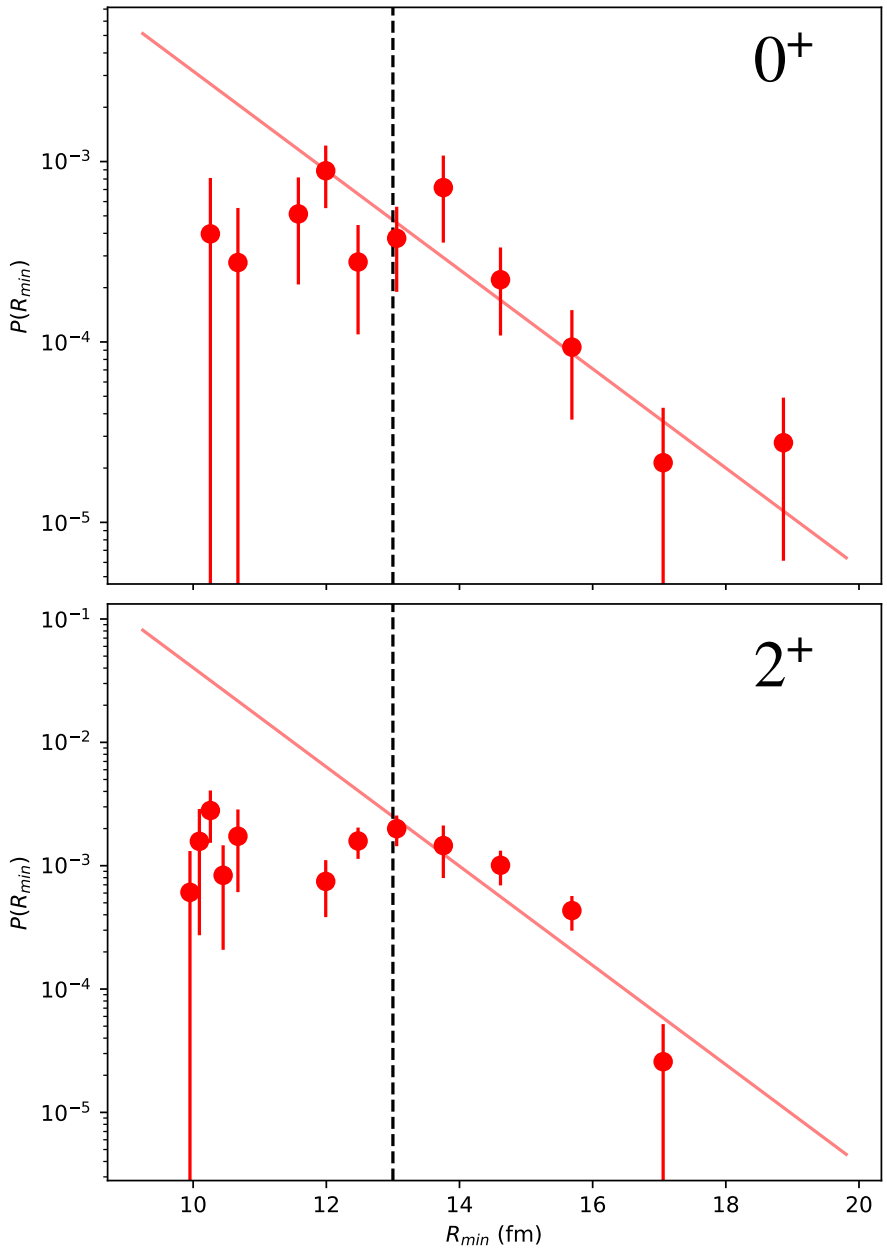

Figure 6.23 Breakup function, plotting the probability for breakup as a function of the distance of closest approach, R_{min}, for the transfer-triggered breakup of ^{7}Be + ^{208}Pb $\rightarrow \alpha + \alpha + ^{207}$Pb for the 0^+ resonance (upper panel) and 2^+ resonance (lower panel). The lines indicates exponential fits for $R_{\text{min}} > 13$ fm (cutoff indicated by the dashed, vertical line). Points below 13 fm are affected by absorption of the breakup fragments and were excluded from the fit for extracting breakup functions.

Breakup Mode	Resonance	μ	ν
$^8\text{Be} \rightarrow \alpha + \alpha$	0^+	0.6 ± 0.1	0.6 ± 2
	2^+	0.9 ± 0.2	6 ± 3
$^7\text{Be} \rightarrow \alpha + ^3\text{He}$	$7/2^-$	0.8 ± 0.2	2.6 ± 3
	Non-resonant	0.8 ± 0.2	2.6 ± 3
$^6\text{Li} \rightarrow \alpha + d$	3^+	0.62 ± 0.04	2.8 ± 0.6

Table 6.4 Breakup functions for each channel simulated in *KOOKABURRA* for analysis of breakup of ^{7}Be. The breakup function is parameterized by μ and ν in the form $P(r) = \exp(-\mu r + \nu)$. The uncertainties represent 1σ error in the fit parameters, but because μ and ν are correlated parameters, these uncertainties do not reflect the overall covariance in the fit of the breakup functions.

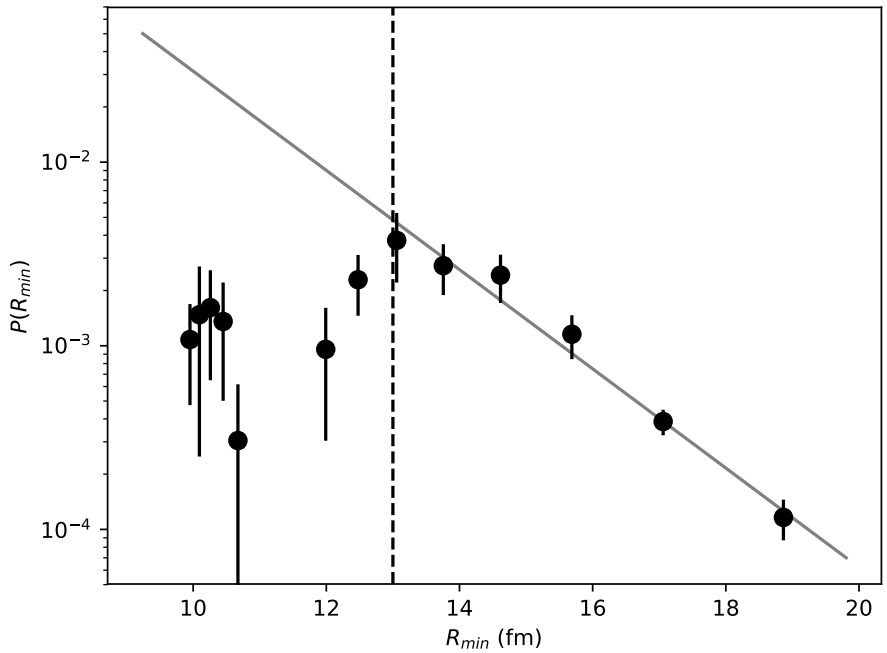

Figure 6.24 Breakup function, plotting the probability for breakup as a function of the distance of closest approach, R_{min}, for the direct breakup of $^7\text{Be} + ^{208}\text{Pb} \rightarrow \alpha + ^3\text{He} + ^{208}\text{Pb}$. The line indicates an exponential fit based on points with greater than $R_{\text{min}} = 13$ fm (dashed, vertical line). Points below this are affected by absorption of the breakup fragments and were excluded from the fit for extracting the breakup function.

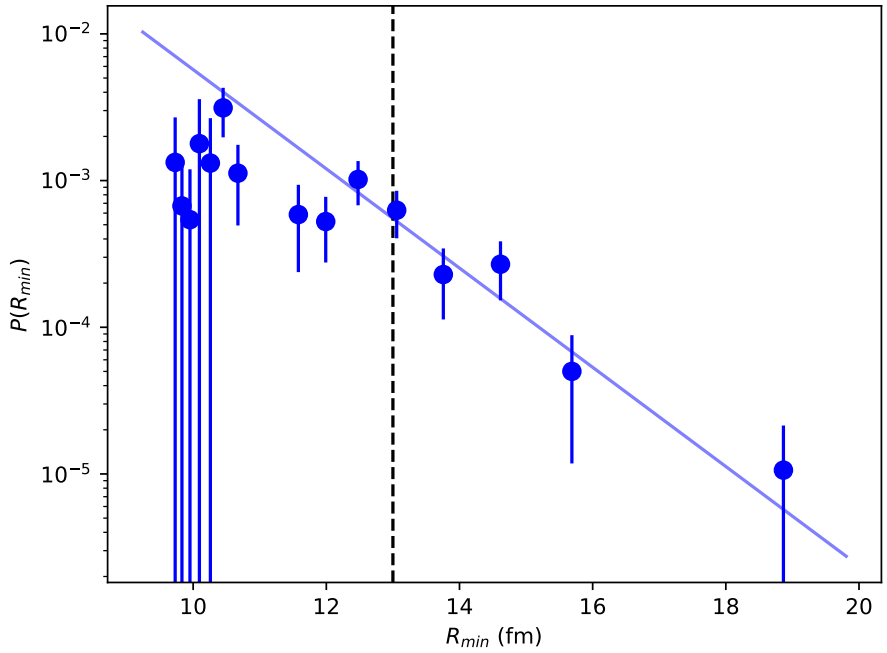

Figure 6.25 Breakup function, plotting the probability for breakup as a function of the distance of closest approach, R_{min}, for the transfer-triggered breakup of ^{7}Be + ^{208}Pb $\rightarrow$ α + d + ^{209}Bi. The solid line indicates an exponential fit and points below 13 fm (indcated by the dashed, vertical line) were excluded.

6.7 Conclusion

In this chapter, the methods by which one can identify different breakup channels and correct the efficiencies of particle measurements in FABLE were discussed. By employing semi-classical simulations, one can better interpret the resulting kinematic spectra for accurate separation of near-target and asymptotic breakup and determine coincidence efficiencies for application to yields to extract exclusive no-capture breakup cross sections. In the next chapter, I will show how these yields, along with the singles yields for ^{3,4}He can be used to extract incomplete fusion cross sections.

CHAPTER 7

BREAKUP AND UNACCOMPANIED CROSS SECTIONS

In the last chapter, the process of extracting yields for no-capture breakup and resulting differential cross sections in the coincidence analysis was demonstrated. In this chapter, by taking the difference in cross sections between the singles yield and the no-capture breakup yield and accounting for α-particle evaporation, unaccompanied α-particle and ^{3}He cross sections will be determined, corresponding to incomplete fusion cross sections resulting in the emission of each helium isotope.

7.1 Singles Cross Sections

The singles cross sections for α and ^{3}He are determined by first selecting each particle with $\Delta E - E$ particle identification and making cuts in $Q - E_{\text{rel}}$ and $E - \theta$ to remove contributions from light impurities, giving a yield distribution measured in FABLE as a function of the scattering angle in the laboratory frame, $Y_{\text{FABLE}}(\theta)$. As discussed in Ch. 6 for coincidence cross sections, this yield can be used to determine a differential cross section in combination with the Rutherford scattering measurement in the beam monitors by

$$\frac{d\sigma_{\text{FABLE}}(\theta)}{d\Omega} = \frac{Y_{\text{FABLE}}(\theta)}{Y_{\text{Ruth}}(\theta)} \frac{d\sigma_{\text{Ruth}}(\theta)}{d\Omega} \frac{\epsilon_{\text{FABLE}}}{\epsilon_{\text{Ruth}}}, \tag{7.1}$$

where $\frac{d\sigma_{\text{FABLE}}(\theta)}{d\Omega}$ is the differential cross section for a reaction product with yield $Y_{\text{FABLE}}(\theta)$ measured in FABLE, $\frac{d\sigma_{\text{Ruth}}(\theta)}{d\Omega}$ is the Rutherford cross section at that same angle, Y_{Ruth} are the monitor counts of Rutherford scattering, ϵ_{FABLE} is the efficiency for measuring the reaction product of interest in FABLE, and ϵ_{Ruth} is the Rutherford scattering measurement efficiency. These efficiency terms correspond to the scaling and pairing correction factors, which were discussed in detail in Sec. 6.4.3.

7.2 Characterization of α Evaporation

The measurement of ^{7}Be + ^{208}Pb formed the compound nucleus of sufficiently high excitation energies so that in the data will be some α-yields arising from αxn evaporation from the target-like nucleus. As these may have energies similar to those of α-yield resulting from breakup or incomplete fusion, they need to be characterized and subtracted from the data. To estimate the

α evaporation cross section, the statistical model code PACE4 was used to calculate the fusion evaporation differential cross section [23, 24]. The calculation was performed using a level density parameter of $K = 12$, which was chosen by matching the xn fusion relative excitation functions to those measured by Dasgupta et al. for ^{6}Li + ^{209}Bi, which forms the same compound nucleus, in Ref [5], but has the full excitation functions constraining PACE calculations unlike the present experiment. This matching included a 1.7 MeV shift in beam energy, as mentioned in the reference for matching calculations for ^{7}Li + ^{209}Bi due to the angular momentum distribution being difficult to model when incomplete fusion is significant. All other settings were default and potential parametrization were calculated from systematics. The integrated αxn evaporation cross section was $\sigma_{\text{evap}} = 86.6 \pm 0.9$ mb. The differential cross section for the αxn evaporation calculation is shown alongside the other α cross sections in Fig. 7.1, and the evaporation contribution is subtracted off wherever there was measured α-yield to arrive at the unaccompanied distribution. Calculations with level density parameters of $K = 11, 13$ were also tested, but the differential cross section remained similar. The uncertainty used in the presented calculation is purely statistical.

7.3 Unaccompanied Cross Sections

One can determine the cross section for generating a particle in the exit channel due to no-capture breakup by summing the cross sections for no-capture breakup exit channels that emit each particle. This is important in the case of the α cross section, where α-particles can be generated from multiple breakup modes, and in the case of ^{8}Be decay, two α-particles are generated from a single reaction. Therefore, the cross section associated with α production in the exit channel due to no-capture breakup can be written as

$$\sigma_{\alpha}(\text{NCBU}) = 2\sigma_{\alpha\alpha} + \sigma_{\alpha^{3}\text{He}} + \sigma_{\alpha d}, \tag{7.2}$$

where the subscripts indicate each no-capture breakup exit channel. Meanwhile, the yield of ^{3}He due to breakup, $\sigma_{^{3}\text{He}}$, comes simply from the no-capture breakup cross section for $^{7}\text{Be} \rightarrow \alpha + {}^{3}\text{He}$. The unaccompanied α cross section, is then given by

$$\sigma_{\text{unacc}}(\alpha) = \sigma_{\alpha} - \sigma_{\alpha}(\text{NCBU}) - \sigma_{\text{evap}}, \tag{7.3}$$

and in the case of ^{3}He, there are no evaporation particles to account for, so the cross section is simply

$$\sigma_{\text{unacc}}(^3\text{He}) = \sigma_{^3\text{He}} - \sigma_{^3\text{He}}(\text{NCBU}). \tag{7.4}$$

Figure 7.1 shows the differential cross section for the unaccompanied α in black, along with its components, including the breakup (red) and singles (blue) cross sections and the PACE calculation (pink). Points associated with scattering angles between 84-96° have been discarded even though there was some detector coverage due to issues with precise determination of the solid angle at the detector edges. In this region, the average of multiple linear interpolations, by conducting multiple fits while including or excluding fitted points, was employed to obtain approximate values and uncertainties for the cross section at the middle angles for the purposes of integration. At 18-20° in the α spectrum, these points were discarded due to apparent contributions from light impurities that could not be removed from the yield. These points were instead extrapolated, in addition to points where there was a lack of statistics or detector coverage. Extrapolations at the most forward and backward angles were also used in integration. The integrated cross sections give the cross sections for α and ^{3}He production leading to incomplete fusion, respectively. The integrated cross sections are shown in Table 7.1.

The unaccompanied differential cross section for ^{3}He along with its components are shown in Fig. 7.2. Linear interpolations and extrapolated were employed in the shaded regions for the singles spectrum (blue), but in the breakup cross sections (red), only interpolation between 84-96° was used, without extrapolations at forward and backward angles. Similar to the singles α spectrum, there is a shoulder at forward angles in the singles ^{3}He differential cross section that propagates into the unaccompanied distribution. This again can be attributed to imperfect removal of light impurity reaction products in the yields.

The unaccompanied α and ^{3}He cross sections look quite different to each other, as can be seen in Fig. 7.3, where they are compared along the same axis. The α-spectrum is much larger, and peaks at a much more forward angle than that of the ^{3}He spectrum. Interpreting this in the view of classical scattering, one can observe that more peripheral (smaller θ, larger b) reactions on average

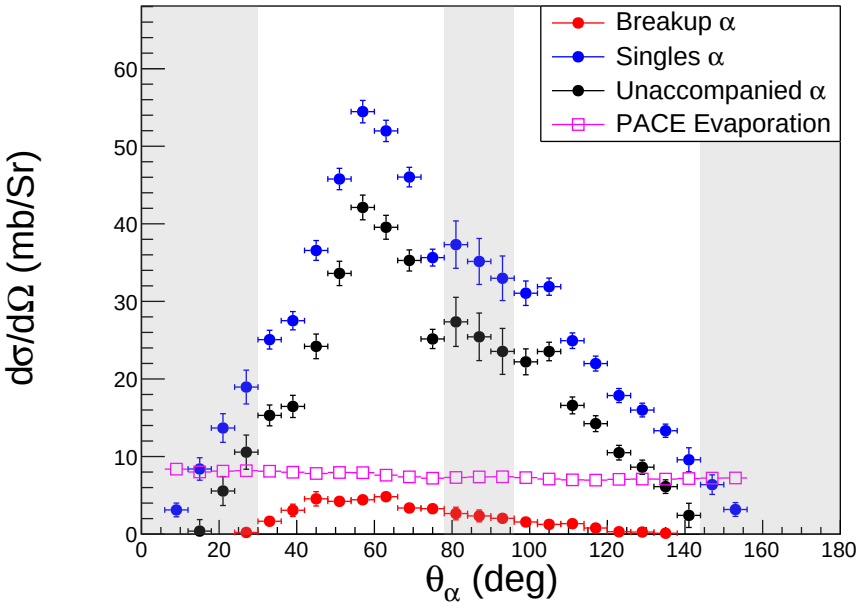

Figure 7.1 Differential cross sections for α-particles resulting from reactions of ^{7}Be + ^{208}Pb plotted as a function of the laboratory-frame angle of the escaping α, θ_α. The cross section for α-yield resulting from all breakup modes is plotted in red. The singles α cross section is plotted in blue. The difference of the two gives the unaccompanied-α differential cross section, plotted in black. α evaporation cross sections calculated with PACE are plotted in the open pink squares and their associated statistical uncertainties are plotted, but small. Shaded regions indicate data that has been linearly interpolated or extrapolated (see discussion in the text).

σ	α	^{3}He
Singles	352 ± 8 mb	161 ± 6 mb
Breakup	24 ± 3 mb	9 ± 2 mb
Evaporation	86.6 ± 0.9 mb	–
Unaccompanied	241 ± 8 mb	152 ± 6 mb

Table 7.1 Integrated cross sections for breakup and total generation of α and ^{3}He, along with the unaccompanied cross sections, correspond to cross sections for incomplete fusion leading to the escape of each fragment.

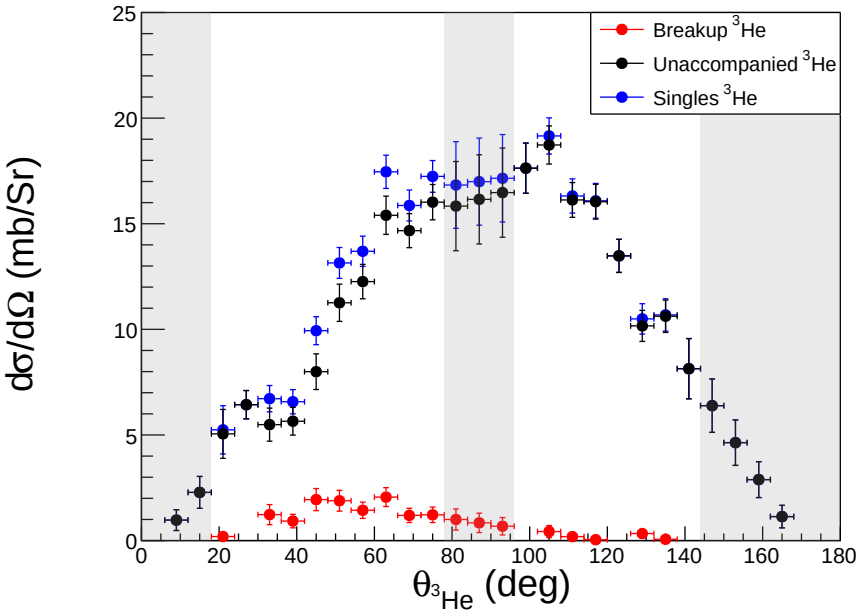

Figure 7.2 Differential cross sections for ^{3}He resulting from reactions of ^{7}Be+^{208}Pb plotted as a function of the laboratory-frame angle of the escaping ^{3}He, $\theta_{^3He}$. The cross section for ^{3}He resulting from all breakup modes is plotted in red. The singles ^{3}He cross section is plotted in blue. The difference of the two gives the unaccompanied ^{3}He differential cross section, plotted in black. Shaded regions indicate data that has been linearly interpolated or extrapolated in the singles spectrum, but the breakup cross sections were only interpolated in between 84-96° (see discussion in the text).

lead to the generation of α incomplete fusion yields when compared to the ^{3}He yields. This may be expected – the only expected reactions leading to ^{3}He in the exit channel are those *without* transfer, meaning absorption of an α-cluster in ^{7}Be either directly or following Coulomb breakup. Meanwhile, α-yields from incomplete fusion can follow from transfer-triggered breakup channels, which may be more peripheral, in addition to the ^{7}Be entrance channel. However, contributions from breakup are small in comparison to the unaccompanied cross sections. This could be a possible signal of a "Trojan Horse" effect – the weakly-bound projectile of form $P = A + B$, with its weakly-bound charged clusters being a heavier particle, A, and some secondary, lighter cluster, B, is able to achieve a shorter distance-of-closest approach because the heavier A-particle shields B from Coulomb repulsion of the target and instead brings it along a smaller ℓ trajectory, leading to enhanced direct transfer of B in comparison to the direct fusion of B alone to some target. This

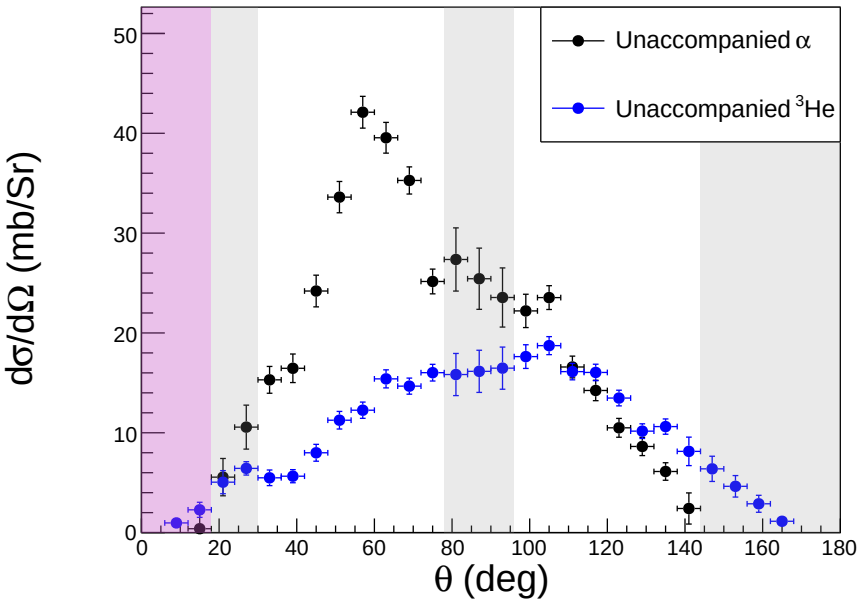

Figure 7.3 Plot of the differential unaccompanied cross sections with respect to the scattering angle of the escaping particle for α (in black) and ^{3}He (in blue). Shaded gray regions indicate data that has been linearly interpolated or extrapolated, except for ^{3}He at forward angles, which had its extrapolation region shortened to only the magenta-shaded region.

is because, for the same $E_{\mathrm{CM}}/A_{\mathrm{proj}}$, the higher total energy for the cluster transfer with A puts the overall reaction at an energy higher above the Coulomb barrier [38, 39].

The total fusion cross section for ^{7}Be was calculated using a coupled channels calculation provided by the *CCFULL* program [22]. This calculation was employed to determine an incomplete fusion factor,

$$F_{\mathrm{ICF}} = \frac{\sigma_{\mathrm{ICF}}}{\sigma_{\mathrm{CF}} + \sigma_{\mathrm{ICF}}} = \frac{\sigma_{\mathrm{ICF}}}{\sigma_{\mathrm{TF}}}, \tag{7.5}$$

where the calculated total fusion cross section, σ_{TF}, is used to scale the incomplete fusion cross section. This then quantifies the degree of complete fusion suppression observed in a given reaction. The incomplete fusion cross section for this experiment was taken as the sum of the unaccompanied cross sections for the ^{3,4}He isotopes previously discussed. While there may be a contribution of deuterons to the incomplete fusion cross section, the unaccompanied deuteron spectrum was not able to be reliably extracted in this work and has been excluded from the sum, but is likely to be small since the α and ^{3}He are the primary components of the cluster structure in ^{7}Be.

The expected total fusion cross section without the effects of weak binding was calculated by employing the coupled channels program, *CCFULL* [22]. The input parameters (V_0, r_0, a_0) for the Woods-Saxon potential used in the calculations was based off values given by the Saõ Paulo Potential. The fusion barrier energy extracted from these calculations was $V_b = 39.44$ MeV, which well matches the fusion barrier extracted from the optical model fit of elastic scattering measurement of ^{7}Be on ^{208}Pb by Mazzocco et al. [40], in which they found to be 39.45 MeV. The uncertainty in the total fusion cross section was determined by making several calculations of the total fusion cross sections with slight variations in the barrier depth parameter, V_0, and plotting the absolute difference $|\sigma_{\mathrm{TF}}(V_0) - \sigma_{\mathrm{TF}}(V_B = 39.44\ \mathrm{MeV})|$ as a function of the resulting barrier energy, V_B, as shown in Fig. 7.4. By taking the average difference in the total fusion cross section at $V_B \pm 500$ keV the uncertainty is estimated. The variance of the barrier energy was chosen to be 500 keV since the fusion excitation function for this reaction has not been measured, so the range presented roughly captures some uncertainty in the chosen barrier energy. This results in a calculated total fusion cross section of 790 ± 60 mb.

For the laboratory frame incident energy of 51.74 MeV ($E_{\mathrm{CM}} = 50.05$ MeV), the incomplete fusion factor determined in this work for ^{7}Be + ^{208}Pb was found to be $F_{\mathrm{ICF}} = 0.50 \pm 0.04$.

7.4 Conclusion

In this chapter, the unaccompanied ^{3,4}He differential and integrated cross sections were extracted for reactions of ^{7}Be + ^{208}Pb at $E_{\mathrm{CM}} = 50.05$ MeV, at 1.3 times the barrier energy and the incomplete fusion factor was determined with respect to a total fusion calculation using *CCFULL*. In the next chapter, this result is considered in the context of other incomplete fusion factor measurements with weakly-bound nuclei. Additionally, the no-capture breakup dynamics and incomplete fusion yields of ^{7}Be are compared to those of ^{6,7}Li to better understand the role of nuclear structure and cluster binding in the near-barrier reaction dynamics.

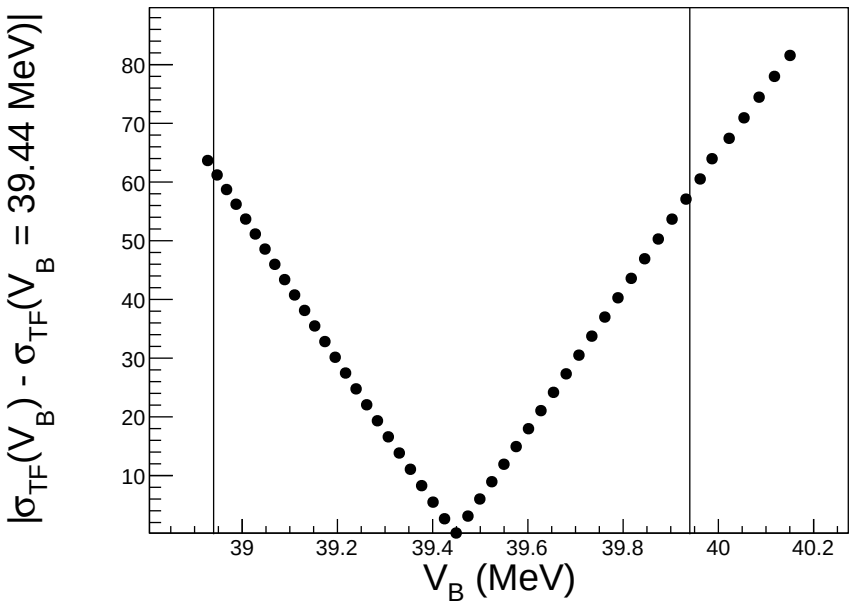

Figure 7.4 Absolute difference in total fusion cross section for a barrier energy and the chosen total fusion cross section for ^{7}Be + ^{208}Pb at E_{lab} = 51.74 MeV based on the SPP potential parameterization plotted against the barrier energy from the resulting calculation with *CCFULL*. The vertical lines indicate $V_B \pm 500$ keV.

CHAPTER 8

DISCUSSION AND CONCLUSION

In the last chapter, unaccompanied helium cross sections were extracted for the measurement of ^{7}Be + ^{208}Pb at E_{CM} = 50.05 MeV, 1.3 times the fusion barrier energy. From these, an incomplete fusion cross section and incomplete fusion factor of $F_{ICF} = 0.50 \pm 0.04$ were determined. I will now consider the implications of these results by way of a direct comparison to the mirror nucleus ^{7}Li and also within the broader context of other studies of the complete fusion suppression of weakly-bound nuclei.

8.1 Complete Fusion Suppression of ^{7}Be in the Context of Prior Measurements

In Fig. 8.1 shows an updated version of the dependence of F_{ICF} on charged particle breakup threshold, with now the inclusion of the ^{7}Be incomplete fusion measurement. Note that the exponential fit to radioactive isotopes, indicated by the red line, *excluded* the ^{7}Be point measured in this work, but is still in agreement with the value. In this context, an enhancement of incomplete fusion yields in the radioactive and weakly-bound nuclei is further substantiated. While it may be expected that the structure of the weakly-bound nucleus (similar to ^{7}Li) and its breakup threshold (similar to ^{6}Li) would be the predominant influence on the mechanism of the resulting complete fusion suppression, this measurement is in disagreement with this notion.

8.2 Comparison to ^{6,7}Li + ^{209}Bi

There have been various breakup and fusion measurements of ^{6,7}Li before this work. I shall consider comparisons of breakup in available data of ^{7}Li + ^{209}Bi, measured at a matching beam energy to barrier energy ratio of 1.3 measured in this work's study of ^{7}Be to better understand how structure may or may not influence the breakup dynamics. These ^{7}Li breakup data are courtesy of Cook et al., measured at the Heavy Ion Accelerator Facility located at the Australian National University, which is the basis of Ref. [11]. The comparison relative energy spectra with the same $\alpha + \alpha$ exit channel are shown in Fig. 8.2 by way of neutron-pickup for ^{7}Be and proton-pickup for ^{7}Li. Figure 8.3 compares relative energy spectra in the $\alpha + d$ exit channel via proton-stripping for

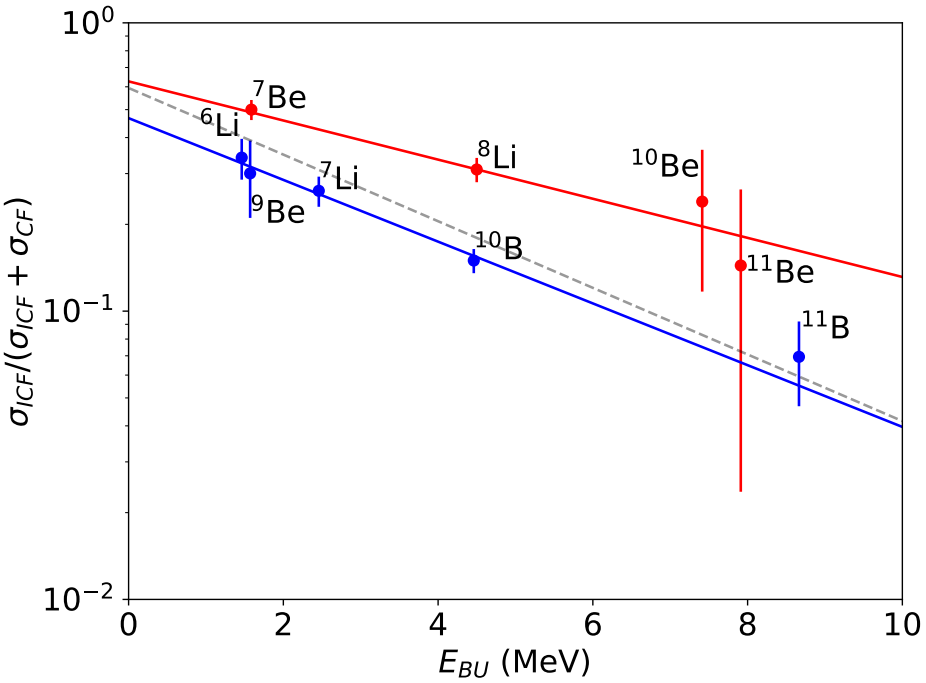

Figure 8.1 Updated version of Fig. 1.3, plotting the F_{ICF} for different isotopes against their breakup threshold into two charged fragments. Blue points indicate stable beam measurements and red points indicate radioactive ion beam experiments. The solid blue line plots an exponential fit to the stable beam data and in red is an exponential fit to the radioactive ion beam data, excluding the ^{7}Be point presented in this work. The dashed, grey line indicates an exponential fit to all data. With the inclusion of the ^{7}Be measurement from this work, the trend of enhancement of incomplete fusion yields in radioactive isotopes is further supported. Additional F_{ICF} data from Refs. [5–9].

^{7}Be and neutron-stripping for ^{7}Li. Despite the fact that the initial transfer reactions are different to populate the ^{8}Be and ^{6}Li resonances, the breakup appears to match within uncertainty for each experiment, but since the ^{7}Be statistics were so low, it is difficult to comment on the strength of agreement or disagreement.

The breakup orientations in the $\alpha + d$ exit channel might reveal discrepancy between the two reactions. Figure 8.4 shows the breakup orientation matrix for the ^{7}Li experiment [11] (left) in comparison to the present work (right). For $^{7}\mathrm{Li} + {}^{209}\mathrm{Bi} \rightarrow {}^{6}\mathrm{Li}^{*} + {}^{210}\mathrm{Bi} \rightarrow \alpha + d + {}^{210}\mathrm{Bi}$, not only is breakup visible through the 3^{+} resonance, but there are also clear contributions from non-resonant breakup. However, for $^{7}\mathrm{Be} + {}^{208}\mathrm{Pb} \rightarrow {}^{6}\mathrm{Li}^{*} + {}^{209}\mathrm{Bi} \rightarrow \alpha + d + {}^{209}\mathrm{Bi}$, there is no clear significant contribution of non-resonant breakup. In addition, the *KOOKABURRA* simulation of

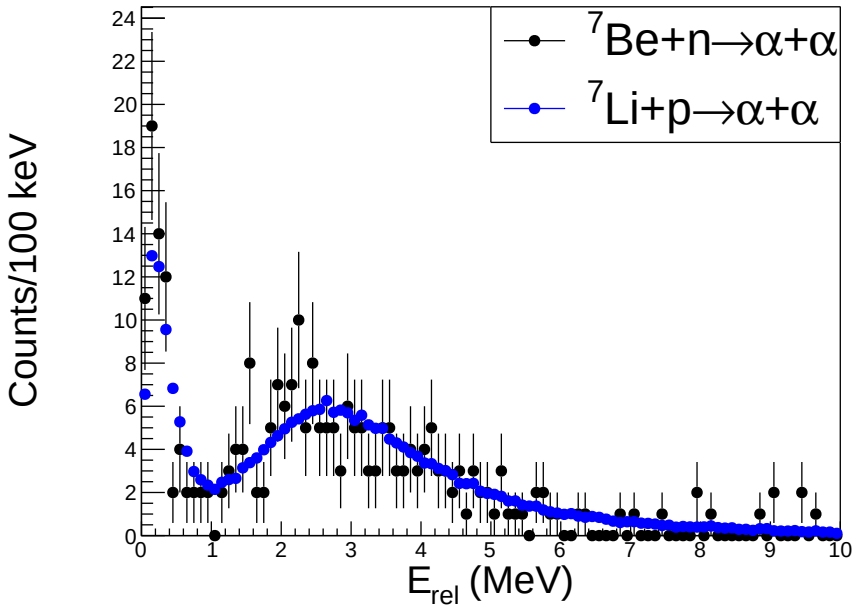

Figure 8.2 Relative energy spectra comparing the breakup of $^{7}\mathrm{Li} + p \rightarrow \alpha + \alpha$ in reactions of ^{7}Li on ^{209}Bi at E_{CM} = 38.7 MeV, from Cook et al. (see Ref. [11]) to the matching exit channel in this work. Note that the beam energies are at a matching beam energy to barrier energy ratio. The error bars represent statistical error, and in the case of the ^{7}Li data, counts and associated uncertainties have been scaled down to match the overall statistics of the ^{7}Be data.

this breakup channel accurately reproduced the experimental E_{rel} spectrum with only a 3^{+} resonant breakup contribution. This suggests that in spite of the different transfer reactions, each transfer is isospin-symmetric, which seems to be the predominant predictor for the excitation energy of the projectile-like resonance prior to breakup, but the resonance structure through which breakup occurs may appear different in the breakup orientation spectra. With such low statistics in the case of the ^{7}Be dataset, it is possible that there is some non-resonant breakup at larger θ_{12}, but it cannot be clearly identified with such few counts. However, based on the relative intensities of non-resonant and resonant breakup in the ^{7}Li experiment, perhaps one might expect more non-resonant breakup in the orientation matrix for the ^{7}Be experiment than what is visible.

This may lead one to believe that because the breakup of the two mirror nuclei, ^{7}Be and ^{7}Li, are similar due to their underlying structure, that their (in)complete fusion should also be similar. This is incorrect. As mentioned in the last chapter, the incomplete fusion factor for ^{7}Be was found in this work to be 0.50 ± 0.04, which is *much* higher than that of both ^{6}Li (F_{ICF} = 0.34 ± 0.06)

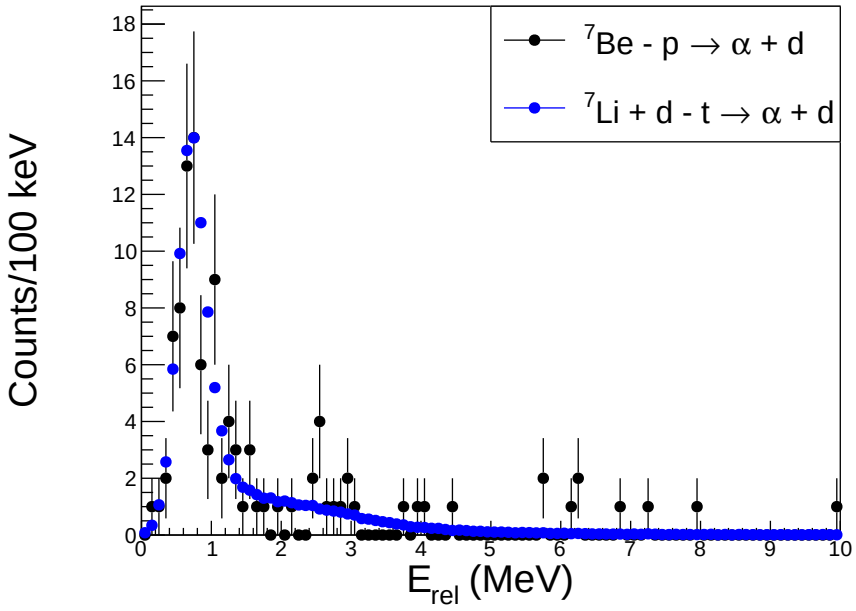

Figure 8.3 Relative energy spectra comparing the breakup of $^7\mathrm{Li} + d - t \rightarrow \alpha + d$ in reactions of ^{7}Li on ^{209}Bi at $E_{\mathrm{CM}} = 38$ MeV, from Cook et al. (see Ref. [11]) to the matching exit channel in this work. Note that the beam energies are at a matching beam energy to barrier energy ratio. The error bars represent statistical error, and in the case of the ^{7}Li data, counts and associated uncertainties have been scaled down to match the overall statistics of the ^{7}Be data. Note the different scales of the color axes.

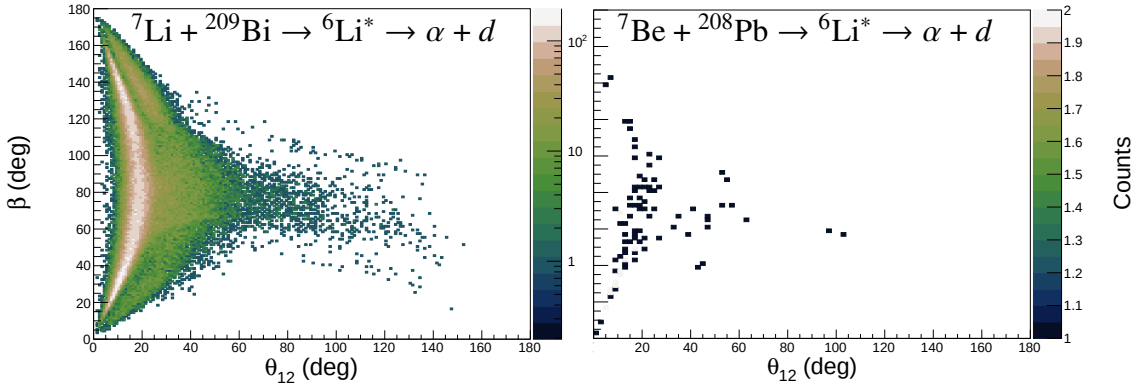

Figure 8.4 Comparison of the breakup orientation matrix for the transfer-triggered breakup of $^7\mathrm{Li} + {}^{209}\mathrm{Bi} \rightarrow {}^6\mathrm{Li}^* \rightarrow \alpha + d$ at $E_{\mathrm{CM}} = 38.7$ MeV (left) measured by Cook et al. [11] to the breakup orientation matrix of $^7\mathrm{Be} + {}^{208}\mathrm{Pb} \rightarrow {}^6\mathrm{Li}^* \rightarrow \alpha + d$ at $E_{\mathrm{CM}} = 50.05$ MeV (right), presented in this work. These measurements were both performed at similar $E/V_B = 1.3$. Note that there are clear contributions from both non-resonant breakup and resonant breakup in the ^{7}Li data, while it is not as apparent in the ^{7}Be data, even with low statistics.

Reaction	E_{CM} (MeV)	Unacc.	Rel. Intensity	σ_{ICF} (mb)	$Q_{transfer}$ (MeV)
^{7}Be + ^{208}Pb [(a)]	50.05	α	61 ± 3%	241 ± 8	4.03
		^{3}He	39 ± 2%	152 ± 6	-10.54
^{6}Li + ^{209}Bi[(b)]	38.81	α	63 ± 3%	148 ± 4	5.84
		d	37 ± 5%	87 ± 10	-10.73
^{7}Li + ^{209}Bi[(b,c)]	38.63	α	80 ± 8%	256 ± 21	4.59
		t	20 ± 2%	65 ± 3	-11.7

(a) This work

(b) Dasgupta et al., Ref. [5]

(c) Cook et al., Ref. [11]

Table 8.1 Cross sections for unaccompanied particles resulting from incomplete fusion measured at $1.3 \times E_{beam}/V_B$ for ^{7}Be on ^{208}Pb and ^{6,7}Li on ^{209}Bi. The relative intensities for each unaccompanied particle are provided. The Q-values for direct cluster transfer leading to incomplete fusion are also indicated, which are calculated via mass excesses based on mass evaluations from Ref. [41].

and ^{7}Li (F_{ICF} = 0.26 ± 0.03) [5], even though the breakup thresholds of ^{7}Be and ^{6}Li are nearly identical, as shown in Fig. 8.1 in the prior section.

The comparison of incomplete fusion yields in ^{7}Be and ^{6,7}Li may be informative to better understand why the breakup looks so similar, but the complete fusion suppression is so different. Table 8.1 compares the cross sections for incomplete fusion, resulting in the escaping α or secondary fragment for each of these isotopes in reactions at a matching beam energy to fusion barrier energy ratio of 1.3. The Q-values for direct cluster transfer in each case are also indicated. Plotted in Fig. 8.5 are the relative intensities for incomplete fusion yields for each reaction resulting in either an unaccompanied α or secondary cluster. While the overall fusion is significantly enhanced in ^{7}Be in comparison to ^{6,7}Li, the relative intensities of escaping versus absorbed fragments better match for ^{7}Be and ^{6}Li, showing that there is perhaps some correlation between clustered breakup threshold and direct cluster transfer orientations. At the same time, it is then strange that the relative intensities between the unaccompanied α and ^{3}He/t differ so greatly when comparing the incomplete fusion cross sections of ^{7}Be and^{7}Li when the difference in their breakup thresholds is also small. Furthermore, the transfer Q-values for ^{7}Be and ^{7}Li cases are also close, making the difference in both relative intensities and overall intensities surprising. In all cases, the α-particle is more likely to escape in incomplete fusion than their alternative cluster. This makes sense when considering the Q-value for direct cluster transfer in each process and the Trojan horse mechanism

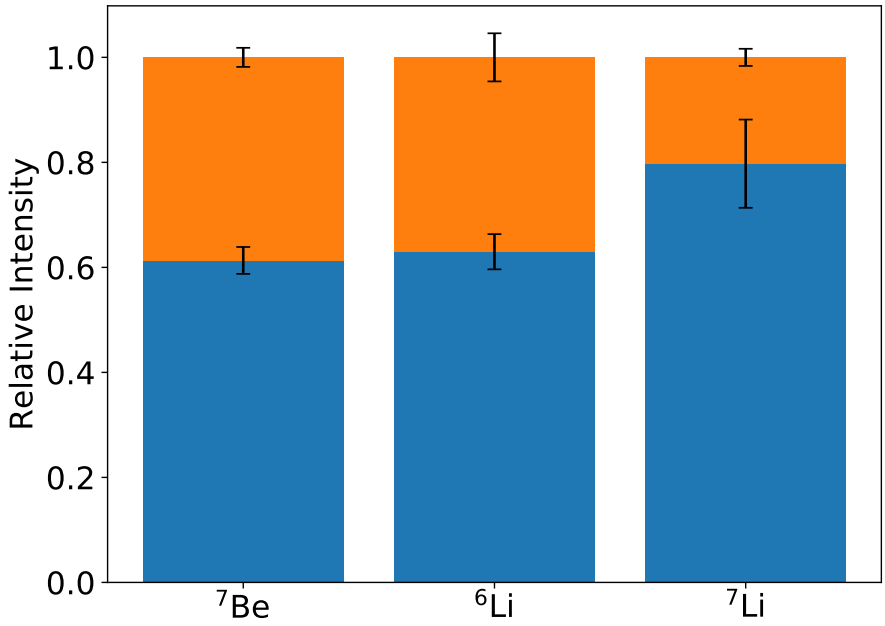

Figure 8.5 Stacked bar chart plotting the relative intensities of incomplete fusion cross sections associated with an unaccompanied α (in blue) or secondary cluster (^{3}He, d, t, in orange) for ^{7}Be and ^{6,7}Li [5, 11]. There is good agreement in the relative intensities between ^{7}Be and ^{6}Li.

Exit Channel	σ (mb) from ^{7}Li	σ (mb) from ^{7}Be
$\alpha + t/^{3}$He	9.6 ± 0.6	7.9 ± 2
$\alpha + d$	10.8 ± 0.5	3.2 ± 0.6
$\alpha + \alpha$	7.3 ± 0.4	4.5 ± 1

Table 8.2 Comparison of no-capture breakup cross sections for ^{7}Li + ^{209}Bi at E_{CM} = 38.7 MeV [17] [11] to those of ^{7}Be + ^{208}Pb at E_{CM} = 50.05 MeV, measured in this work. The $\alpha + t$ exit channel corresponds to breakup of ^{7}Li and $\alpha + ^{3}$He to breakup of ^{7}Be.

[38], but cannot be explained easily with breakup alone.

The no-capture breakup cross sections of the ^{7}Li and ^{7}Be studies can also be compared. The cross sections for each exit channel is indicated in Table 8.2. Here, it is shown that the no-capture breakup cross sections are smaller in every exit channel for the ^{7}Be reactions than the ^{7}Li reactions. Presumably, if there is breakup, at least one of the fragments is captured more often for ^{7}Be than ^{7}Li in view of the incomplete fusion cross sections.

8.3 Influence of Cluster Charge-to-Mass Ratios in Fusion Reactions

While structure of the weakly-bound projectile is integral to the *breakup* reactions, the dynamics of incomplete fusion, which include not only sequential breakup capture, but also direct cluster transfer, are influenced first by something else. This could be the breakup threshold to clusters, but if this is the case, why should some weakly-bound isotopes have such enhanced incomplete fusion cross sections just because they are radioactive, but have otherwise typical structures? Many of the studied radioactive nuclei, like ^{7}Be, are not exotic in structure.

I propose that a different quantity, instead of breakup threshold, better models and predicts complete fusion suppression and merge the discrepancy between the stable and radioisotopes. I construct such a quantity by considering both the properties of the weakly-bound projectile and its constituent charged clusters. Consider a weakly-bound isotope, p, such that it has low breakup threshold to disintegrate into two charged fragments, $p \rightarrow 1+2$. The parameter then is constructed from the proton numbers of the particle and its clusters, Z_p, Z_1, Z_2, the masses, m_p, m_1, m_2, and charge radii ρ_p, ρ_1, and ρ_2.

Recall the form of the Coulomb force between two particles,

$$\vec{F} = \frac{kQ_1Q_2}{r^2}\hat{r}, \tag{8.1}$$

where Q_1, Q_2 are the charges of the two particles, r is the distance between them, and k is the Coulomb constant. If one were to construct a "force-like" term from the parameters enumerated. the product of the proton numbers in each fragment, Z_1Z_2, acts as natural choice to represent the charge product component in the Coulomb force between two particles. This means that the magnitude of acceleration of each fragment, a_1 and a_2, is proportional to the ratio between this product and the cluster particle mass.

However, to construct a full term to represent the acceleration of each fragment, the radial terms are required. To do this, I propose the to use the charge radii. Specifically, by taking the difference between the charge radius of each cluster and the charge radius of the whole projectile, two radial

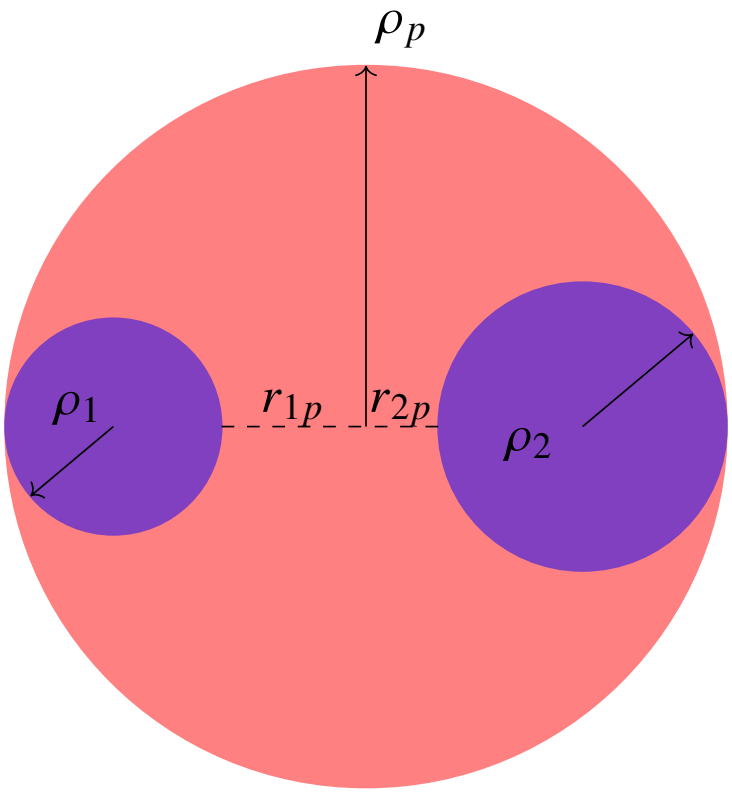

Figure 8.6 Cartoon illustrating the properties of the clusters within a weakly-bound isotope. The charge radius of the projectile, ρ_p, and its component clusters, $\rho_{1,2}$ are labeled. Each radial term is taken as the difference between charge radii. The proposed quantity to predict F_{ICF} emulates the force between the component clusters within the nucleus.

terms can be constructed:

$$r_{1p} = |\rho_p - \rho_1|, \qquad r_{2p} = |\rho_p - \rho_2|. \tag{8.2}$$

See Fig. 8.6 for a visualization of the relationship between the various charge radii. Each radial term r_{1p} and r_{2p} serve to quantify the asymmetry of the charge distribution based on clustering within the nucleus. The product of these two radial terms then allows us to construct the "force-like" term,

$$\vec{F} \propto \frac{Z_1 Z_2}{r_{1p} r_{2p}}. \tag{8.3}$$

If one wanted to write a term corresponding to a term with dimensionality of acceleration for each charged cluster within the nucleus based on this force term, we can write $a_1 = F/m_1$ and $a_2 = F_{12}/m_2$. Combining these two acceleration components for each cluster, we find that a "net"

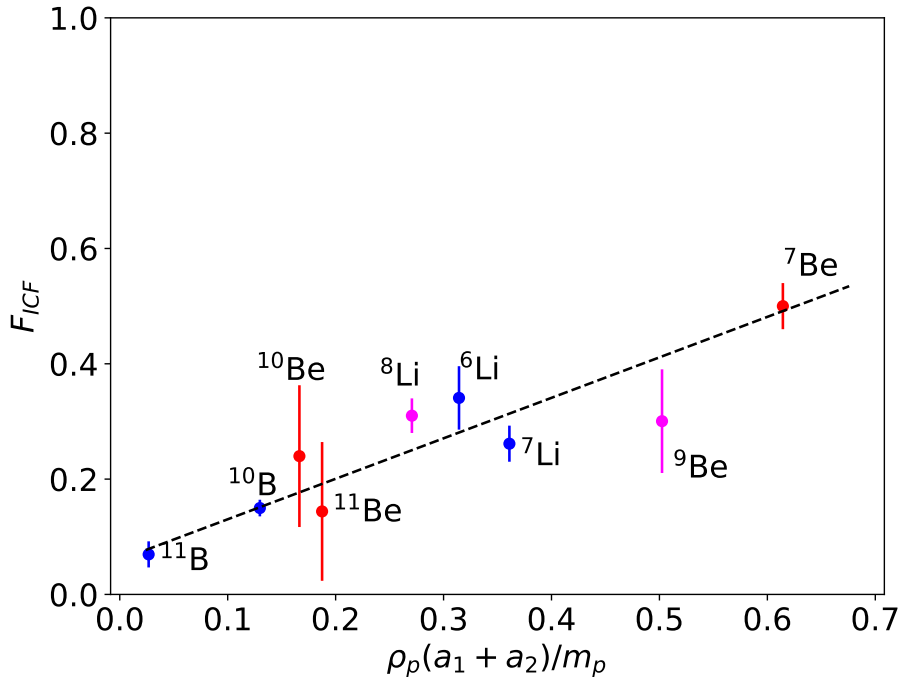

Figure 8.7 Incomplete fusion factors for different weakly-bound isotopes plotted against the quantity proposed in the text. This quantity scales with the magnitude of accelerations between the charged clusters within each isotope divided by the linear charge density of the weakly-bound isotope itself. Blue points indicate stable beam measurements and red points indicate radioactive ion beam measurements. Magenta points indicate instances where the charge radii of the projectile clusters have not been measured – specifically of ^{5}He, and have instead used the charge radius of ^{4}He in the determination. The black dashed line indicates a linear fit to the data, with mean-squared error 0.00. Additional F_{ICF} data from Refs. [5–9]. Charge radii measurements are from Ref. [42] and nuclear masses are from the Atomic Mass Evaluation [41].

acceleration parameter is

$$a_{12} = a_1 + a_2 = \frac{Z_1 Z_2}{|\rho_p - \rho_1||\rho_p - \rho_2|}\left(\frac{1}{m_1} + \frac{1}{m_2}\right). \tag{8.4}$$

With greater "acceleration," the more easily clusters can be separated, or of relevance in this work, perhaps *individually* transferred. Finally, the parameter is scaled to the linear charge density ρ_p/m_p for each isotope. Figure 8.7 plots the incomplete fusion factors against this proposed quantity. Note that in the cases of ^{8}Li and ^{9}Be, one of the expected clusters, ^{5}He, does not have an experimentally measured charge radius. For this reason, these points have been colored magenta and the charge radius of ^{4}He has been used, instead, since the lifetime of ^{5}He is so short compared to the timescales of the reactions of interest. In this figure, there is no longer as wide of a separation

between stable and radioactive weakly-bound nuclei, as can be seen when only examining the breakup threshold. The linear fit to data, indicated by the dashed line, does not agree to all points within uncertainty but captures the overall trend of the incomplete fusion factor.

To compare the parametrization of F_{ICF} by breakup threshold versus the proposed quantity, the error in each fit to all data is quantified as a weighted sum of the residuals, or

$$E = \sum \frac{|F_{\mathrm{ICF}} - \hat{F}_{\mathrm{ICF}}|}{\Delta F_{\mathrm{ICF}}^2}, \tag{8.5}$$

where the uncertainty E is the sum of the difference between the measured F_{ICF} and predicted $\hat{F}_{\mathrm{ICF}}$, weighted by the uncertainty each measurement, ΔF_{ICF}. The error in the exponential fit based on clustered breakup threshold, indicated by the gray line in Fig. 8.1, is $E = 482$. Meanwhile, the error in the linear fit to the proposed parametrization, indicated by the black line in Fig. 8.7, is $E = 192$. Note that the magnitude of these error terms are large because they are scaled by large weight terms. The important aspect of this error analysis is that the error in the fit by the proposed quantity is less than half that of the fit by breakup threshold. This demonstrates that the parametrization proposed more accurately reflects the measured incomplete fusion factors.

8.4 Conclusion

In this work, the no-capture breakup and incomplete fusion of ^{7}Be on ^{208}Pb was measured at an energy 1.3 times the fusion barrier energy. After extracting unaccompanied ^{3,4}He cross sections, the incomplete fusion cross section for ^{7}Be at this energy was determined. Additionally, by calculating a complete fusion cross section with *CCFULL* [22], the incomplete fusion factor for ^{7}Be in this experiment was found to be $F_{\mathrm{ICF}} = 0.50 \pm 0.04$. This finding is in surprising agreement with the trend in prior studies of weakly-bound nuclei that showed an enhancement of incomplete fusion yields and complete fusion suppression in comparison to those of stable, weakly-bound nuclei.

The comparison between breakup and fusion of ^{7}Be to reactions of ^{6,7}Li show that breakup threshold and low-lying structure cannot fully explain the mechanism for complete fusion suppression. Additionally, the comparison of incomplete fusion products provides further evidence for a "Trojan Horse" mechanism by which direct cluster transfer is enhanced in weakly-bound nuclei.

Additional breakup calculations that more properly model the capture of breakup fragments is still necessary to understand the evidence of direct cluster transfer as a mechanism for complete fusion suppression in ^{7}Be, as has been observed in ^{7}Li [11]. There were difficulties in applying simulations with *KOOKABURRA* to accurately model absorption effects in this work due to large uncertainties in the breakup functions, but calculations that constrain cross sections associated with breakup and breakup-capture are critical to demonstrating the role of cluster transfer in the observed enhancement of incomplete fusion.

Furthermore, calculations that carefully model cluster-cluster interactions within the weakly-bound projectile along its trajectory would prove beneficial in forming a more complete description of the mechanism of complete fusion suppression, as well as describe the apparent enhancement of direct cluster transfer. One natural choice of model would be the IAV model of breakup, since it has already been applied in calculations of ^{6,7}Li reactions [39].

A measurement of the complete fusion cross section in ^{7}Be + ^{208}Pb would be beneficial for constraining the F_{ICF} presented in this work. Part of the original experimental campaign described in this work was to do so by measuring the decay α resulting from fusion products implanted onto an aluminum "catcher" foil following irradiation of the ^{208}Pb target, but the resulting decay spectrum could not be fully de-convoluted [37]. Additionally, only one energy was able to be measured in this work. While prior studies have shown that the incident energy does not change the resulting incomplete fusion factors [5], measurements of the same reaction system at different energies would not only improve the constraint on the incomplete fusion cross section, but also the fusion barrier energy.

Further measurements of incomplete fusion reactions in previously-measured isotopes, but by way of the unaccompanied charged particle method may prove useful in understanding the role of clustering in fusion and breakup, especially in cases where there is asymmetry in the $\alpha + x$ clustering. For example, while incomplete fusion factors for ^{10,11}Be have been measured already [8, 12], the unaccompanied charged particle spectra that may be extracted in another near-barrier study would better constrain the effects of asymmetric clustering in transfer. In one recent measurement

of near-barrier reactions of ^{10}B + ^{209}Bi [43], singles production cross sections were extracted and coincident α+α exit channels of breakup were studied, but a measurement of the no-capture breakup differential cross sections of each breakup channel would allow for extraction of unaccompanied particle cross sections. By studying the various breakup exit channels observable through reactions of ^{10}B, the mechanism by which cluster transfer is enhanced can be better understood. Alternatively, an above-barrier measurement of ^{14}N would prove useful for analyzing cluster asymmetry in fusion dynamics.^{14}N has higher energy, but accessible, resonances that are unbound to a variety of different charged fragment decays, such as ^{13}C + p (E_{BU} = 7.5 MeV), ^{12}C + d (E_{BU} = 10.27 MeV) and ^{10}B + α (E_{BU} = 10.55 MeV) [44]. While the cross sections would be small, high beam intensities with a stable beam are achievable and the measurement would provide plenty of asymmetry with which to probe how clustering influences both transfer and breakup. Of course, investigating the reaction dynamics with more exotic nuclei would prove useful in attaining more asymmetric cluster structures, but such measurements may be difficult to achieve without improved beam intensities.

In conclusion, the measurement of no-capture breakup and incomplete fusion in ^{7}Be + ^{208}Pb further substantiated evidence of incomplete fusion enhancement in radioactive isotopes. With the statistics achieved in the present work, it is difficult to draw conclusions in the comparison to prior ^{6,7}Li measurements to better understand the role of structure and breakup in near-barrier reactions with weakly-bound nuclei, this measurement demonstrates further evidence of direct cluster transfer as a mechanism of complete fusion suppression and suggests that further study of clustering effects in weakly-bound nuclei is necessary to disentangle the relationship between near-barrier reaction dynamics and the structures of the participant reactants.

BIBLIOGRAPHY

[1]M. Dasgupta, D. Hinde, N. Rowley, and A. Stefanini, "Measuring barriers to fusion", Annual Review of Nuclear and Particle Science **48**, 401–461 (1998).

[2]N. Michel, W. Nazarewicz, J. Okołowicz, and M. Płoszajczak, "Shell model description of weakly bound nuclei", Nuclear Physics A **752**, Proceedings of the 22nd International Nuclear Physics Conference (Part 2), 335–344 (2005).

[3]Y. Kanada-En'yo, M. Kimura, and H. Horiuchi, "Antisymmetrized molecular dynamics: a new insight into the structure of nuclei", Comptes Rendus. Physique **4**, 497–520 (2003).

[4]D. Tilley, C. Cheves, J. Godwin, G. Hale, H. Hofmann, J. Kelley, C. Sheu, and H. Weller, "Energy levels of light nuclei A=5, 6, 7", Nuclear Physics A **708**, 3–163 (2002).

[5]M. Dasgupta, P. R. S. Gomes, D. J. Hinde, S. B. Moraes, R. M. Anjos, A. C. Berriman, R. D. Butt, N. Carlin, J. Lubian, C. R. Morton, J. O. Newton, and A. Szanto de Toledo, "Effect of breakup on the fusion of ^{6}Li, ^{7}Li, and ^{9}Be with heavy nuclei", Phys. Rev. C **70**, 024606 (2004).

[6]E. F. Aguilera, E. Martinez-Quiroz, P. Rosales, J. J. Kolata, P. A. DeYoung, G. F. Peaslee, P. Mears, C. Guess, F. D. Becchetti, J. H. Lupton, and Y. Chen, "Hindrance of complete fusion in the ^{8}Li +^{208} Pb system at above-barrier energies", Phys. Rev. C **80**, 044605 (2009).

[7]L. R. Gasques, D. J. Hinde, M. Dasgupta, A. Mukherjee, and R. G. Thomas, "Suppression of complete fusion due to breakup in the reactions ^{10,11}B +^{209} Bi", Phys. Rev. C **79**, 034605 (2009).

[8]D. J. Hinde and M. Dasgupta, "Systematic analysis of above-barrier fusion of ^{9,10,11}Be+^{209}Bi", Phys. Rev. C **81**, 064611 (2010).

[9]C. Signorini, A. Yoshida, Y. Watanabe, D. Pierroutsakou, L. Stroe, T. Fukuda, M. Mazzocco, N. Fukuda, Y. Mizoi, M. Ishihara, H. Sakurai, A. Diaz-Torres, and K. Hagino, "Subbarrier fusion in the systems ^{11,10}Be + ^{209}Bi", Nuclear Physics A **735**, 329–344 (2004).

[10]L. Canto, P. Gomes, R. Donangelo, J. Lubian, and M. Hussein, "Recent developments in fusion and direct reactions with weakly bound nuclei", Physics Reports **596**, Recent developments in fusion and direct reactions with weakly bound nuclei, 1–86 (2015).

[11]K. J. Cook, E. C. Simpson, L. T. Bezzina, M. Dasgupta, D. J. Hinde, K. Banerjee, A. C. Berriman, and C. Sengupta, "Origins of incomplete fusion products and the suppression of complete fusion in reactions of ^{7}Li", Phys. Rev. Lett. **122**, 102501 (2019).

[12]R. Rafiei, R. d. Rietz, D. H. Luong, D. J. Hinde, M. Dasgupta, M. Evers, and A. Diaz-Torres, "Mechanisms and systematics of breakup in reactions of ^{9}Be at near-barrier energies", Phys. Rev. C **81**, 024601 (2010).

[13]K. J. Cook, E. C. Simpson, D. H. Luong, S. Kalkal, M. Dasgupta, and D. J. Hinde, "Importance of lifetime effects in breakup and suppression of complete fusion in reactions of weakly bound nuclei", Phys. Rev. C **93**, 064604 (2016).

[14]TUNL Nuclear Data Evaluation Project, *A=7 isobar energy level diagrams*, `https://nucldata.tunl.duke.edu/nucldata/figures/07figs/07_is_2002.pdf`.

[15]A. Shrivastava, A. Navin, N. Keeley, K. Mahata, K. Ramachandran, V. Nanal, V. V. Parkar, A. Chatterjee, and S. Kailas, "Evidence for transfer followed by breakup in ^{7}Li + ^{65}Cu", Physics Letters B **633**, 463–468 (2006).

[16]D. H. Luong, M. Dasgupta, D. J. Hinde, R. D. Rietz, R. Rafiei, C. J. Lin, M. Evers, and A. Diaz-Torres, "Insights into the mechanisms and time-scales of breakup of ^{6,7}Li", Physics Letters B **695**, 105–109 (2011).

[17]D. H. Luong, M. Dasgupta, D. J. Hinde, R. du Rietz, R. Rafiei, C. J. Lin, M. Evers, and A. Diaz-Torres, "Predominance of transfer in triggering breakup in sub-barrier reactions of ^{6,7}Li with ^{144}Sm, ^{207,208}Pb, and ^{209}Bi", Phys. Rev. C **88**, 034609 (2013).

[18]S. Kalkal, E. C. Simpson, D. H. Luong, K. J. Cook, M. Dasgupta, D. J. Hinde, I. P. Carter, D. Y. Jeung, G. Mohanto, C. S. Palshetkar, E. Prasad, D. C. Rafferty, C. Simenel, K. Vo-Phuoc, E. Williams, L. R. Gasques, P. R. S. Gomes, and R. Linares, "Asymptotic and near-target direct breakup of ^{6}Li and ^{7}Li", Physical Review C **93**, 044605 (2016).

[19]K. S. Krane, *Introductory nuclear physics* (John Wiley & Sons, 1991).

[20]L. Chamon, B. Carlson, and L. Gasques, "São Paulo potential version 2 (SPP2) and Brazilian nuclear potential (BNP)", Computer Physics Communications **267**, 108061 (2021).

[21]H. Goldstein, C. P. Poole, J. Safko, et al., *Classical mechanics*, Vol. 2 (Addison-wesley Reading, MA, 1950).

[22]K. Hagino, N. Rowley, and A. Kruppa, "A program for coupled-channel calculations with all order couplings for heavy-ion fusion reactions", Computer Physics Communications **123**, 143–152 (1999).

[23]A. Gavron, "Statistical model calculations in heavy ion reactions", Physical Review C **21**, 230 (1980).

[24]O. Tarasov and D. Bazin, "LISE++: exotic beam production with fragment separators and their design", Nuclear Instruments and Methods in Physics Research Section B: Beam Interactions with Materials and Atoms **376**, Proceedings of the XVIIth International Conference on Electromagnetic Isotope Separators and Related Topics (EMIS2015), Grand Rapids, MI, U.S.A., 11-15 May 2015, 185–187 (2016).

[25]J. Wilczyński, "Optimum Q-value in multinucleon transfer reactions", Physics Letters B **47**, 124–128 (1973).

[26]E. C. Simpson, K. J. Cook, D. H. Luong, S. Kalkal, I. P. Carter, M. Dasgupta, D. J. Hinde, and E. Williams, "Disintegration locations in ^{7}Li → ^{8}Be transfer-triggered breakup at near-barrier energies", Physical Review C **93**, 24605 (2016).

[27]G. F. Knoll, *Radiation detection and measurement* (John Wiley & Sons, 2010).

[28]J. F. Ziegler, M. Ziegler, and J. Biersack, "Srim – the stopping and range of ions in matter (2010)", Nuclear Instruments and Methods in Physics Research Section B: Beam Interactions with Materials and Atoms **268**, 19th International Conference on Ion Beam Analysis, 1818–1823 (2010).

[29]N. Gharibyan, K. Moody, S. Tumey, T. Brown, J. Despotopulos, S. Faye, K. Roberts, and D. Shaughnessy, "Production and separation of carrier-free ^{7}Be", Applied Radiation and Isotopes **107**, 199–202 (2016).

[30]S. Satija, K. A. Domnanich, C. Sumithrarachchi, Y. Liu, S. J. Cingoranelli, S. Saini, I. Chaple, S. E. Lapi, and G. W. Severin, "Production and separation of ^{7}Be for use in an ion source", Applied Radiation and Isotopes **211**, 111382 (2024).

[31]A. Villari, B. Arend, G. Bollen, D. Crisp, K. Davidson, K. Fukushima, A. Henriques, K. Holland, S.-H. Kim, A. Lapierre, et al., "Reaccelerator upgrade, commissioning and first experiments at the National Superconducting Cyclotron Laboratory (NSCL)/Facility for Rare Isotope Beams (FRIB)", Proc. IPAC'22, 101–103 (2022).

[32]A. Villari, G. Bollen, A. Henriques, A. Lapierre, S. Nash, R. Ringle, S. Schwarz, and C. Sumithrarachchi, "Gas stopping and reacceleration techniques at the facility for rare isotope beams (FRIB)", Nuclear Instruments and Methods in Physics Research Section B: Beam Interactions with Materials and Atoms **541**, 350–354 (2023).

[33]M. S. Ltd, *MMM detector design*, https://www.micronsemiconductor.co.uk/product/mmm/, Accessed: 2026-06-23.

[34]K. Cook, "Zeptosecond dynamics of transfer-triggered breakup: mechanisms, timescales, and consequences for fusion", PhD thesis (The Australian National University, 2017).

[35]W. Catford, *CATKIN: the relativistic kinematics programme in excel*, https://personalpages.surrey.ac.uk/w.catford/kinematics/, 2019.

[36]D. Tilley, J. Kelley, J. Godwin, D. Millener, J. Purcell, C. Sheu, and H. Weller, "Energy levels of light nuclei A=8,9,10", Nuclear Physics A **745**, 155–362 (2004).

[37]I. M. Harca, M. J. Basson, K. J. Cook, K. W. Brown, S. A. Gillespie, A. K. Anthony, N. E.

Esker, and S. N. Paneru, "The FABLE silicon detector array for comprehensive studies of fusion and breakup dynamics", Nuclear Instruments and Methods in Physics Research Section A: Accelerators, Spectrometers, Detectors and Associated Equipment **1077**, 170527 (2025).

[38]G. Baur, "Breakup reactions as an indirect method to investigate low-energy charged-particle reactions relevant for nuclear astrophysics", Physics Letters B **178**, 135–138 (1986).

[39]J. Lei and A. M. Moro, "Puzzle of complete fusion suppression in weakly bound nuclei: a trojan horse effect?", Phys. Rev. Lett. **122**, 042503 (2019).

[40]M. Mazzocco, N. Keeley, A. Boiano, C. Boiano, M. La Commara, C. Manea, C. Parascandolo, D. Pierroutsakou, C. Signorini, E. Strano, D. Torresi, H. Yamaguchi, D. Kahl, L. Acosta, P. Di Meo, J. P. Fernandez-Garcia, T. Glodariu, J. Grebosz, A. Guglielmetti, Y. Hirayama, N. Imai, H. Ishiyama, N. Iwasa, S. C. Jeong, H. M. Jia, Y. H. Kim, S. Kimura, S. Kubono, G. La Rana, C. J. Lin, P. Lotti, G. Marquínez-Durán, I. Martel, H. Miyatake, M. Mukai, T. Nakao, M. Nicoletto, A. Pakou, K. Rusek, Y. Sakaguchi, A. M. Sánchez-Benítez, T. Sava, O. Sgouros, V. Soukeras, F. Soramel, E. Stiliaris, L. Stroe, T. Teranishi, N. Toniolo, Y. Wakabayashi, Y. X. Watanabe, L. Yang, Y. Y. Yang, and H. Q. Zhang, "Elastic scattering for the ^{8}B and ^{7}Be +^{208} Pb systems at near-coulomb barrier energies", Phys. Rev. C **100**, 024602 (2019).

[41]W. Huang, M. Wang, F. Kondev, G. Audi, and S. Naimi, "The AME 2020 atomic mass evaluation (i). evaluation of input data, and adjustment procedures*", Chinese Physics C **45**, 030002 (2021).

[42]I. Angeli and K. Marinova, "Table of experimental nuclear ground state charge radii: an update", Atomic Data and Nuclear Data Tables **99**, 69–95 (2013).

[43]P. Mishra, V. Parkar, S. Pandit, S. Kaur, A. Chavan, K. Mahata, A. Shrivastava, K. Ramachandran, V. Kumar, S. Dhuri, P. M, and S. Rathi, "Inclusive and exclusive breakup studies in ^{10}B+^{209}Bi system", Nuclear Physics A **1065**, 123264 (2026).

[44]F. Ajenberg-Selove, "Energy levels of light nuclei A=13–15", Nuclear Physics A **360**, 1–186 (1981).